2D array of metallic nanoparticles: optical characterization and applications as photochemical reactor and SERS-based sensor

Francesca Pincella
Doctoral Program in Materials Science and Engineering

Submitted to the Graduate School of
Pure and Applied Sciences
in Partial Fulfillment of the Requirements
for the Degree of Doctor of Philosophy in
Engineering

at the
University of Tsukuba

Acknowledgements

I would like to thank all group members of Functional Heterointerface Group, present and past, Prof. Miki, Dr. Isozaki, Dr. Sakamoto, Ms. Tanaka, Yeji, Ochiai, Taguchi, Murata, Nittoh, Peter, Tsubomatsu, Kanazawa, Dr. Nishiyama, Deguchi, Ueno, Liu, Fei and Khine, for all your help during these three years.

I want to express all my gratitude to my Doctoral Commission, Prof. Itoh, Prof. Takeuchi, and Prof. Miyazaki, for helpful discussions.

I thank my mother and my brother for supporting me in my hard times, even from very far away I always felt your support. A special thanks to my friends here and in Italy: Alice, Ilaria, Chiara, Davide, Luca, Elena, Eniko, Valentina, Andrea and Rita.

I thank Yeji Song in particular for helping me in the last two years for nanoparticles synthesis and Raman measurement and also for having the patience to try to meet all my absurd requests: I wish you all the best for your future!

A special thanks to the technical staff of MANA NIMS Iiyama, Uemura, Yamada, Tanaka and Nakatsu for their help and support for my experiments.

I also want to thank my previous colleagues at the University of Parma for their continuous support and friendship. I also want to remember my Master Degree supervisor, Prof. Marco P. Fontana, in the proximity of the third anniversary of his passing. His great enthusiasm and vast knowledge will always be an inspiration for my work.

Dedicated to my father, I miss you.

Francesca

Abstract

In the recent year the interest in metallic nanostructures has experienced an exponential increase. Research involving metallic nanostructures spans from fundamental research, where metallic nanoparticle can be used both for their intrinsic optical properties[1,2] or as a very convenient model system to study various phenomena, such as glass transition and, more generally, dynamics of mesoscale systems[3,4], to applications in various fields, from catalysis to biosensing to cancer treatment[5–11].

For what concerns their chemical properties, metallic nanoparticles (MNPs), more correctly metallic nanoclusters (aggregates smaller than 5 nm), were proven to act as good and selective catalyst[5]. Their catalytic activity was shown to depend on the nano-cluster size, preparation method and support material[12]. Regarding their physical properties, instead, their peculiar behavior arises from the collective oscillations of free electrons when electromagnetic radiation of a certain frequency impinges on the MNPs. This collective oscillation, known as localized plasmon resonance (LSPR) can be tailored by changing various parameters such as size, shape [13,14], and composition of the MNP and is responsible for the generation of a strong enhancement of the electromagnetic field in the vicinity of the particle.

Although isolated MNPs possess intriguing properties, when two or more MNPs are brought close to each other (in the range of a few nanometers distance), the most interesting phenomena take place, e.g. appearance of coupled LSPR modes[15–17], "hot spots" of high near-field enhancement[18], Fano resonance[15,19–21]. Therefore, much attention has been devoted recently to the development of efficient ways to prepare metallic nanostructures with sub-10 nm interparticle distance. Despite a huge literature on the topic[22], most of the deposition techniques still suffer from major disadvantages, such as large gap distance, high cost and small substrate area, typical limitations of top-down methods, and low MNPs coverage, poor control of optical properties, and poor reproducibility, typical of bottom-up deposition methods. Nevertheless, due to its versatility and low fabrication cost (no need of clean room facilities or ultra-high vacuum systems), the bottom-up approach is considered extremely promising. In particular, in case of self-assembly based deposition methods, a kaleidoscopic variety of MNPs can be employed, which can be synthesized with wet chemical processes to obtain different size, shape and composition of metallic nanostructures[23,24]. To overcome the aforementioned limitations, dense arrays of Au@Ag NPs should be fabricated bearing a sharp size distribution and a well-defined interparticle distance. To accomplish that a self-assembly based bottom-up deposition method developed by our group[25] was employed. This method enable the deposition of any kind of MNPs on a large scale conducting substrate achieving high MNPs coverage, MNPs mechanical stability (MNPs are chemically bound to the substrate) and a fixed interparticle distance.

In this work the successful deposition of a dense 2D array of Au@Ag NPs with sub-3 nm interparticle distance, good NPs size dispersion and tunable optical properties is demonstrated. The high quality of these arrays enabled the experimental investigation of the optical properties of strongly coupled assemblies of complex MNPs. The optical response of these 2D arrays was characterized by UV-Vis spectroscopy, and it was found that they support an intense and sharp LSPR which can be tuned in a vast range of wavelengths according to the metallic composition and size of the nanoparticles and on the substrate chosen (gold or ITO thin film).

Considering the interesting optical response of these 2D arrays, their successful employment for various applications was anticipated. In fact, the strong near-field light generated in the proximity of the metallic nanoparticles, and especially in the gap between them, can be used to make up for the low quantum efficiency on nonlinear phenomena, paving the way for the direct observation of exotic phenomena under irradiation with common incoherent light sources, instead of expensive high-power pulsed lasers. A few interesting applications were then identified, such as Surface Enhanced Raman Spectroscopy (SERS), Two-Photon

Absorption (TPA) induced photoreactions, and TPA-based visible light sensitization of wide bandgap semiconductors.

At first the application of these 2D arrays as multipurpose and tailorable SERS substrates is reported. For the choice of the suitable MNPs for our purpose, the two most common plasmonic materials, silver and gold, were chosen. In fact, even though various metals can be used for the development of plasmonic nanoparticles, silver and gold NPs are widely considered the best candidates to achieve high enhancement in the UV-Vis-NIR region. Gold is usually preferred because of its good chemical stability in ambient condition and fine control of size and shape of NPs with wet chemical processes, although showing lower plasmonic enhancement in the visible range due to higher plasmon damping compared to silver. Recently much effort has been directed to prepare AgNPs with good size and shape control, [26,27] but the results are still far from the fine tuning achievable with AuNPs and therefore limiting their application in the preparation of dense two-dimensional (2D) arrays of MNPs. To overcome such limitations, the use of Au-core/Ag-shell structure (Au@Ag) was proven advantageous.[28–31] Au@Ag NPs combine the good size and shape control of AuNPs and the high near-field enhancement of AgNPs, allowing us to produce MNPs with a sharp size distribution, which is suitable to achieve dense arrays with optimal control of optical properties. In addition, it is well known that colloidal Au@Ag NPs are able to produce LSPRs in a vast range of wavelengths simply by changing the silver shell thickness, making them good candidates to achieve plasmonic substrates tunable in a wide range of wavelengths.[29,32,33] Furthermore, it was recently proven that a charge transfer complex at the interface between gold and silver can partially protect the silver shell from oxidation.[28] In detail, plasmonic arrays of Au@Ag NPs were obtained by means of a hybrid deposition method developed by our group, then these arrays were characterized experimentally by UV-Vis spectroscopy and SERS, and their optical response was also studied computationally by discrete-dipole approximation (DDA) simulations, revealing their potential as efficient SERS substrate in the visible range. The highest average enhancement factor was achieved for 2D array prepared with the largest Au@Ag NPs (5.9×10^6) comparable with results from self-assembled films of silver nanoparticles.[23] The SERS enhancement factor was also proven to be extremely homogeneous (relative standard deviation below 25%) over the substrate, showing the high potential of this self-assembled 2D array as SERS-based sensor. In addition, SERS and DDA simulations revealed that the near-field optical response of Au@Ag 2D arrays can be greatly affected by various parameters, such as particle size, Ag:Au ratio and aggregation. In case of 40Au@Ag series, in fact, an increase of the enhancement factor close to two orders of magnitude was found upon silver shell growth. In addition, it was found that the near-field response of the 2D array cannot be straightforwardly predicted from the study of its far-field response[34], since the latter cannot account both for the exact position (redshift) and for the intensity of the maximum enhancement.

Second, the successful application of such 2D array as a near-field plasmonic substrate to induce or enhance photochemical reactions is described. The strong enhancement of the incident field, in fact, is used to enhance weak nonlinear processes in the proximity of metallic nanoparticles, such as two-photon absorption (TPA). TPA has attracted a huge deal of attention for its ability to shift the excitation wavelength needed to trigger photoreactions from UV to the visible range (suitable for solar applications), but its application is limited to high power excitation sources[35] and molecules with large nonlinear cross-section. Therefore, plasmonic substrates were recognized as the natural and most prominent candidate to enhance TPA-induced photoreactions.[36–39] Our plasmonic substrate was employed to induce photodimerization of an anthracene derivative under visible light irradiation with an incoherent light source. Despite the efficient photoreaction property of anthracene derivatives and the huge number of publications about them[40–42], there has never been a report of a multiphoton photoreaction involving an anthracene derivative with the exception of a reverse photoconversion of anthracene photodimer to monomer with three-photon absorption.[43] In this work the progress of the TPA-induced photoreaction was examined by means of surface-enhanced Raman scattering, taking advantage of the ability of our plasmonic substrate to enhance and localize both incident light for photoreaction and Raman scattering signal for analysis of the photoreaction products. The TPA-induced

photoreaction in the case of anthracene carboxylic acid coated 2D array of gold nanoparticles gave different results according to the properties of the plasmonic substrate, such as the size of the gold nanoparticle and also its resultant optical properties. In particular, a stringent requirement to achieve TPA-induced photodimerization was found to be the matching between irradiation wavelength, localized surface plasmon resonance of the 2D array, and twice the wavelength of the molecular excitation of the target material (in this case, anthracene carboxylic acid). These results will be useful for the future development of efficient plasmonic substrates for TPA-induced photoreactions with various materials.

Finally, the feasibility of a bottom-up approach to fabricating a visible light-driven titania photocatalyst device was demonstrated. This device contains an embedded 2D array of gold nanoparticles that acts as a near-field light-generating layer. The device is a layered structure prepared by depositing a 2D array of AuNPs on a transparent conductive substrate (10 nm ITO layer on quartz), coating the 2D array of AuNPs with a monolayer of TMOS, and depositing titania nanocrystals on the anchoring molecule (TMOS) layer. The visible light activity of the device was tested using photocatalytic degradation of methylene blue (MB) by illuminating the device with visible light (700 nm light) and UV light (250–380 nm). The localized surface plasmon resonance peak of the 36 nm AuNP 2D array is around 700 nm with a full width at half maximum of 350 nm. In comparison with other control samples, the device showed the highest photocatalytic activity with visible irradiation, which was 1.7 times higher than that of titania with UV irradiation. The origin of the visible light activity was confirmed by both quadratic incident light power dependency and action spectrum to be plasmon-induced (near-field enhancement by AuNPs) two-photon absorption.

Table of Contents

List of common abbreviations and symbols

2D : two dimensional

ACA : anthracene carboxylic acid

AgNP : silver nanoparticle

AQCA : anthraquinone carboxylic acid

Au@Ag NP : gold core-silver shell nanoparticle

AuNP : gold nanoparticle

DDA : discrete-dipole approximation

DFT : Density Functional Theory

Dod : dodecanethiol

EDX : energy-dispersive X-ray spectroscopy

HBAC : 10,10'-dihydroxy-9,9',10,10'-tetrahydro-bianthryl-dicarboxylic acid

Hex : hexanethiol

Hexdt : hexanedithiol

HRTEM : high resolution transmission electron microscope

ITO : indium tin oxide

LSPR : localized surface plasmon resonance

MB : methylene blue

MNP : metallic nanoparticle

MPTMS : 3-mercaptopropyl trimethoxysilane

NF : near field

NIR : near-infrared

R6G : rhodamine 6G

SEM : scanning electron microscope

SERS : surface-enhanced Raman Scattering

SPR : surface plasmon resonance

TEM : transmission electron microscope

TPA: two-photon absorption

UV : ultraviolet

Vis : visible

Introduction

In the recent year the interest in metallic nanostructures has experienced an exponential increase. The peculiar optical behavior of metallic nanoparticles (MNPs) arises from the collective oscillations of free electrons when electromagnetic radiation of a certain frequency impinges on the MNPs (localized surface plasmon resonance, LSPR). Although isolated MNPs possess intriguing properties, when two or more MNPs are brought close to each other, the most interesting phenomena take place, e.g. appearance of coupled LSPR modes, and "hot spots" of high near-field enhancement. Therefore, much attention has been devoted recently to the development, study and application of metallic nanostructures, especially aggregated structures with small gaps.

In this thesis the general concept of plasmons is introduced in Chapter 1, starting from bulk plasmons to finally focus on plasmons in strongly coupled systems, of particular interest for understanding the optical response of aggregated metallic nanoparticles on a conductive substrate. Analytical methods and numerical methods are briefly discussed, with particular emphasis on numerical methods that allow the study of the far- and near-field response of complex nanostructures and aggregates. In Chapter 2, a brief retrospective on the most common methods currently available to design and develop plasmonic nanostructures is provided. The methods are divided according to the underlying approach as top-down and bottom-up methods. At last, new hybrid methods are introduced, including the deposition method developed in our group. Then, some interesting applications of plasmonic substrates are introduced. A few interesting examples of nonlinear phenomena that can be successfully enhanced or triggered by the strong near-field induced by plasmonic substrates are presented, among them surface enhanced Raman scattering (SERS), two-photon absorption (TPA) induced photoreactions and TPA-based photosensitization of wide bandgap semiconductors. Afterwards, the details about the synthesis, preparation and characterization of the desired plasmonic substrates are reported in Chapter 3. From Chapter 4 to Chapter 6, three cases of successful application of our two-dimensional array of metallic nanoparticles are described in detail.

1. Plasmons: theory

Plasmons are the quanta of collective oscillations of free electrons in a metal. They can be divided according to their confinement as bulk, surface and localized surface plasmons.

As a simple picture, the motion of electrons in metals can be describes as a free electron gas moving in presence of an external field as in:[44]

$$m\frac{d^2x}{dt^2} = -\frac{m}{\tau}\frac{dx}{dt} - qE_{tot}(t) \quad (1)$$

where m is the electron effective mass, q is the charge of the electron, τ is the decay time, and E_{tot} is the total electric field on the electron (sum of external and internal electric field). The displacement (one-dimension) induced by an incident field of frequency ω can be written as:

$$x(\omega) = \frac{qE_{tot}}{m(\omega^2 + i\,\omega/\tau)} \quad (2)$$

while the induced polarization can be expressed as:

$$P = -qx(\omega)n \quad (3)$$

where n is the conduction electron density.

From the relationship between the displacement field and the polarization, the expression of the dielectric constant of a metal is obtained:

$$\varepsilon(\omega) = \varepsilon_o(\omega) - \frac{\varepsilon_o(\omega)\omega_p^2}{\omega^2 + i\,\omega/\tau} \quad (4)$$

The plasmon frequency ω_p is defined as:

$$\omega_p = \sqrt{\frac{4\pi q^2 n}{\varepsilon_o m}} \quad (5)$$

Therefore, the equation of the displacement of a conduction electron driven by the total electric field can be rewritten, taking into account of this result:

$$x(\omega)\left(\omega^2 + \frac{i\omega}{\tau} - \frac{4\pi n q^2 x}{\varepsilon_o m}\right) = \frac{q}{m}E_{ext}(\omega) \quad (6)$$

At the bulk plasmon frequency, in case of ideal metals (zero damping, $\tau \to \infty$), the displacement remain finite for an arbitrarily small driving field. This excitation, best known as bulk plasmon, cannot couple directly to light due to its longitudinal nature.

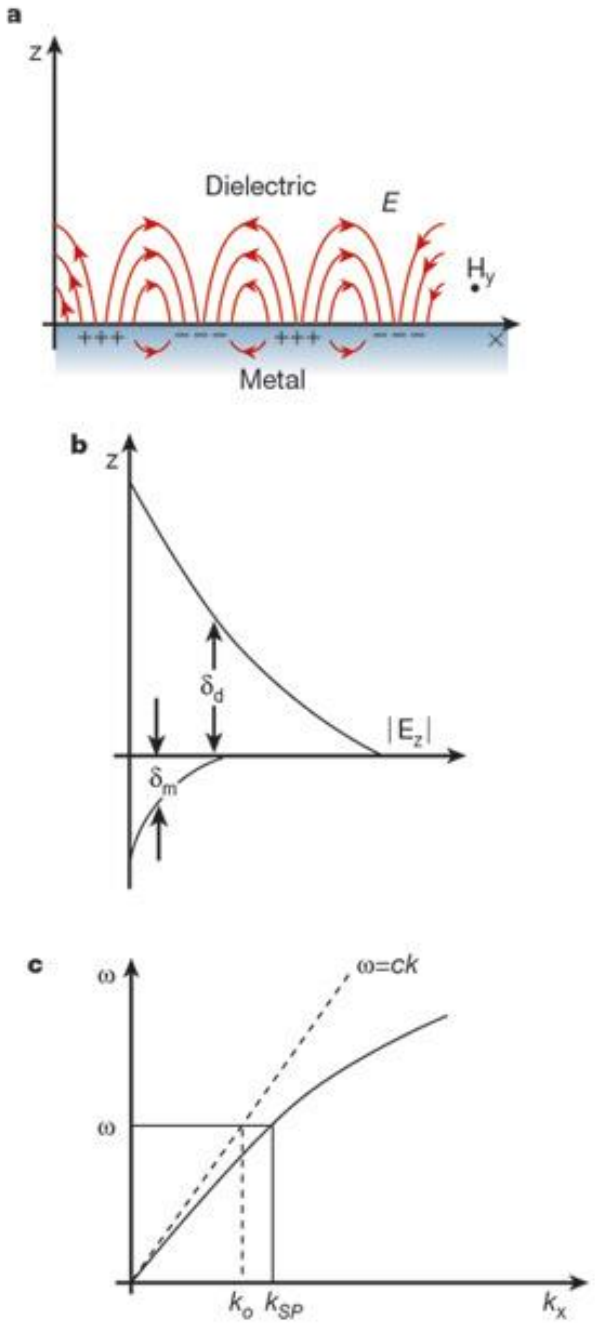

Figure 1 a) Electromagnetic wave and surface charge of SPs at the interface between a metal and a dielectric material. b) The field component perpendicular to the surface is enhanced near the surface and decays exponentially with distance away from it (b). The field in this perpendicular direction is called evanescent, reflecting the non-radiative nature of SPs, and prevents power from propagating away from the surface. In the dielectric medium above the metal, typically air or glass, the decay length of the field, δd, is of the order of half the wavelength of light involved, whereas the decay length into the metal, δm, is determined by the skin depth. c, The dispersion curve for a SP mode shows the momentum mismatch problem that must be overcome in order to couple light and SP modes together, with the SP mode always lying below the light line, that is, it has greater momentum than a free space photon of the same frequency ω. From ref. [45]

When the interface of a metal and a dielectric are considered, new plasmons can be observed, called surface plasmons, see Fig. 1. Considering boundary conditions, the following dispersion relationship for a field propagating along x is obtained:

$$k_x^2 = \frac{\varepsilon_1 \varepsilon_2 \omega^2}{(\varepsilon_1 + \varepsilon_2)c^2} \tag{7}$$

As a results, in case of air/metal interface ($\varepsilon_1 = 1$, $\varepsilon_2 = 1 - \omega_p^2/\omega^2$ metal with no damping), the relationship becomes:

$$k_x^2 = \left(\frac{\omega^2 - \omega_p^2}{\omega^2 - \omega_s^2}\right)\left(\frac{\omega^2}{2c^2}\right) \tag{8}$$

where $\omega_s \equiv \omega_p/\sqrt{2}$ is the surface plasmon frequency.

It is to be remarked that the surface plasmons cannot be normally excited directly by incident value, since the dispersion curve of k_x lies below the photon wave vector for all frequencies. The typical approaches to make up for the momentum mismatch are the introduction of a grating or a high-index-prism (as often used for surface plasmon resonance, SPR, techniques in both Kretschmann and Otto configurations).

1.1 Localized Surface Plasmon Resonance

When the oscillation of the free electron gas is further confined from the surface to a particle whose dimensions are smaller than the wavelength of light (see Fig. 2), a quantization of the modes is obtained in the all three dimensions. This leads to the appearance of discrete non-propagating modes.

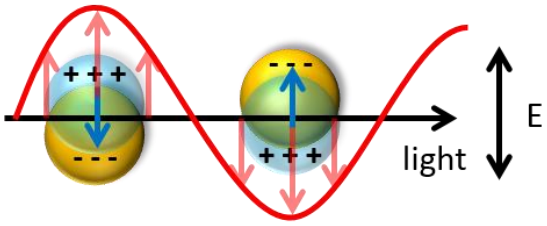

Figure 2 Schematic draw of oscillation of metallic nanoparticles' charge induced by an incident electric field ***E****.*

In case of nanoparticles whose radius is much smaller than the wavelength of light, the treatment of the optical response of the metallic particle can be limited to the quasistatic approximation. In this case only dipolar modes can be excited by a plane incident wave, allowing therefore to neglect higher order modes (no retardation effects). In the quasistatic limit a simple relationship for the nanoparticle polarizability is obtained, that is:

$$\alpha = \frac{(\varepsilon_{in} - \varepsilon_{out})\varepsilon_{out} a^3}{(\varepsilon_{in} + 2\varepsilon_{out})} \tag{9}$$

where ε_{in} and ε_{out} are the dielectric constant of the metallic particle and of the surrounding medium, respectively.

In general, although only dipolar modes can be excited by a plane wave in the quasistatic limit, more complex plane fronts can excite also higher order modes, which can be expressed as:

$$\omega_l = \omega_p \sqrt{l/(l + (l+1)\varepsilon_{out})} \tag{10}$$

As it can be noticed from the previous results, from quasistatic approximation, resonance conditions are independent of nanoparticle size. Therefore, it is easy to understand that this approximation fails to describe the nanoparticles optical response for sizes as small as 10% of the incident wavelength, where retardation effect has to be taken into account.[44]

For larger particles the analytical solution for the Maxwell's equation was first obtained by Mie and takes into account the possibility to excite higher order modes even with an incident plane wave. Anyway, the analytical solution of Maxwell's equation is limited to very few shapes and therefore numerical methods have been developed to study the optical response of complex metallic nanoparticles shapes and aggregates of particles.

1.2 Plasmons in strongly coupled systems

In addition to single nanoparticles, another emerging issue is to deal with aggregated plasmonic structures or nanoparticles interacting with a surface, either insulating or metallic.[46] The case of nanoparticles on a dielectric substrate can be described as consisting of the interaction of the nanoparticle with its image charge in the substrate. This interaction is dependent on the dielectric constant of the substrate, since it is screened by a factor $(\varepsilon - 1)/(\varepsilon + 1)$ where ε is the dielectric constant of the substrate, and on the distance between the nanoparticle and the substrate. Even in case of weak interaction this effect can remove the degeneracy in the modes of a metallic particle.[47] Although for a complete description of the interaction between metallic nanostructures and metallic substrates numerical simulations are of invaluable help, a simple approach can be useful to predict the optical response of this coupled system. Plasmon hybridization theory[48,49] is a good example of a simple and straightforward method to evaluate the interaction of coupled systems, such as nanoparticle over substrate.[50] In case of metallic substrates, the nanoparticles do not only experience the effect of the image charge, but can also interact with the surface plasmon of the metallic film. In the simple case of a gold nanoparticles on a gold thin film whose thickness is larger than the diameter of the metallic nanoparticle, the modes of the gold nanoparticle will experience a redshift, which is strongly dependent (inversely proportional) on the distance between the particle and the substrate. This description will fail in case of metallic films whose thickness is comparable or smaller than the nanoparticle diameter. In the latter case, the interaction will be strongly dependent on the density of continuum states of the metallic film (surface states), see Fig. 3.

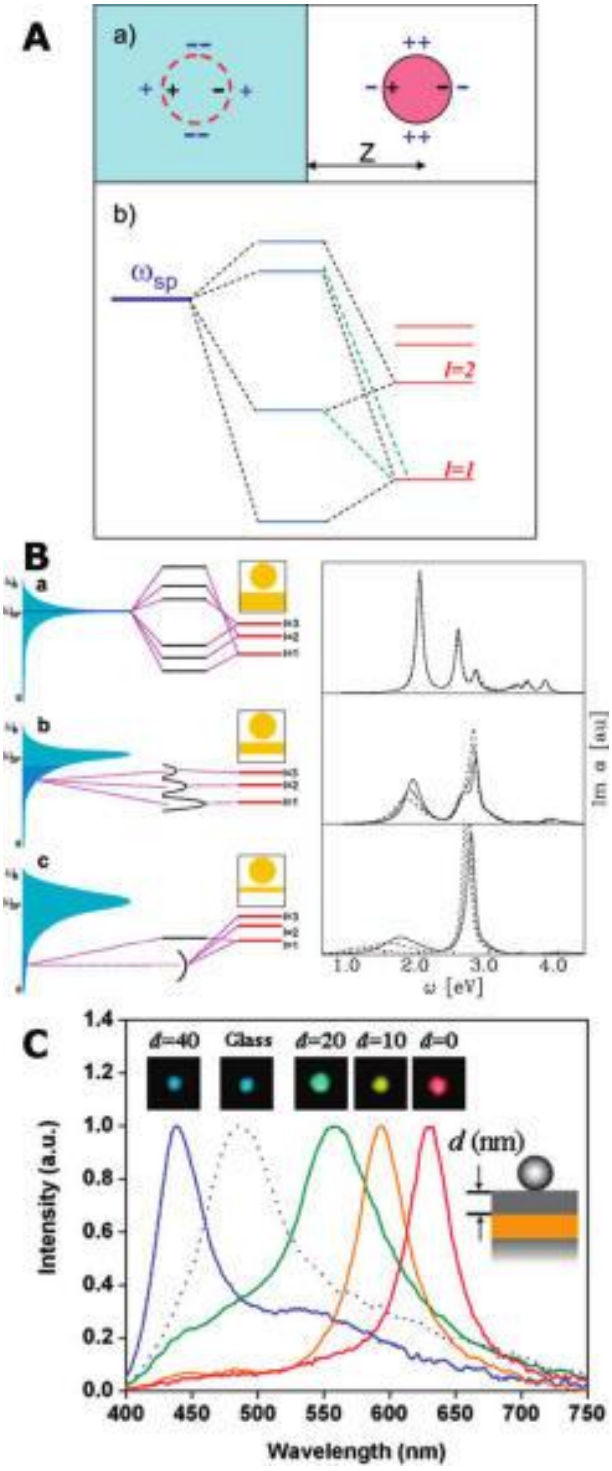

Figure 3 (A) Schematic illustrating the interaction of a nanosphere with a metallic surface. Panel a shows the image forces obtained assuming a perfect response of the surface for an l = 1 (dipolar) and an l = 2 (quadrupolar) sphere plasmon. The surface mediates an interaction between plasmons of different l, resulting in a distance-dependent hybridization of the nanosphere plasmons in a manner similar to the nanosphere dimer. Panel b shows plasmon hybridization in this system. The nanoparticle plasmons interact with the surface plasmons, resulting in shifts and an effective hybridization between nanoparticle plasmons of different angular momentum l.[50] *(B) The three interaction regimes (a-c) for a plasmonic nanoparticle and the surface plasmons of a thin metallic film. For each case, the left panel illustrates the energetics of the interaction regime, while the right panel shows the corresponding calculated dipolar optical absorption spectrum for various film thicknesses corresponding to this regime. The plasmonic density of states is illustrated in light blue, the effective continuum of the film is illustrated in dark blue and the resulting hybridized plasmons are shown in black. (a) the regime corresponding to the thick film limit (much thicker than the nanoparticle diameter), where the effective continuum of the film lies at higher energies than the nanoparticle plasmon. (b) left panel: the intermediate regime (on the order of the nanoparticle diameter), where the nanoparticle plasmon is resonant with the effective continuum of the film. (c) the regime of the thin film limit (significantly smaller than the diameter of the nanoparticle), where the effective continuum of film plasmons lies at lower energies than the nanoparticle plasmon.*[51] *(C) Examples of optical scattering spectra for individual silver nanoparticles on a silica layer of varying*

thickness above a 50 nm gold film. Insets show a dark field image of each individual nanoparticle. The dotted spectrum represents an individual silver nanoparticle over a glass substrate.[52] *From ref.* [17]

In addition to the case of nanoparticle supported over a substrate, the plasmon hybridization picture is particularly helpful to describe simple aggregates of nanoparticles, such as dimers with strong coupling[49] (small interparticle distance) or complex nanostructures such as nanoshells[53] or core-shell nanoparticles.[54] In such simple situations, the plasmonic modes of the coupled structure can be express as a combination of the modes of its components. This treatment is the plasmonic equivalent of the molecular orbital theory and from this latter borrows the definition of the coupled modes as low-energy bonding, and high-energy antibonding modes.

In Fig. 4 a few examples of successful application of the plasmon hybridization theory are shown: which are nanoparticles dimers, thin metallic films, nanoshells, and metallo-dielectric core-shell nanoparticles.

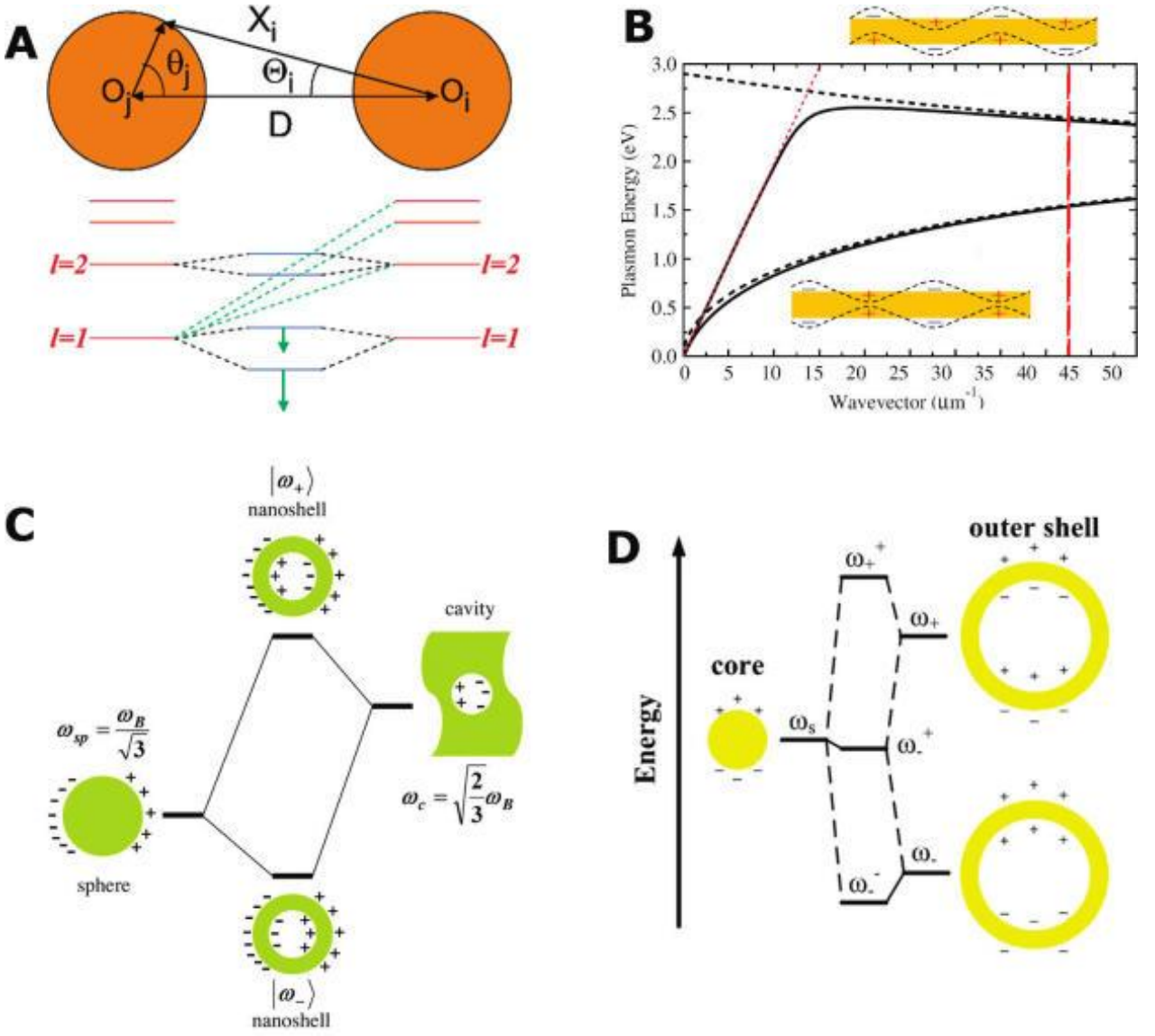

Figure 4 (A) Schematic picture illustrating the plasmon hybridization in a nanoparticle dimer. The individual nanosphere plasmons on the two particles interact and form bonding and antibonding dimer plasmons. In the dimer geometry, nanosphere plasmons with a given angular momentum l interact also with plasmons of different angular momentum on the other particle at small interparticle distances.[49] *(B) Exact retarded calculation of the bonding and antibonding film plasmon dispersion. Insets show schematic surface charge density distribution for the bonding (bottom) and antibonding (top) film plasmon.*[53] *C) An energy-level diagram describing the plasmon hybridization in metal nanoshells resulting from the interaction between the sphere and cavity plasmons. The two nanoshell plasmons are an antisymmetrically coupled (antibonding) plasmon mode and a symmetrically coupled (bonding) plasmon mode.* [48] *(D) Plasmon hybridization diagram for a gold-silica-gold layered nanoparticle.*[55] *From ref.*[17]

Of course, to describe larger aggregates different methods have to be implemented, in particular in case of weakly interacting particles ("diluted systems"), where higher order interactions between nanoparticles can be neglected, an effective medium approach can be applied.[17] The most popular model for this purpose is the Maxwell-Garnett approximation.[56] This approximation takes advantage of the Clausius-Mossotti formula:

$$\frac{\varepsilon_{eff} - \varepsilon_m}{\varepsilon_{eff} + 2\varepsilon_m} = \frac{\alpha}{3v\varepsilon_m} \tag{11}$$

where v is the (average) volume of the single particle, α is the polarizability of the particles, ε_{eff} and ε_m are the effective dielectric constant and the dielectric constant of the surrounding medium (matrix), respectively. Introducing Eq. 11 in Eq. 9, the equation for the effective dielectric constant can be written as:

$$\varepsilon_{eff} = \varepsilon_m \frac{\varepsilon(1+2f) + 2\varepsilon_m(1-f)}{\varepsilon(1-f) + \varepsilon_m(2+f)} \tag{12}$$

where *f* is the filling fraction of gold (of dielectric constant ε) inside the matrix. This approximation was proven to successfully describe sparse nanoparticles in a silica matrix up to a filling fraction $f = 0.3$.[57]

1.4 Plasmons: numerical methods

In order to find a solution for more complex structures, numerical methods have become an indispensable tool. At present, various approaches to solve the scattering problem for a nanoparticle of generic shape and material are available, they are notably (but not only) Finite-Difference Time-Domain (FDTD) method, Discrete-dipole Approximation (DDA) method, Multiple Multipole (MMP) method and Boundary-Element method (BEM). In our work DDA was employed since it allows the straightforward calculation of both far-field and near-field optical properties of aggregates of complex (e.g. core-shell) metallic nanoparticles.

1.4.1 DDA simulations

DDA is a powerful method to compute extinction spectra (scattering and absorption) of objects of arbitrary geometries and with the additional advantage of using experimental values of dielectric constants to model the objects. DDA code DDSCAT 7.3[58–60] was employed to compute both far-field extinction (scattering and absorption) spectra, and electric near-field inside and in the proximity of noble metallic (Au and Ag) and bimetallic (concentric Ag-shell and Au-core) nanoparticle and their assemblies. DDA computes the response of the object of interest by representing it as a grid of discrete and mutually interacting dipoles. The polarizability of each dipole corresponds to that of the volume element of the material that it represents. Each dipole will then experience the contribution of both the external driving electric field and the field generated by the surrounding dipoles. The local field at a dipole of index *i* can be written as:

$$\mathbf{E}_i^{loc} = \mathbf{E}_i(\omega) + \sum_{j \neq i} \mathbf{G}_{ij}(\omega)\alpha_j(\omega)\mathbf{E}_j^{loc}(\omega) \tag{13}$$

where $\mathbf{E}_i$ is the driving field at the position *i*, α_j is the polarizability of the dipole *j*, and $\mathbf{G}_{ij}$ is the free-space Green's tensor that propagates the field from *j* to *i*. Then, after obtaining the self-consistent solution for the electric field at each dipole, the electric field can be computed at any point outside the discretized object. The main disadvantages of DDA are related to the computational time, which scales with the volume of the object, and to the artifacts that can be observed in the near-field, that are intrinsically related to the volume

discretization. The choice of the distance between each dipole (represented as a cube whose side is equal to the inter-dipole distance set for simulations) in fact strongly affect both intensity of the near-field[61,62] and the smoothness of the surface of the object under consideration, which is especially crucial for curved surfaces, as in the typical case of the sphere.

2. Plasmonic substrates

Despite a huge literature regarding the development and applications of plasmonic substrates,[22] most of the deposition techniques still suffer from major disadvantages. The most common issues are large gap distance, high cost, small substrate area, typical limitations of top-down methods, and low MNPs coverage, poor control of optical properties and reproducibility, typical of bottom-up deposition methods. Nevertheless, due to its versatility and low fabrication cost (no need of clean room facilities or ultra-high vacuum systems), the bottom-up approach is considered particularly promising. In particular, in case of self-assembly based deposition methods, a kaleidoscopic variety of MNPs can be employed. Different MNPs can be synthesized with wet chemical processes to obtain different size, shape and composition of metallic nanostructures.

2.1 Top-down methods

Top-down methods for the fabrication of plasmonic substrates are inspired by the idea of achieving nanostructures from metallic thin film by successive "removal" until the desired size and shape is obtained. This approach requires typically the use of clean-room facilities and expensive equipment. The most common techniques that can be ascribed to this class of deposition methods are optical lithography, electron-beam lithography and focused-ion-beam milling.[63]

Optical lithography has long been known and used: it requires the use of a mask to produce the desired pattern on a thin polimeric film ("photoresist"). The mask will be irradiated and only the area of the photoresist layer not screened by the mask will undergo a photoreaction, see Fig. 5. Then, the film is exposed to a chemical developer to obtain the pattern, the result will depend on the kind of photoresist used; in case of positive photoresist the irradiated area is removed by the chemical developer, while the opposite occurs for negative photoresists. As it can easily understood, the limitations of this techniques are directly related to its optical nature. Although UV light is used to pattern the structure, the diffraction limit (about half of the wavelength) set the smallest features that can be achieved by optical lithography. After producing the pattern by lithography, a thin metallic film is deposited on the patterned substrate. After this step, the sample is then immersed in a suitable solvent to remove the resist. Together with the photoresist, also the metal deposited onto the resist will be removed ("liftoff process"), giving as a final result a substrate with the desired pattern of metal. Although straightforward and easy to apply for the development of various structures, this methods presents several problems related to low yield and poor quality of the metallic pattern.

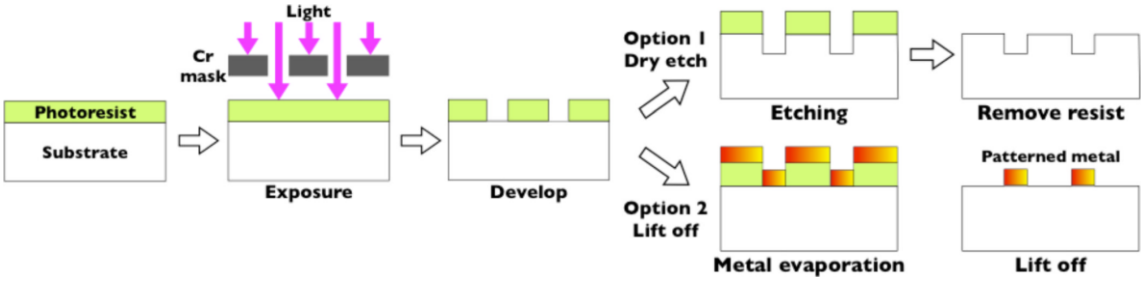

Figure 5 Lithographic patterning: Option 1: If the substrate is amenable to dry etching (e.g. Si or SiO2), the pattern in the photoresist is readily transferred. Option 2: If the substrate is not amenable to dry etching like most metallic films, a lift-off process is used instead. From ref.[63]

Another approach consists in employing electrons instead of light as an exposure method to achieve patterns in the resist. When using electron-beam lithography, a high energy focused electron beam scans the resist film to form a pattern. With this techniques features as small as 5 nm can be achieved under optimal conditions.

A third approach is to use a focused ion-beam to remove the "undesired" areas directly from the metallic film on the substrate, without the need of a resist layer.

2.2 Bottom-up methods

A different approach to achieve plasmonic substrate is to try to mimic nature, that is to say build nanostructures starting from small building block, such as atoms or molecules. This choice is particularly compelling for its ability to decrease below the capability of top-down techniques the size of the nanostructures that can be prepared. In addition, bottom-up deposition techniques do not necessitate of expensive machines, clean-room facilities and ultra-high vacuum equipment, relying mainly on techniques that do not need extreme synthetic conditions.

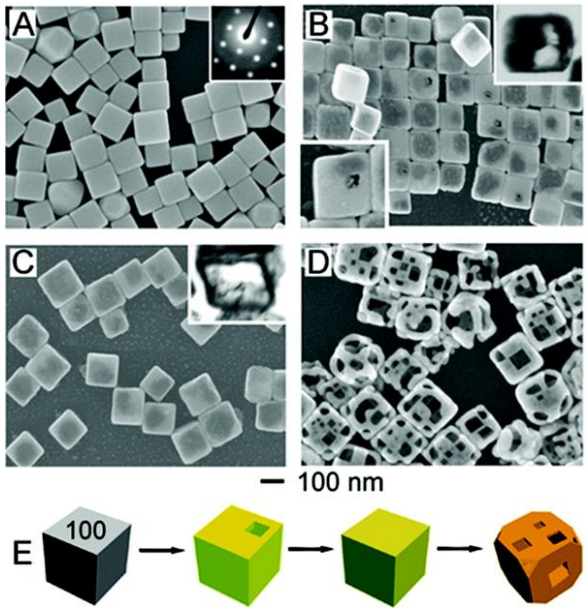

Figure 6 Example of metallic nanoparticles prepared from wet chemical processes. (A) SEM of Ag nanocubes; electron diffraction (inset). (B) SEM of product after 0.30 mL of 1 mM $HAuCl_4$ solution was added to a 5-mL 0.8 mM Ag nanocube suspension; a pinhole (lower inset) is observed on the exposed face of ~1 in 6 nanocubes and TEM (upper inset) of a microtomed sample reveals early hollowing out. (C) SEM of product after 0.50 mL of $HAuCl_4$ solution was added; TEM (inset) of a microtomed sample reveals the hollow interior of the nanobox. (D) SEM of product after 2.25 mL of $HAuCl_4$ solution was added; porous nanocages were produced. (E) Illustration summarizing morphological changes. Coloration indicates the conversion of a Ag nanocube into a Au/Ag nanobox then a predominately Au nanocage. From ref.[64]

The main example of bottom-up method is the synthesis of metallic nanoparticles by means of wet-chemical processes,[10] see Fig. 6. With these methods metallic nanoparticles of various sizes, shapes and compositions can be prepared. At the moment, a vast literature can be found on the topic, although limitations still exist for what concern the polidispersity of the nanoparticles, the yield, and the possible shapes. In particular, the controlled synthesis of silver nanoparticles has proven to be particularly challenging.[65]

2.3 Assembly of metallic nanoparticles

Once the desired MNPs have been synthetized by wet-chemical processes, it is of great interest to immobilize them onto solid structures to achieve the desired plasmonic substrates, in analogy with what can be obtained from top-down processes. A few well-established deposition techniques can be applied to the formation of a two-dimensional (2D) or three-dimensional (3D) ordered arrangement of metallic nanoparticles.

2.3.1 Langmuir-Blodgett

Historically, Langmuir-Blodgett (vertical lifting method) and Langmuir-Schaefer (horizontal lifting method) have been applied for the preparation and transfer to solid substrates of monolayers of amphiphilic molecules or polimeric materials.[66,67] In the case of amphiphiles, the molecules are spread at the water/air interface to form a sub-monolayer. The solvent used for the spreading should be non-polar and volatile, to allow for the molecules to arrange at the interface with their hydrophilic head immersed in the subphase (usually deionized water, but saline solutions or acidic solutions are common) and the hydrophobic tail instead out of the subphase. Then, after equilibration, the sub-monolayer is compressed by the slow movement of two (or one, depending on the though used) Teflon barriers. The compression can be followed in real-time by evaluating the pressure-area isotherm (transition from gas phase, to liquid and finally condensed phase). When a close-packed monolayer is obtained (condensed phase, before collapse), the film is transferred on a solid substrate by vertical or horizontal lifting method.

The Langmuir-Schaefer deposition method can be applied with some precautions also to metallic nanoparticles coated with hydrophobic capping agents, such as alkanethiols.[68] The main issues related to the application of this technique to metallic nanoparticles is linked to their poor mobility at the interface once they are spread at the interface. Fig. 7 shows an example of this behavior: alkanethiol-capped MNPs form rigid island-like aggregates that will not be destroyed upon compression and finally give a sub-monolayer with high percentage of voids.[69]

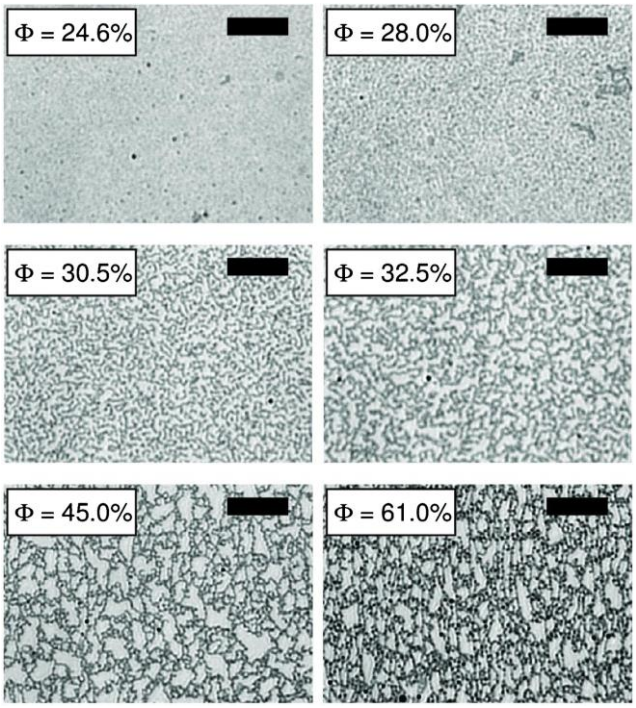

Figure 7 Formation of a 2D gel network as the surface concentration of GNPs is increased. The images, recorded using an inverted microscope, show the evolution of the film structure as ϕ (surface concentration) is increased, as indicated in each image. At the highest concentration a network is formed. The scale bar in each figure corresponds to 50 μm. From ref.[69]

2.3.2 Chemical immobilization

The Langmuir-Schaefer method, apart from the limitations in the final MNP coverage, has another disadvantage that consists in the nature of the immobilization of the monolayer on the substrate. For Langmuir-

Schaefer films, in fact, the film is only physisorbed at the surface, therefore it can be easily removed from the substrate. This characteristic limits then its recyclability, since typically the film will be removed upon repeated rinsing or sonication. In order to have MNPs strongly bound to the substrate, chemical immobilization can be used. This mechanism requires the formation of a self-assembled monolayer (SAM) of molecules on the substrate. The bi-functional molecule used should have a functional group that strongly links to the substrate and another group that can chemically bind to the metallic nanoparticles. This method is easy and straightforward to implement, but, as for the case of Langmuir-Blodgett, usually results in low MNP coverage, as shown in Fig. 8.

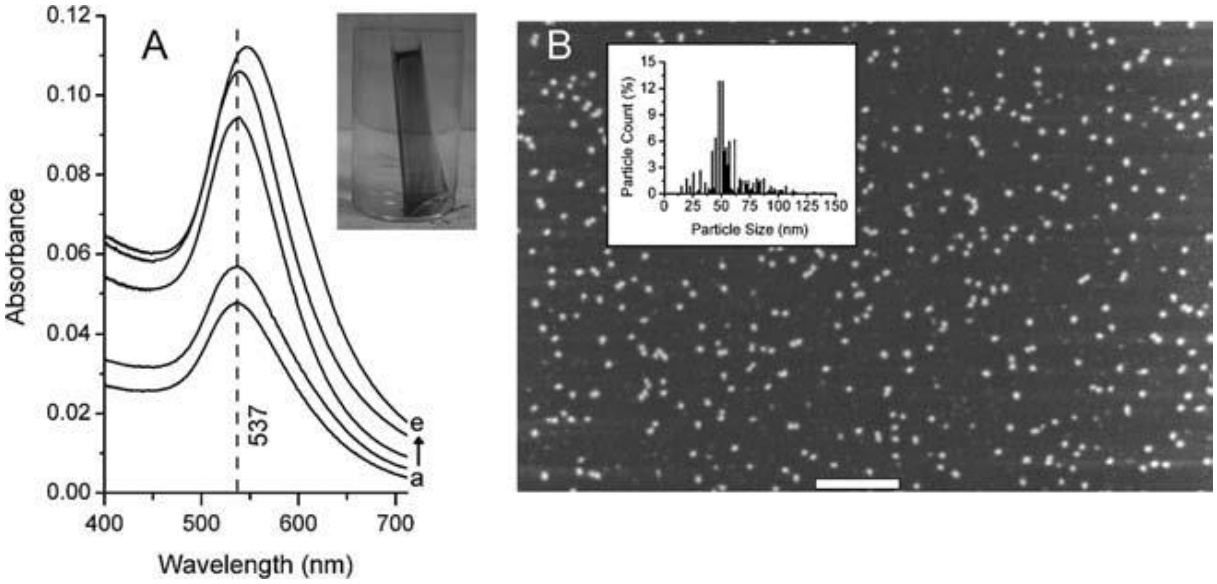

Figure 8 (A) Temporal evolution of Au nanoparticle film SPR absorption; samples (a) through (e) refer to 30, 60, 120, 180, and 300 s after immersion into a Au growth solution of a DEDAS-stabilized Au seed layer whose time-zero spectrum (not shown) was located at the baseline on this scale. Inset shows the appearance of the final Au nanoparticle film on a glass support. (B) SEM image of a typical Au nanoparticle assembly and corresponding histogram showing the size distribution of supported nanoparticles formed. The scale bar is 500 nm. From ref. [33]

2.3.4 New hybrid methods

In an attempt to overcome the limitations of the aforementioned methods, new deposition methods have been developed recently that combine the advantages of top-down and bottom-up approaches. One simple example is the combination of the two approaches, most notably the patterning of the substrate prior to metallic nanoparticles deposition. The pattern in the substrate would serve as a grid for the controlled arrangement of the metallic nanoparticles onto the substrates. This method is highly promising since two or three dimensional arrangements can be easily obtained starting from spherical particles instead of the usual planar structures obtained from lithography. In spite of that, this deposition method does not tackle the main limitations of top-down methods, which are cost and total area of the substrate (typically in the range of a few μm^2). Therefore, in order to achieve large scale and cheap substrates, the use of clean room facilities should be avoided and metallic nanostructures should be obtained from easy synthetic methods with high yield and good size and shape control.

In our group, a hybrid deposition method based solely on bottom-up methods was developed, which guarantees the deposition of large scale (in the range of a few cm^2) plasmonic substrates with good control of interparticle distance and consequently of their optical response.[25] This deposition method relies on the combination of a few existing methods. At first metallic nanoparticles are synthetized in the desired size and shape by wet-chemical processes, then they are capped with a suitable mixture of alkanethiols. The capping molecule is

chosen in order to allow MNPs to maintain a controlled interparticle distance and to disperse well in a nonpolar solvent. The colloidal solution of alkanethiol capped MNPs in hexane:acetone (9:1 vol) is then used to perform electrodeposition of MNPs on a functionalized conductive substrate. The conductive substrate was functionalized with bi-functional molecules leaving a thiol moiety available for chemisorption of metallic nanoparticles. The deposition method does not only rely on electrophoresis, but it also takes advantage of the solvent evaporation effect. In fact, at the oil/air interface the supersaturated solution of metallic nanoparticles induces nucleation on the substrate. In addition, the slow motion of the meniscus favors the creation of an ordered monolayer, similar to the Langmuir-Blodgett liftoff method. After the solvent is completely evaporated, the substrate is annealed at 50 °C overnight to allow for the formation of the metal-S bond between MNPs and the substrate, guaranteeing a strong attachment of MNPs on the substrate.

2.4 Plasmonic substrates: applications

Although, as anticipated in the introduction, metallic nanoparticles and nanostructures can be applied in a vast range of fields, the focus of this work is mainly on the ability of metallic nanostructures to induce a strong near-field light that can make up for the low quantum efficiency of non-linear processes. The first example is also the best-known one and most-widespread application of plasmonic substrate, that is the enhancement of Raman scattering.[70,71] In addition, the application of plasmonic substrates for the enhancement of two-photon processes has also attracted a huge interest,[36–38,72] since it would allow the shift of the photoexcitation from the UV range (typical of many relevant photoreactions) to the visible range and the use of incoherent sources instead of high-power pulsed-lasers.

2.4.1 Surface-enhanced Raman spectroscopy

Raman scattering was first discovered by Raman in 1928, but its widespread application as a characterization tool was not possible until the development of micro-Raman spectroscopy. The limitations of Raman spectroscopy, in fact, are directly related to the weak Raman cross-section of most materials, which is usually in the range of $\sigma \approx 10^{-26} - 10^{-30}$ cm^2. When light excite an atom or a molecule, in fact, scattered light will be produced: this light mainly consists of elastically (Rayleigh) scattered light, with a minor contribution coming from inelastically scattered light. The frequency of the inelastically scattered light can either be lower or higher than that of the incident light, giving rise to Stokes and anti-Stokes Raman scattering, respectively. In Stokes (anti-Stokes) Raman scattering incident light excites the molecule from the ground state (excited state) to a virtual state, then the molecule relaxes to a higher energy vibrational state (to ground state) and emit a photon of lower (higher) energy.

In 1973 an extremely high Raman signal was detected from pyridine adsorbed on a chemically roughened silver electrode by Fleishmann and co-workers.[73] The origin of this enhancement was at first attributed to the higher density of molecules on the roughened electrode, thereof the name of surface-enhanced Raman scattering (SERS). Only a few years after, Van Duyne's group suggested that the origin of the enhancement could not be attributed solely to the increased density of molecules on the substrate, but an electromagnetic enhancement should play a major role in SERS signal.[74] At the same time, a chemical enhancement was also proposed to contribute to the SERS signal.[75] The theory of the electromagnetic enhancement was further refined by Moskovits,[71] who recognized that the origin of SERS enhancement was actually not related to a surface effect but to the presence of metallic nanostructures. Because of the huge enhancement of the Raman signal and the possibility to combine Raman apparatuses with microscopes for signal collection (micro-Raman), this technique has been soon recognized as highly promising for development of high sensitivity and high selectivity sensors.[76,77] In fact, SERS presents major advantages if compared with other well-established

and high sensitivity spectroscopic techniques such as fluorescence spectroscopy: it allows multiplexing,[78] recognition of structural properties[79] and structural changes of the analytes.[80] Nevertheless, up to now SERS has not been able to live up to its tremendous potential,[81] due to limitations in the fabrication of plasmonic substrates, in the understanding of their near-field properties, and, finally, due to the difficulty in the estimation of the exact enhancement factor. This latter issue, in fact, often led to reports claiming very high enhancement factors, often overestimated by 4 or 5 order of magnitude. Typical examples of this enhancement factor overestimation were found when resonance conditions were not taken into account properly (resonant Raman cross-section can be up to 6 orders of magnitude higher than its non-resonant counterpart) or when an unsuitable reference line is used (typically solvent lines, e.g. methanol).

2.4.2 Two-photon induced photoreactions

A multiphoton process occurs when a molecule is excited simultaneously by two or more photons via a virtual state. In order for mutiphoton processes to be observed, they require high peak powers, and molecules with high nonlinear cross-section. Multiphoton processes have been long known and studied, from the pioneering work of Göppert-Mayer in 1931,[82] who first discovered the possibility of the simultaneous absorption of two photon (Two-photon absorption, TPA), see Fig. 9. Her discovery gained new momentum when pulsed lasers became widely available and two-photon processes could be actively investigated.[83] For long time though the main application of TPA was limited in the field of spectroscopy. Recently application of multiphoton processes have been extended to photoreactions such as three-dimensional photopolimerization, due to the great spatial resolution that can be achieved (only area in the laser focus spot can undergo photoreaction) with this technique,[84] as shown in Fig. 10.

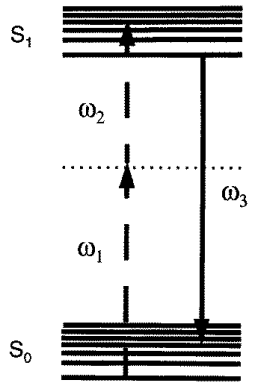

Figure 9 Energy level diagram showing the simultaneous absorption of two photons of frequency ω_1 and ω_2 through a virtual state denoted by the dotted line. If $\omega_1 \equiv \omega_2$ it represents the case of degenerate two-photon absorption. From ref. [35]

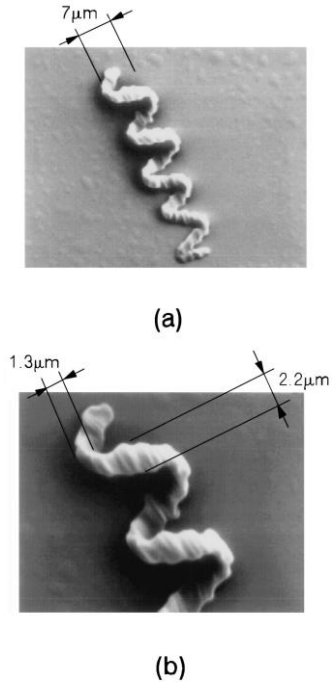

Figure 10 SEM image of a spiral structure made by two-photon microfabrication after removal of the unsolidified resin: (a) view of the entire structure, (b) magnified view. From ref.[84]

Following the success of two-photon-initiated photopolimerization, other applications of multiphoton processes were proposed, such as ultra-high-resolution optical microscopy,[85] 3D ultra-high density optical data storage,[86] and TPA-induced photoreactions.[87] Although the aforementioned examples were first observed with ultra-high power pulsed laser excitation, a few reports of TPA-induced photoreactions under irradiation with conventional lamps could be found.[37,39] Up to now, though, these results were limited to compounds with very large nonlinear cross-section and of little or no interest for organic synthesis. In this work the application of plasmonic-enhanced TPA-induced photoreaction to a different compound (anthracene carboxylic acid) is performed, in order to prove the generality of this photoreaction process.

2.4.3 TPA-based photosensitization of wide-bandgap semiconductors

One of the main issue nowadays is to find an efficient way to convert solar light into chemical energy. One of the most promising path is to produce hydrogen by photocatalytic water splitting. The most famous material for this purpose is titania. A titania photoanode, in fact, can generate an electron-hole pair when light in the UV region impinges on it. Large titania bandgap though inhibits its use for solar water splitting, since UV light is only 5% of the solar spectrum. To overcome such problem a few different approaches have been proposed. One possible approach consists in replacing the oxide semiconductors with multiple semiconductor tandem cells. Tandem cells will collect light in a vast range of the solar spectrum and perform water splitting without external voltage applied.[88] The main problem of this approach though is high cost and lack of resistance to corrosion of conventional semiconductor solar cells. The second and most common approach is to dope the oxide semiconductor to decrease its bandgap.[89] This will lead to an increase in visible light activity, but at the same time to an increase of electron-hole pair recombination due to scattering with impurities. The third approach is to load the oxide semiconductor with a co-catalyst, such as platinum.[90] Unfortunately, this strategy will lead not only to a beneficial increase in oxygen and hydrogen evolution near the co-catalyst/titania interface, but also to an increment in the pair recombination outside the boundary between the semiconductor and the co-catalyst, which limits its application. The fourth approach is to photosensitize the material, as for Grätzel cells,[91] in this case the photosensitizer is excited from the ground state to an excited state by the incident

visible light, and the excited electron is then injected in the conduction band of the wide-bandgap semiconductor. The main problem of this approach is that it usually decreases the UV activity of the semiconductor due to screening and, in addition, degradation of the dye is a serious issue.

Apart from organic dyes, a different class of photosensitizers has been recently applied to wide-bandgap semiconductors, which consists of metallic nanoparticles. Metallic nanoparticles are not only able to transfer charge to the semiconductor, but have additional interesting optical properties. Metallic nanostructures can in fact increase visible light activity in semiconductors (not only wide-bandgap semiconductors) though multiple non-exclusive mechanisms, as shown in Fig. 11: scattering with metallic nanoparticles can increase the light path of incident radiation and therefore the probability of electron-hole pair creation, and, in addition, metallic nanparticles and metallic nanostructures can increase the semiconductor performance through near-field enhancement.

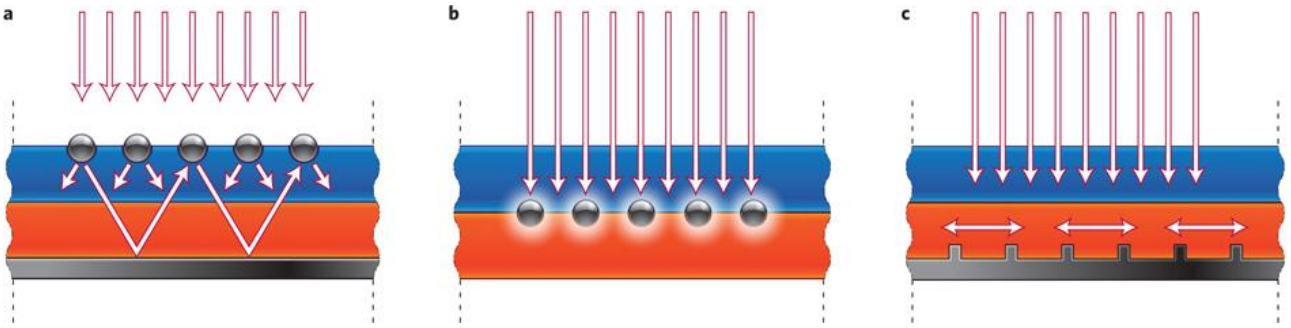

Figure 11 Plasmonic light-trapping geometries for thin-film solar cells. a) Light trapping by scattering from metal nanoparticles at the surface of the solar cell. Light is preferentially scattered and trapped into the semiconductor thin film by multiple and high-angle scattering, causing an increase in the effective optical path length in the cell. b) Light trapping by the excitation of localized surface plasmons in metal nanoparticles embedded in the semiconductor. The excited particles' near-field causes the creation of electron–hole pairs in the semiconductor. c) Light trapping by the excitation of surface plasmon polaritons at the metal/semiconductor interface. A corrugated metal back surface couples light to surface plasmon polariton or photonic modes that propagate in the plane of the semiconductor layer. From ref.[8]

In case of wide bandgap semiconductors, anyway, the first mechanism is not effective for visible light radiation, because increasing the light path inside the semiconductor will not induce electron-hole pair production since the semiconductor is transparent in the visible region. In order to achieve visible light activity the near-field properties of metallic nanostructures have to be exploited. As already anticipated, when nanoparticles are excited at resonant conditions, a strong near field light is produced in their proximity. This resonant excitation was postulated to modify the response of the wide-semiconductor in various ways. One possible mechanism can consist in the plasmon induced "hot electrons"[92] transfer from the metallic nanoparticle to the semiconductor.[93] In normal condition such transfer is prohibited, due to the Schottky barrier between the metallic nanoparticle and the semiconductor, but the plasmon decay can contribute to the energy needed to overcome the barrier and induce the charge transfer, as shown in Fig. 12.

Another possible mechanism is also related to the non-radiative decay of nanoparticles plasmons, that is LSPR heating.[94] LSPR decay was proven, for example, to induce crystallization of titania under resonant excitation.[95] This process, anyway, can be usually neglected at solar power, or under irradiation with wide-band incoherent sources (Xe lamps or W lamps), that are the target of this research.

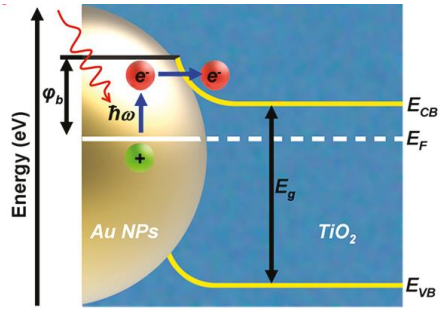

Figure 12 Plasmonic photosensitization of TiO_2 through "hot electron" transfer. Schematic illustrating the band-bending effect of the Schottky junction between Au NP and the TiO2 layer surrounding it. Band bending creates an energy barrier which allows an electron excited by an incoming photon of energy ħω from a filled to an empty level of the metal's conduction band to tunnel directly into the conduction band (E_{CB}) of the TiO2. From ref. [93]

Furthermore metal nanoparticles act as sinks for electrons avoiding fast recombination.[89]

Apart from non-radiative plasmon decay, the near-field produced by metallic nanoparticles can also affect the response of titania. In case of metallic nanoparticles whose enhancement is peaked at the same wavelength of the absorption of the wide bandgap semiconductor, the metallic nanoparticle can directly enhance the one-photon activity of the semiconductor. A typical example of this mechanism is titania over silver nanoparticles; silver nanoparticles in fact show strong enhancement in the UV and blue region of the spectrum, therefore they can affect UV (one-photon) activity of titania.[96] This mechanism is indeed interesting, but it does not improve the visible light activity of the material. Therefore, a different approach is needed in order to shift the range of activity of the material from the UV to the visible range without modifying directly the material by doping. A possible implementation of this strategy is to produce an e/h pair by simultaneous absorption of two photon of about half energy, with a two-photon absorption process. As stated above, nonlinear processes have very small quantum efficiency, therefore they can be neglected at standard conditions, but the strong enhancement produced by metallic nanostructures when excited at resonant conditions can overcome this limitation. To achieve the e/h pair formation upon simultaneous absorption of two photons it is therefore necessary to design of a plasmonic structure whose LSPR does not lay near the energy of the bandgap of titania, but near half its value (twice he wavelength).

3. Experimental

3.1 Materials and methods

3.1.1 General

Plastic formed carbon counter electrodes were purchased from Tsukuba Materials Information Laboratory Ltd. (TMIL) and used after cutting and cleaning by sonication in DI water and hexane. 2-Anthracene carboxylic acid (ACA), 9,10-anthraquinone 2-carboxylic acid (AQCA), hexadecyltrimethylammonium bromide (CTAB), and 1-hexanethiol were purchased from TCI. 1,6-Hexanedithiol (Hexdt), and chlorauric acid trihydrate were purchased from Sigma-Aldrich. 2-Anthracene carboxylic acid (ACA), 9,10-anthraquinone 2-carboxylic acid (AQCA), hexadecyltrimethylammonium bromide (CTAB), and 1-hexanethiol were purchased from TCI. 1,6-Hexanedithiol (Hexdt), and chlorauric acid trihydrate were purchased from Sigma-Aldrich. All other chemicals were purchased from Nacalai-Tesque. All chemicals were guaranteed reagent grade and were used as received. Ultrapure water (Milli-Q by Millipore Co., 18.2 MΩ cm) was used throughout the experiments.

3.1.2 Substrate preparation

Gold substrate Quartz substrates (1 × 1 cm^2) were cleaned by immersion for 15 min at RT in fresh piranha solution (H_2SO_4 30%: H_2O_2 = 2:1 v/v; handle with care: piranha solution is highly corrosive and reacts violently with organic matter) and rinsed three times with milli-Q water. Quartz substrates were then coated with Cr (10 nm) (adhesion layer) and Au (40 nm) by electron beam deposition. Afterwards, samples were UV-ozone cleaned for 3 hours and later immersed in a 1% v/v solution of Hexdt in ethanol for 12 h, rinsed with 2-propanol (IPA) three times and dried with a nitrogen stream.

ITO substrate Quartz substrates (1 × 1 cm^2) were cleaned by immersion for 15 min at RT in fresh piranha solution (H_2SO_4 30%: H_2O_2 = 2:1 v/v; handle with care: piranha solution is highly corrosive and reacts violently with organic matter) and rinsing three times with milli-Q water. Quartz substrates were then coated with ITO (10 nm) by radio-frequency sputtering deposition at room temperature. Afterwards, samples were UV-ozone cleaned for 3 hours (final bulk resistivity of 1.1 $\times 10^{-3}$ Ωcm). The substrates were immersed in a 1% v/v solution of 3-mercaptopropyltrimethoxysilane (MPTMS) in toluene for 40 h, rinsed with methanol three times and dried with a nitrogen stream. Afterwards, substrates were immersed in a 1% v/v solution of 1,6-hexanedithiol (Hexdt) in ethanol for 12 h, rinsed with acetone three times and dried with a nitrogen stream.

3.1.3 Gold nanoparticles synthesis

10 nm gold nanoparticles Small gold nanoparticles were synthesized by a seed-mediated method[97] from a (3.5 ± 0.7) nm seed. A 0.12 mL of an ice-cold 0.1 M aqueous $NaBH_4$ solution was added to a 4 mL aqueous solution containing 2.5 × 10^{-4} M $HAuCl_4 \cdot 3H_2O$ and 2.5 × 10^{-4} M trisodium citrate while continuously stirring. The growth solution was prepared by adding 0.2 mL of a 50 mM solution of $HAuCl_4 \cdot 3H_2O$ to 39.8 mL of milli-Q water. Then 1.2 g of solid CTAB was added to the solution to reach a final concentration of 0.08 M. The solution was then stored in an incubator at 40 °C until it turned to an orange color and finally cooled to RT before use. To obtain a final size of 10 nm, a 2.07 mL of seed solution were added to a pre-prepared solution of 99.5 μL of freshly prepared 0.1 M ascorbic acid solution and 17.83 mL of growth solution. The extinction spectrum of the solution is shown in Fig. 13.

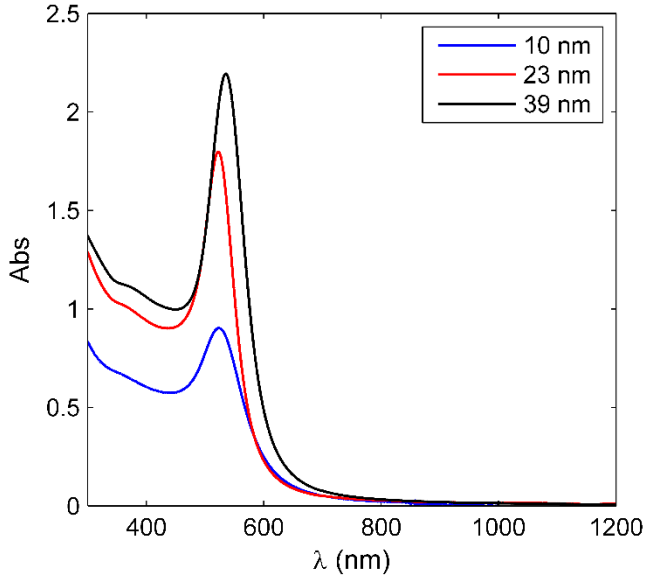

Figure 13 Extinction spectra of 10 nm (blue line), 23 nm (red line), 39 nm (black line) colloidal solutions.

36 nm gold nanoparticles Gold nanoparticles (AuNPs) with 36 nm diameter were synthesized by a citrate reduction method (average size 36 nm ± 6):[98] a 100 mL solution of 0.5 mM $HAuCl_4 \cdot 3H_2O$ was brought to boiling in a round bottom flask while continuously stirring, then 5 mL of a 38.8 mM aqueous sodium citrate solution were added at once. The solution was refluxed for 20 min to allow complete reduction (solution turned wine red). The extinction spectrum of the colloidal solution of AuNPs is shown in Fig. 14.

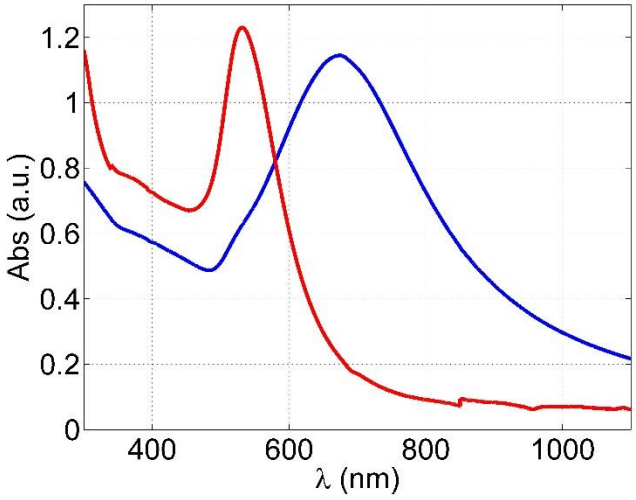

Figure 14 Extinction spectra of 36 nm citrate capped AuNPs in water solution (red line) and 2D array of 36 nm AuNPs capped with hexanethiol:dodecanethiol on MPTMS-Hexdt functionalized ITO substrate (blue line).

20, 23, 39, 40 nm gold nanoparticles In order to have a sharper size distribution, another synthetic method was later employed for "large" gold nanoparticles (AuNPs). The nanoparticles referred as 20, 23, 39 and 40 nm AuNPs were synthesized by a different seed-mediated growth method[99] from a 13 nm seed. At first a gold seed solution was prepared by the citrate reduction method[98] (average size 13 nm ± 1.5). The solution was refluxed for 20 min to allow complete reduction. The colloidal solution was left to cool slowly and then used as the seed solution to obtain larger gold nanoparticles.

To prepare the growth solution, 0.8 mL of 20 mM aqueous $HAuCl_4 \cdot 3H_2O$ solution and 80 µL of 10 mM aqueous $AgNO_3$ solution were added to 34 mL of milli-Q water. To obtain the desired final size 6.35 mL (20 nm), 6.12 mL (23 nm AuNPs) or 0.6 mL (39 nm or 40 nm AuNPs) of seed solution were added to the growth solution while stirring vigorously and 6 mL of aqueous ascorbic acid solution (5.3 mM) was added dropwise (feeding rate 0.6 mL/min) to the solution by means of a mechanical syringe pump (KdScientific). The extinction spectra of the colloidal solutions of 23 and 39 nm AuNPs are shown in Fig. 13.

Au@Ag core-shell nanoparticles Ag@AuNPs were synthesized by a seed-growth method (modified from literature) to obtain various final sizes. With this method, particles size and composition could be controlled by varying the Au to Ag molar ratio. After the synthesis of 20 and 40 nm AuNP core following the method described in previous section, Ag@AuNPs were obtained following a seed-growth method.[28] By adding $AgNO_3$ and ascorbic acid to the colloidal solution of AuNPs, Ag is reduced on the surface of AuNPs to form a uniform shell around the gold core. A given amount of 5 mM $AgNO_3$ was added dropwise with a mechanical syringe (feeding rate= 0.4 mL/min) into 10 mL of AuNP solution containing ascorbic acid (see Table 1) to obtain MNPs with Ag to Au molar ratio ranging from 0.4 to 3. The growth of the silver shell was also confirmed by UV-Vis spectroscopy, see Fig. 15.

Table 1

Au core d (nm)	Concentration of Au sol [mM]	Ag:Au molar ratio	$AgNO_3$ mL	Ascorbic acid mL	Expected d (nm)
20.00	0.41	0.40	0.33	0.17	22.40
20.00	0.41	0.70	0.58	0.29	23.90
20.00	0.41	1.00	0.82	0.41	25.20
20.00	0.41	3.00	2.50	1.25	31.80
40.00	0.39	0.40	0.32	0.16	44.80
40.00	0.39	0.70	0.55	0.28	47.70
40.00	0.39	1.00	0.79	0.40	50.40
40.00	0.39	3.00	2.40	1.20	63.70

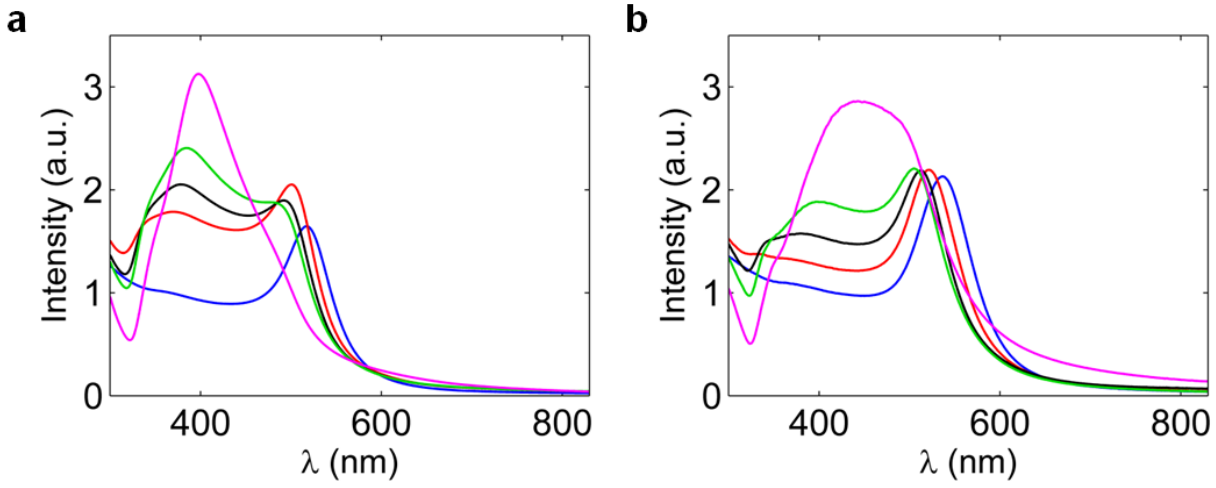

Figure 15 Experimental extinction spectra of colloidal solution of a) 20AuNPs (blue line), 20Au@Ag0.4 NPs (red line), 20Au@Ag0.7 NPs (black line), 20Au@Ag1 NPs (green line), 20Au@Ag3 NPs (magenta line), and b) 40AuNPs (blue line), 40Au@Ag0.4 NPs (red line), 40Au@Ag0.7 NPs (black line), 40Au@Ag1 NPs (green line), 40Au@Ag3 NPs (magenta line).

Alkanethiol-capped MNPs MNPs were then capped with alkanethiols:[39] the colloidal solution of 10 nm AuNPs was mixed with a 0.55% v/v dodecanethiol solution (10 mL) in acetone. The colloidal solution of larger AuNPs and Au@Ag NPs was mixed with a 0.55% v/v solution of hexanethiol:dodecanethiol = 3:1 (10 mL) in acetone. Stirring was performed for 12 h at RT, then alkanethiol-capped AuNPs were extracted with methanol and hexane and purified by sequential centrifuge and redispersion into hexane three times.

3.1.4 2D array deposition

The 2D array of AuNPs was deposited on a gold substrates by means of a hybrid method developed by our laboratory (see Fig. 16).[25] Briefly, a dithiol-functionalized gold substrate was used as a cathode, while a plastic carbon electrode was used as an anode. The distance between the electrodes was kept at 1.2 mm, while the voltage applied was 1.1 V. Alkanethiol-capped AuNPs were redispersed in a 2 mL hexane:acetone (10:1 v/v) solution. The electrodes were immersed in the colloidal solution (in a 3 mL plastic vessel) and left in a nitrogen-purged environment until complete evaporation of the solvent took place. Afterwards, samples were put on a hot plate at 50 °C for 24 h to induce chemisorptions of the AuNPs on the substrate and finally they were sonicated for 20 s to remove multilayers of MNPs.

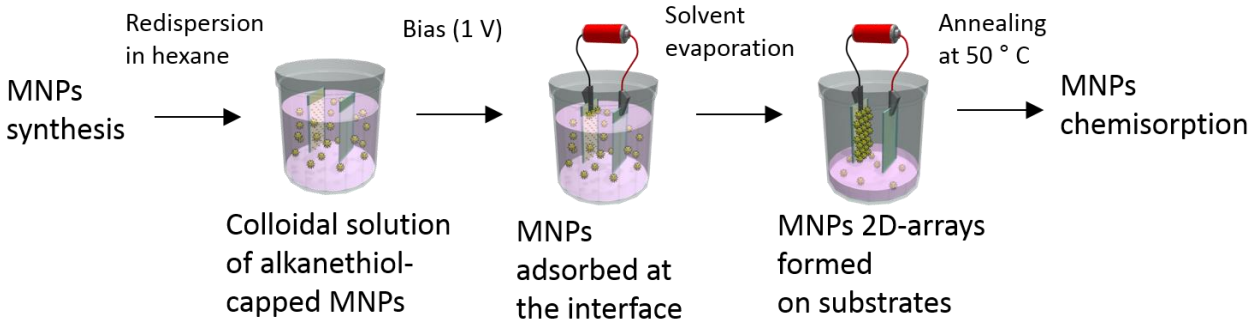

Figure 16 Flow chart of 2D array deposition process by hybrid method.

3.2 Characterization methods

3.2.1 General

Extinction spectra were recorded with a double beam spectrometer Jasco V-670 equipped with liquid cell holder module for solution samples, a transmission module for solid samples (for ITO substrates) and a specular reflection module (for gold substrates). Raman measurements were performed with a Horiba Jobin-Yvon T-64000 micro-Raman spectrometer equipped with a He/Ne laser (632.8 nm excitation line was used) and a Ar/Kr laset (514 nm), and a liquid nitrogen cooled CCD detector (for titania and anthracene characterization) or a Peltier-cooled (−80 °C) detector (Andor) (for Rhodamine 6G SERS measurements).

The micro-Raman was equipped with a 45× (0.55 NA) and 90× (0.7 NA) Plan APO Super Long Working Distance (SLWD) objective lenses (Photon Design). To realize high throughput, a holographic notch filter was used for laser line rejection, and a single spectrograph with 1800 gr/mm grating was used to disperse Raman

light. Laser power at the sample was measured on a Si photodiode power meter (Thorlabs Inc. S120VC, wavelength range 200-1100 nm) power meter.

^{1}H, and ^{13}C spectra were recorded on JEOL JNM-AL300 and JNM-ECS400 spectrometers. Mass spectra were measured by Fourier transformation-ion cyclotron resonance-mass spectrometry (FT-ICR-MS) coupled with electron spray ionization (ESI) technique using a SolariX FT-ICR-MS spectrometer (Bruker Daltonics GmbH).

SEM images were acquired with a Hitachi S-4800 FE-SEM. SAXS measurements were performed using beamline BL40B2 with synchrotron radiation at SPring-8, Japan. XRD pattern was obtained with a RIGAKU RINT2000 Ultima-III. TEM micrographs were obtained with a JEOL JEM 2100-F, contact angle measurements were performed with a Kyowa DM500 contact angle meter. AFM images were acquired with a SII NanoTechnology L-Trace AFM in tapping mode with an Si cantilever.

An Asahi-Spectra 300 W Xe lamp (Max-302) equipped with UV (250–385 nm), Vis (385–740 nm) and IR (750–1050 nm) mirrors modules and a visible bandpass filter (422–750 nm) was used for the photoreaction experiments. Laser power and Xe lamp power (for low incident power) was measured on a Si photodiode (Thorlabs Inc. S120VC, wavelength range 200–1100 nm) power meter. Xe lamp power (high incident power) was measured with a thermal power sensor (Thorlabs Inc. S302C).

Simulations of Raman spectra were performed by DFT calculation and carried out using Gaussian 03 program.[100] Simulation of extinction spectra and near-field response of metallic nanoparticles were performed with DDSCAT 7.3.[58–60]

3.2.2 Morphological characterization

In order to evaluate the optical properties and potential application of the 2D arrays of metallic nanoparticles, various metallic nanoparticles were synthetized (different metallic composition and final diameter). The morphology of various MNPs was characterized by SEM, TEM, HRTEM and EDX. For SEM characterization, the MNPs were immobilized on a conductive substrate, such as gold or ITO substrate, while for TEM measurements MNPs in water solution were dropcasted on a carbon-coated copper grid and dried in a vacuum box overnight. From the morphological characterization the average size of the MNPs was determined: for small nanoparticles (diameter below 30 nm) the average size was extracted from TEM micrographs, while for larger particles SEM images were used to evaluate the MNPs average size and size distribution. Although various MNPs were employed in this work, AuNPs and core-shell Au@Ag NPs were considered as the most interesting and promising nanostructures, since they are easy to produce in a wide range of sizes by simple wet-chemical processes.

In order to study carefully the optical response as a function of final MNP diameter, metallic composition and aggregation properties, two sets of AuNPs were synthetized, 20 nm and 40 nm in diameter, and then used as the core for the synthesis of Au@Ag NPs with different Ag shell thicknesses.

The results of MNPs characterization for one set of AuNPs and Au@Ag NPs are shown in Fig. 17 and 18 and summarized in Table 2.

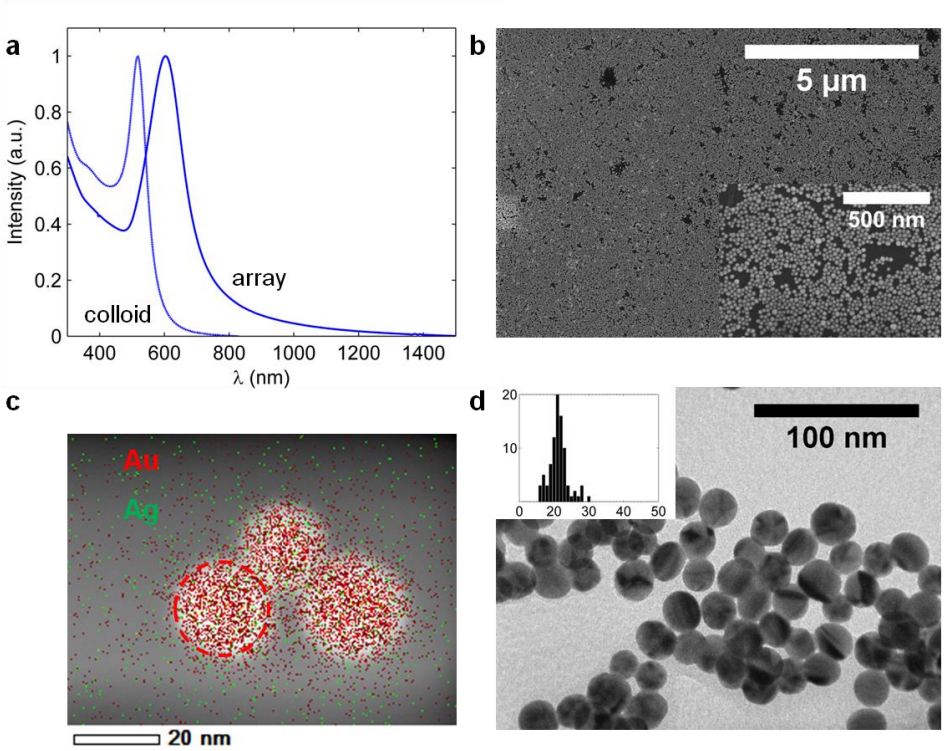

Figure 17 a) Extinction spectra of colloidal and arrayed 20AuNPs, b) SEM micrograph of 2D array of 20AuNPs, inset: higher magnification c) EDX map of 20AuNPs and d) TEM image of 20AuNPs, inset: histogram of size distribution of 20AuNPs, average d= 21 ± 1.5 nm.

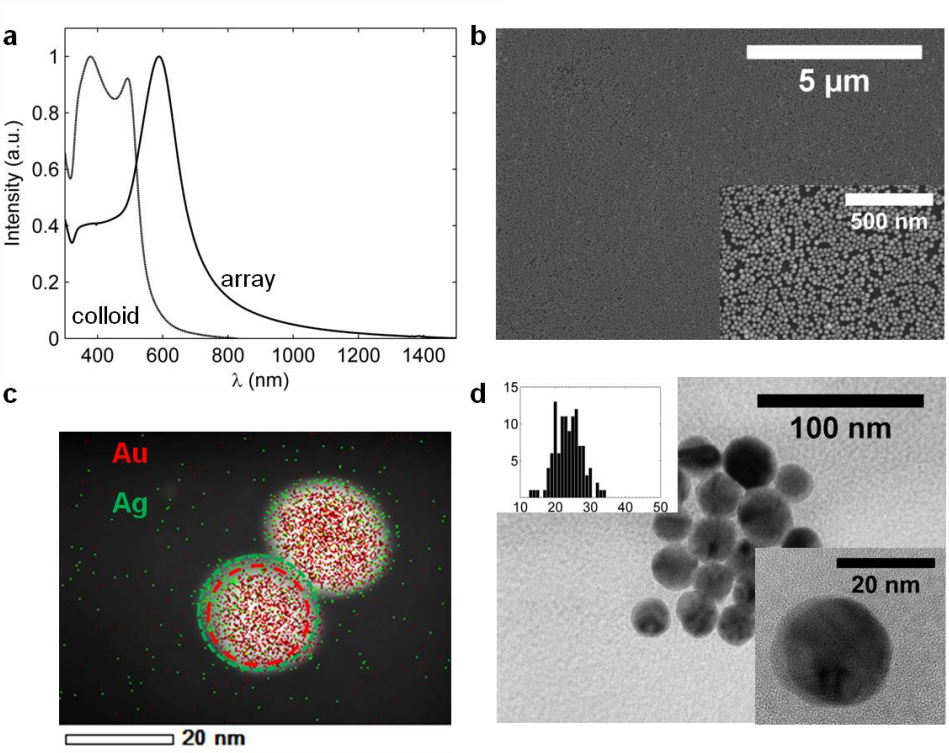

Figure 18 a) Extinction spectra of colloidal and arrayed 20Au@Ag$_{0.7}$ NPs, b) SEM micrograph of 2D array of 20Au@Ag$_{0.7}$ NPs, inset: higher magnification c) EDX map of 20Au@Ag$_{0.7}$ NPs and d) TEM micrograph of 20Au@Ag$_{0.7}$ NPs, top inset: histogram of size distribution of 20Au@Ag$_{0.7}$ NPs, average d= 25 ± 3.5 nm, bottom inset: HRTEM micrograph of 20Au@Ag$_{0.7}$ NP.

Table 2

Expected size d (nm)	Average size d (nm)	std (nm)	2D array coverage
20	21	1.5	70%
22.4	23	2.5	76%
23.9	25	3.5	79%
25.2	26	4	71%
31.8	34	4	67%
40	38	3	58%
44.8	41	5	61%
47.7	47	4	60%
50.4	53	5	60%
63.7	63	7	55%

As a result, AuNPs and Au@Ag NPs showed a quite sharp size distribution (standard deviation of MNPs' diameter is not larger than 14% of the average diameter) for all MNPs. For what concerns the shape of the MNps, a small number of core-shell nanorods and different nanoparticles shapes was found in case of large core (40 nm) and thick Ag shell (1:1 and 3:1 Ag:Au ratio). In addition, from EDX maps and HRTEM micrographs, the Ag shell is proven to grow as a quite uniform layer around the Au core (although non-perfectly concentric at large Ag shell thicknesses).

The formation of a dense 2D array of MNPs was verified by SEM, as shown in Fig. 17b, 18b. From SEM micrographs the MNPs coverage was estimated (from various points on the sample); the results of such analysis are summarized in Table 1. The interparticle distance for similar 2D arrays of alkanethiol-capped MNPs on ITO substrate was previously determined by means of SEM and SAXS measurement[25] to be 2.4 nm, due to alkyl chain interdigitation. After confirmation of the successful deposition of a dense monolayer of MNPs, the far-field optical properties of the various 2D arrays were investigated with UV-Vis spectroscopy, as shown in Fig. 17a, 18a.

3.2.3 Optical characterization

Once morphological properties of MNPs were characterized, the optical response of gold and core-shell nanoparticles in colloidal solution was evaluated. Extinction spectra of gold and core-shell Au@Ag NPs prepared from 20 nm gold core and 40 nm gold core are shown in Fig. 15a,b (20 nm core and 40 nm core, respectively). Then MNPs were capped with alkanethiols and deposited on a conductive substrate (ITO or gold).

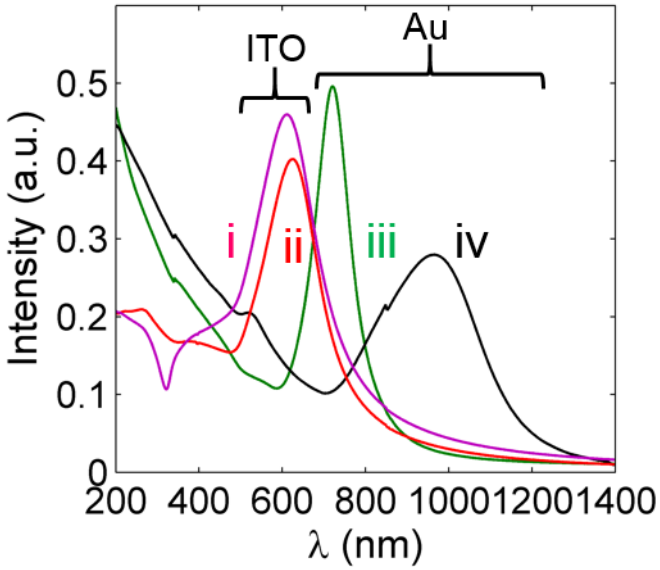

Figure 19 Extinction spectra of i) 20Au@Ag NPs (3:1 Ag:Au ratio) 2D array on ITO, ii) 20 nm AuNPs 2D array on ITO, iii) 20 AuNPs 2D array on gold, iv) 39 AuNPs 2D array on gold.

From Fig. 19, it can be observed that 2D arrays whose LSPR ranged from the visible (orange) to the NIR region could be obtained just by changing the metallic composition of the MNPs and the substrate (gold or ITO). In addition, from comparison of the same MNPs (20 nm AuNPs) on different substrates the effect of the substrate on the position of the LSPR could be determined. LSPR of AuNPs 2D array deposited on gold is in fact redshifted of 110 nm if compared to the same 2D array on ITO. This effect is due to the different material and therefore dielectric constant of the two substrates. For all substrates, the metallic nanoparticles can interact with the image charges in the substrate, and this interaction depends on the dielectric constant of the substrate[101] though the factor $(\varepsilon - 1)/(\varepsilon + 1)$.[17] This interaction, weak for dielectric substrates and stronger for metallic film, has the effect of redshifting the modes of the nanoparticle when light polarized perpendicular to the metallic film is incident on the sample. Furthermore, the modes of the nanoparticles can couple to the surface plasmons of the metallic film, and this coupling depends on the surface plasmon frequency of the metallic film and its thickness (density of states). The different behavior of gold and ITO can be intuitively explained by the different coupling of the MNPs with the two substrates. Surface plasmon resonance of gold lies at higher frequency than the MNPs modes and the film is thicker that the MNP diameter, therefore the interaction can fall in the regime of thick metallic films giving a redshift of the LSPR, while for ITO film the surface plasmon lies at lower frequencies (ω_{sp}~0.76 eV),[102] and the thickness of the film is smaller (t=10 nm, half of the MNP diameter) than the MNP diameter, giving as a result a broadened LSPR with no (or negligible blueshift) shift in position.[51]

The effect of the metallic composition and final size of the nanoparticles was also studied. Considering 2D arrays of AuNPs and Au@Ag NPs on ITO only (Fig. 20), it can be noticed that the main LSPR peak in the 2D array depends on the MNP final size and composition (Ag:Au ratio). In details, the most intense LSPR peak shows a small blueshift from the starting core NP (LSPR=603 nm for 20 nm AuNP) to the larger Au@Ag (LSPR=577 nm for 20Au@Ag_3). The same tendency can be seen for larger Au@Ag NPs prepared from 40 nm gold core, in this case a gradual blueshift can be observed from the 40 AuNPs 2D array (LSPR=688 nm) to the 40Au@Ag_3 NPs 2D array (LSPR=635 nm).

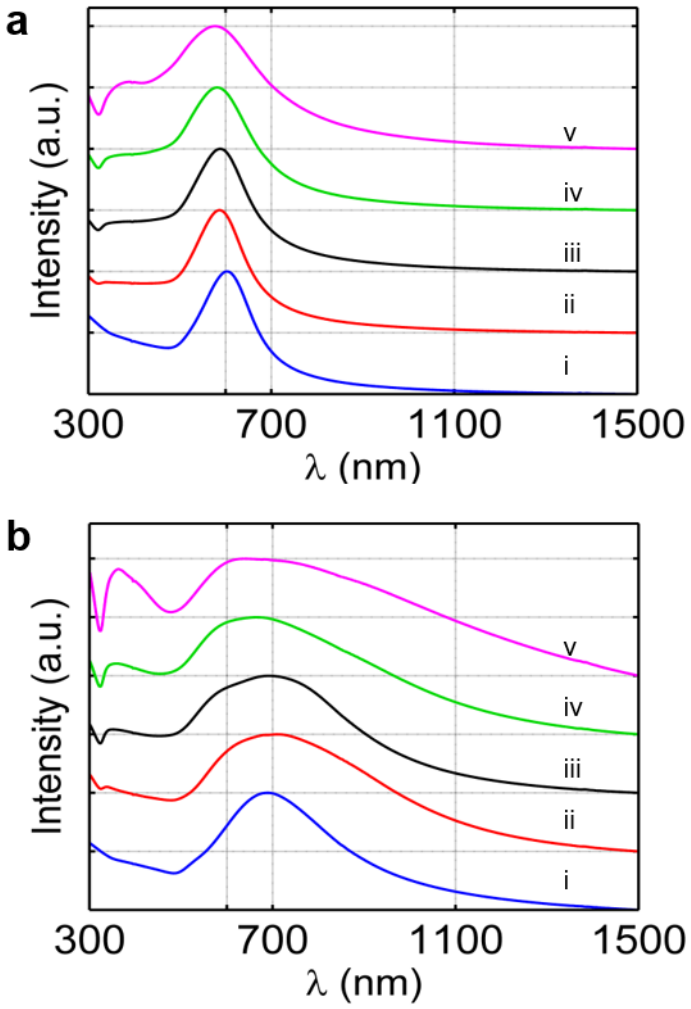

Figure 20 a) Extinction spectra of i) 20AuNPs, ii) 20Au@$Ag_{0.4}$ NPs, iii) 20Au@$Ag_{0.7}$ NPs, iv) 20Au@Ag_1 NPs, v) 20Au@Ag_3 NPs, b) extinction spectra of i) 40AuNPs, ii) 40Au@$Ag_{0.4}$ NPs, iii) 40Au@$Ag_{0.7}$ NPs, iv) 40Au@Ag_1 NPs, v) 40Au@Ag_3 NPs. Each spectrum is normalized to its maximum value and shifted for clarity.

3.2.4 Discrete-dipole simulations

DDA is a powerful method to compute extinction spectra (scattering and absorption) of objects of arbitrary geometries and with the additional advantage of using experimental values of dielectric constants to model the objects. DDA code DDSCAT 7.3 was employed to compute both far-field extinction (scattering and absorption) spectra, and electric near-field inside and in the proximity of noble metallic (Au) and bimetallic (concentric Ag-shell and Au-core) nanoparticle and their assemblies. For our DDA calculations, the aforementioned MNPs and their assemblies were modelled as spherical particles surrounded by air or water without taking into account both adsorbates (alkanethiol on MNPs surface) and substrates. Values reported by Johnson and Christy [103] were used as refractive index of gold and silver. For refractive index of ambient media, values reported by Hale and Querry[104] were used as medium refractive index of water for the metallic NPs in aqueous solution, while refractive index of air was set to 1.0. Because of large refractive index of Au and Ag in the visible light region, filtered coupled dipole method was used to compute dipole polarizability.[105] It was reported in fact that filtered coupled dipole method outperforms lattice dispersion method (also known as point dipole method) when computation includes high index materials[106] such as Ag and Au, and it provides higher accuracy and faster convergence. Calculation volume including NP(s) was discretized by 0.5 nm of interdipole spacing. Gap between adjacent particles was set to 3.0 nm for all calculations of NPs assemblies. The

parameters (core and final radius of MNP) relative to all MNPs models employed throughout this work are listed in Table 3. It is to be stresses that, due to computational limitations, a trimer of MNPs was used to model our 2D arrays, instead of la larger assembly of nearly close-packed MNPs.

Table 3

Sample	Core size d (nm)	Ag shell thickness (nm)	Final size d (nm)
20 Au	20	0	20
20Au@Ag$_{0.4}$	20	1	22
20Au@Ag$_{0.7}$	20	2	24
20Au@Ag$_{1}$	20	2.5	25
20Au@Ag$_{3}$	20	6	32
40 Au	40	0	40
40Au@Ag$_{0.4}$	40	1.5	43
40Au@Ag$_{0.7}$	40	3	46
40Au@Ag$_{1}$	40	4.5	49
40Au@Ag$_{3}$	40	10.5	61

In Fig. 21, the comparison of experimental extinction spectra and simulated extinction efficiency (total extinction divided by volume of the nanoparticle) is shown for both colloidal solution and isolated nanoparticles (single particle in the simulations). As it can be noticed, a very good agreement was found between experimental and simulated values, confirming the validity of the models for single particles. This step was necessary to apply the simulations for more complex structures, such as nanoparticles aggregates, which can convey information about the near-field behavior of our samples. In Fig. 22,23 the near-field pattern of various MNPs trimers is shown as a function of the silver shell thickness, for both 20 nm and 40 nm AuNPs as core. As expected, the strong near-field enhancement is located predominantly in the gap between the nanoparticles along the field polarization direction.

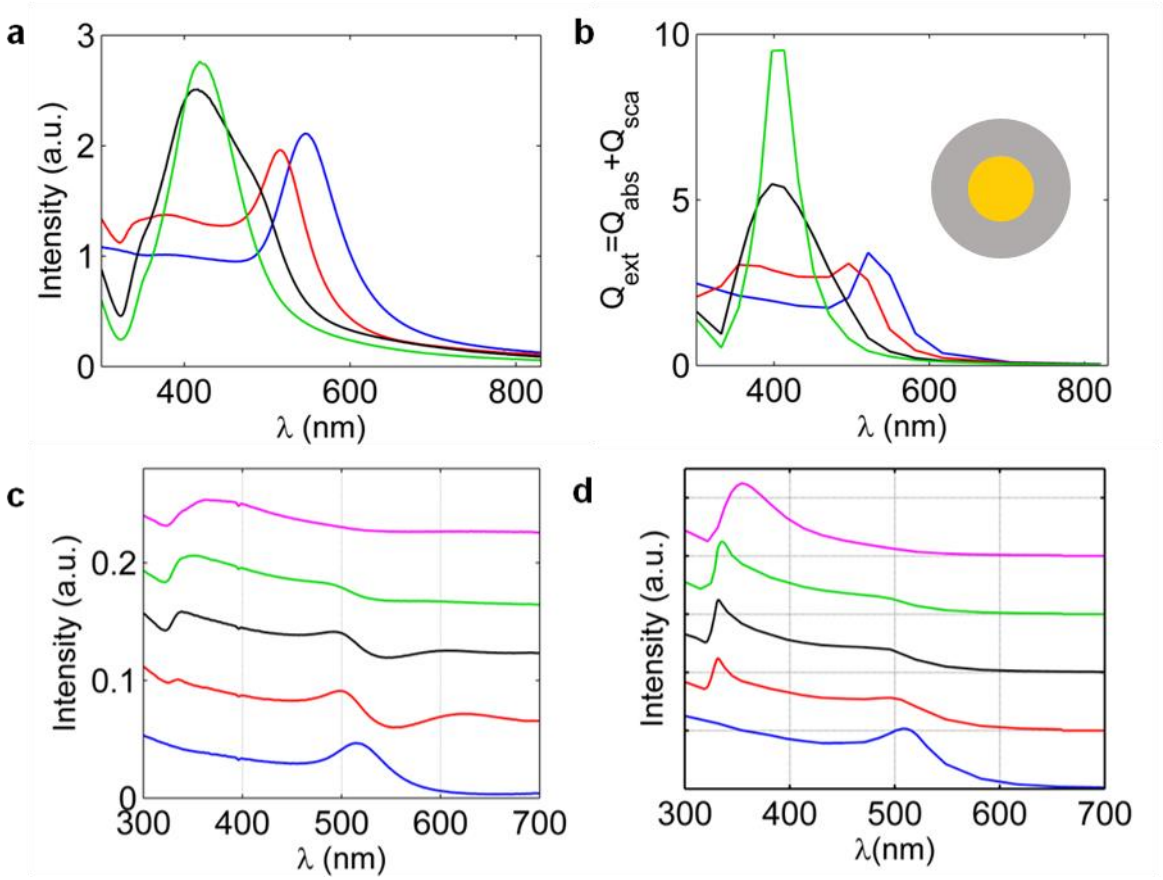

Figure 21 a) Experimental extinction spectra of colloidal solution of 46AuNPs (blue line), 40Au@Ag NPs with final diameter d=46 nm (red line), 30Au@Ag NPs with final diameter d=46 nm (black line), 20Au@Ag NPs with final diameter d=46 nm (green line), and b) simulated extinction spectra of colloidal solution of 46AuNPs (blue line), 40Au@Ag NPs with final diameter d=46 nm (red line), 30Au@Ag NPs with final diameter d=46 nm (black line), 20Au@Ag NPs with final diameter d=46 nm (green line), c) experimental extinction spectra of isolated 40AuNPs (blue line), 40Au@$Ag_{0.4}$ NPs (red line), 40Au@$Ag_{0.7}$ NPs (black line), 40Au@Ag_1 NPs (green line), 40Au@Ag_3 NPs (magenta line) on a ITO substrate and d) simulated extinction spectra of single nanoparticles in air: 40AuNPs (blue line), 40Au@$Ag_{0.4}$ NPs (red line), 40Au@$Ag_{0.7}$ NPs (black line), 40Au@Ag_1 NPs (green line), 40Au@Ag_3 NPs (magenta line).

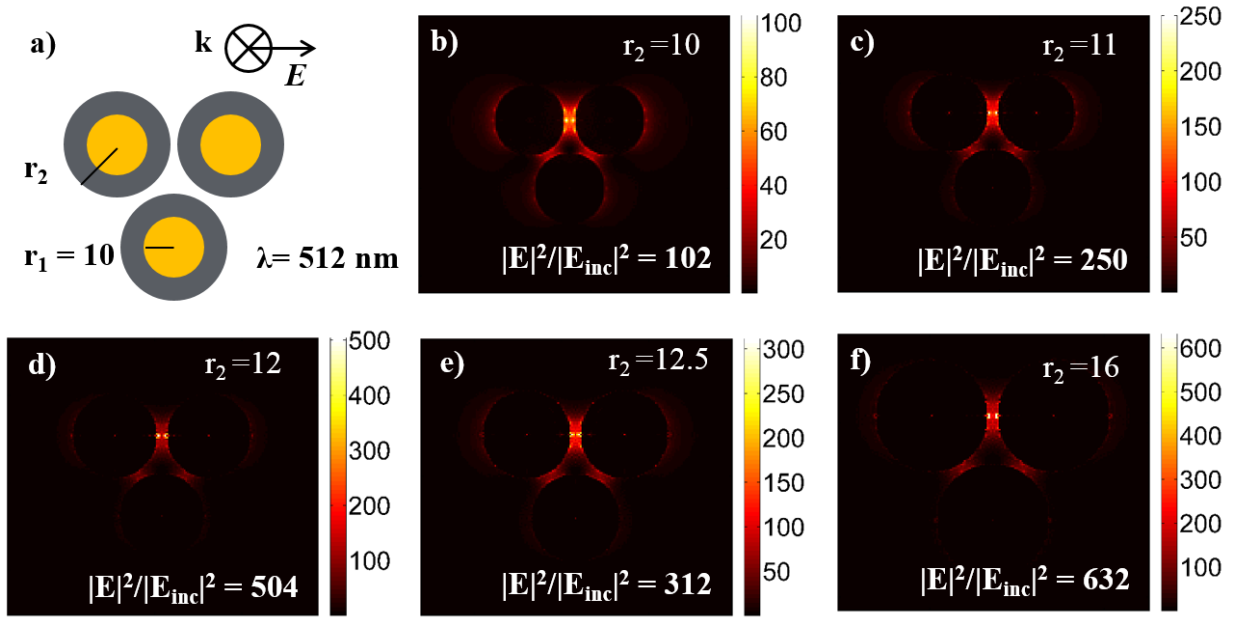

Figure 22 a) Schematic draw of the trimer and the polarization direction of the field. Map of near-field intensity $|\boldsymbol{E}|^2/|\boldsymbol{E_{inc}}|^2$ *at 512 nm incident wavelength of b) 20Au@Ag, c) 20Au@Ag0.4, d) 20Au@Ag0.7, e) 20Au@Ag1, and f) 20Au@Ag3 NPs. In each figure the value of the maximum field enhancement is reported in white. The values of* r_1 *and* r_2 *are in nm.*

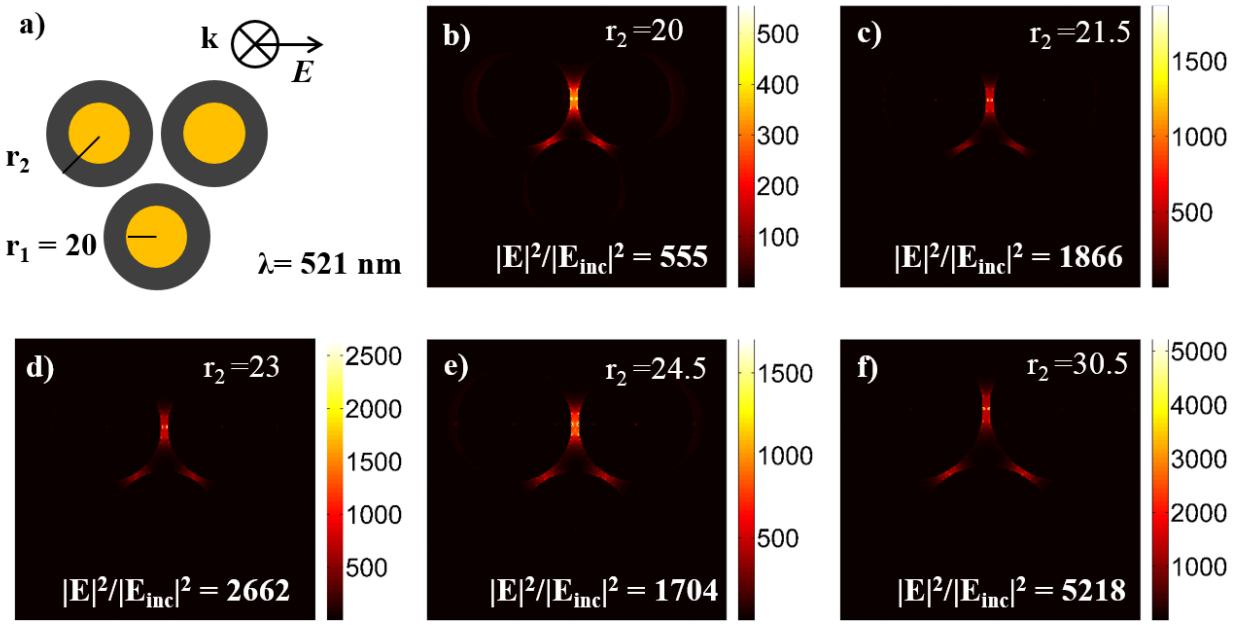

Figure 23 a) Schematic draw of the trimer and the polarization direction of the field. Map of near-field intensity$|\boldsymbol{E}|^2/|\boldsymbol{E_{inc}}|^2$ *at 435 nm incident wavelength of b) 40Au NP c) 40Au@*$Ag_{0.4}$*, d) 40Au@*$Ag_{0.7}$*, e) 40Au@*Ag_1*, and f) 40Au@*Ag_3 *NPs. In each figure the value of the maximum field enhancement is reported in white. The values of* r_1 *and* r_2 *are in nm.*

4. Application of 2D arrays as SERS substrate

4.1 Introduction

Nowadays, the need for early-stage diagnosis, and detection of trace contaminants has triggered the surge of interest in single-molecule detection techniques.[107] In order to achieve single-molecule detection (SMD), cross-section of the order of $\sigma \sim 10^{-16}\ cm^2$ are needed, and these values are only achievable for fluorescence cross-sections of strong emitters (fluorophores). Apart from fluorescence spectroscopy, another candidate for SMD is surface-enhanced Raman scattering (SERS).[76] SERS has been recognized as one of the most promising techniques since it does not rely on the use of markers as in fluorescence. This fact is related to the high near-field enhancement induced by the metallic nanostructures, which can make up even for the small Raman cross-sections of bio-samples (typical Raman cross-section are in the range $\sigma \sim 10^{-26} \div 10^{-30}\ cm^2$). In addition, SERS, unlike fluorescence, can allow multiplexing,[108] that is simultaneous detection of various molecules, molecular recognition (from analysis of vibrational frequencies), and even detection of small structural changes in the sample under examination, which is of tremendous interest for medical applications.

In details, the mechanism of SERS can be summarized as in Fig. 24: SERS takes advantage of the near-field induced by metallic nanostructures when excited at resonant conditions to enhance both incident light ($I(\nu_L)$ excitation intensity, ν_L laser frequency) and the weak Raman signal ($P(\nu_S)$ Raman scattered signal, ν_S Raman scattered frequency). The Raman signal is produced by molecules adsorbed on the metallic substrate, whose number *N'* can be in principle smaller than the total number of molecules in the whole scattering volume, *N*. The Raman cross-section of the adsorbed molecules, σ_{ads}^{R}, can also be larger than the normal Raman cross-section of free molecules, due interactions between the molecule and the metallic nanostructure (this mechanism accounts for the so-called chemical enhancement).[77] Neglecting the chemical enhancement, the (electromagnetic) enhancement of the SERS signal (P_{SERS}) can be expressed as $EF = |A(\nu_L)|^2 |A(\nu_S)|^2$. The first contribution $|A(\nu_L)|^2$originates from the enhancement at the laser excitation frequency, where $A(\nu_L) = E(\nu_L)/E_0(\nu_L)$, and the second one $|A(\nu_S)|^2$ from the enhancement at the Raman scattered frequency, where $A(\nu_S) = E(\nu_S)/E_0(\nu_S)$. As a result, enhancement up to 14 orders of magnitude can be achieved, allowing SMD (7-8 orders of magnitude are sufficient for SMD in case of resonant Raman scattering).

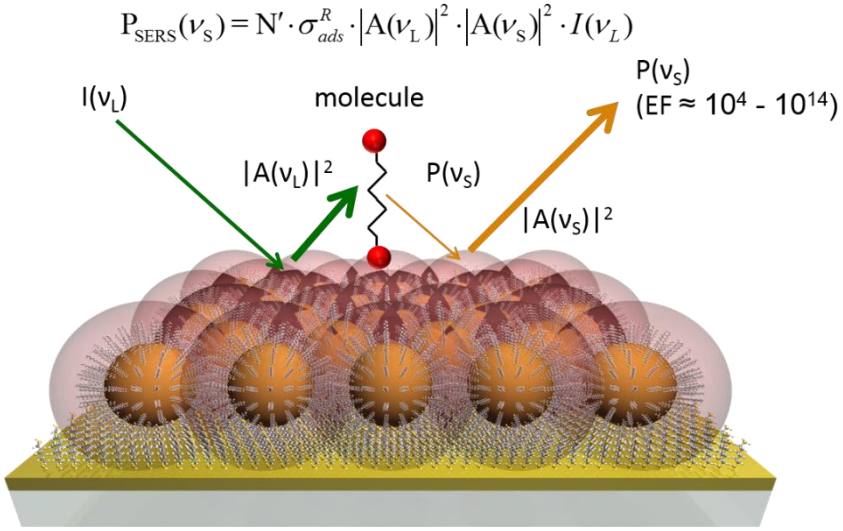

Figure 24 Schematic representation of the SERS mechanism. Incident light enhanced by metallic nanostructures impinges on the molecules and triggers emission of weak Raman scattered light that is further enhanced by interaction with the metallic substrate.

For its many promising features, SERS has been actively investigated to develop high sensitivity sensors for applications in many fields such as biology, medicine,[109] chemistry, pharmacology and environmental science.[110] The purpose of this study is to prepare reproducible, versatile, and low cost sensors in large scale that take advantage of the SERS effect.

Up to now, research on SERS substrates focused on two different approaches, the first relies on top-down techniques, such as lithography, and allows good control of optical properties of the device but has huge limits concerning the scalability of the substrate, which is usually limited a sub millimeters in size; the second relies on bottom-up techniques and usually cannot guarantee high enhancement factor (due to low density of metallic nanostructures) and good reproducibility. In this latter case the most common SERS substrates consist of colloidal solution of metallic nanoparticles, or metallic nanoparticles immobilized on a substrate by self-assembly, Langmuir-Blodgett, or layer-by-layer (among others). These methods cannot usually guarantee a controlled aggregation of particles (geometry of the aggregates and interparticle distances are randomly distributed), therefore no prior determination of the enhancement factor can be done, limiting their application for medical or industrial purposes, where reproducibility is a key issue. In order to overcome the main limitations of the common techniques, the development of a SERS substrate which shows both good control of optical properties and good reproducibility was targeted in this work.

4.2 Design of the SERS substrate

For the optimal design of our plasmonic SERS substrate, a few important factors are to be considered, that are material, LSPR matching, substrate coverage and homogeneity.

To optimize SERS conditions, it is necessary to choose the metallic nanoparticles that match our experimental conditions. In the visible range only a few materials can support plasmon resonances, notably silver and gold. AuNPs, are chemically stable and their size and shape are easy to control, but they show lower SERS activity due to plasmon damping induced by gold interband transition. In contrast, AgNPs give high SERS enhancement but they are difficult to treat because of their fast oxidation in ambient conditions. In order to combine the good complementary property of both particles and overcome the demerits of both AuNPs and

AgNPs, core-shell Au@Ag NPs were investigated. In fact, Au@AgNPs are easy to produce in a wide range of sizes and shapes, as for AuNPs, and they provide higher near-field enhancement due to the presence of silver. In addition it was recently reported that a charge transfer complex between Au and Ag can partially protect Ag shell from oxidation.

For what concerns the substrate coverage and homogeneity, a hybrid deposition method developed by our group was used. This method enables the deposition of metallic nanoparticles onto a conductive substrate, overcoming the usual limitations of top-down techniques.

Finally, LSPR tuning is a critical point to get high enhancement. It was proven that the highest enhancement can be obtained when LSPR of SERS substrate lies between excitation and emission wavelengths. In order to meet this requirement the LSPR of our 2D array can be tailored by changing shape, composition of metal NPs and their aggregation properties (interparticle distance).

4.3 SERS measurements

Various 2D arrays of MNPs were prepared as follows: at first 20 and 40 nm AuNPs were synthetized as reported in Chapter 3.1.3 These particles were also used as gold core for the growth of core-shell Au@Ag NPs with various Ag:Au molar ratios.

After characterization of the prepared MNPs, they were deposited on a conductive substrate with our hybrid method and then characterized them by means of SEM, TEM, and UV-Vis spectroscopy.

As a reference sample, a sparse sub-monolayer of MNPs was obtained from a method analogous to ref. [23] In details, a piranha-cleaned quartz substrate was immersed in a 1% solution of 3-Aminopropyltriethoxysilane (APTES) in anhydrous toluene for 7 hours at room temperature in nitrogen environment and then rinsed with toluene 3 times. The APTES-functionalized substrate was then immersed in a colloidal solution of metallic nanoparticles and left overnight to allow attachment of MNPs on the substrates. Due to electrostatic repulsion between charged metallic nanoparticles, the sample appears as a sparse sub-monolayer of MNPs dominated by isolated MNPs (only a few dimers or small aggregates can be noticed), as shown in Fig. 25.

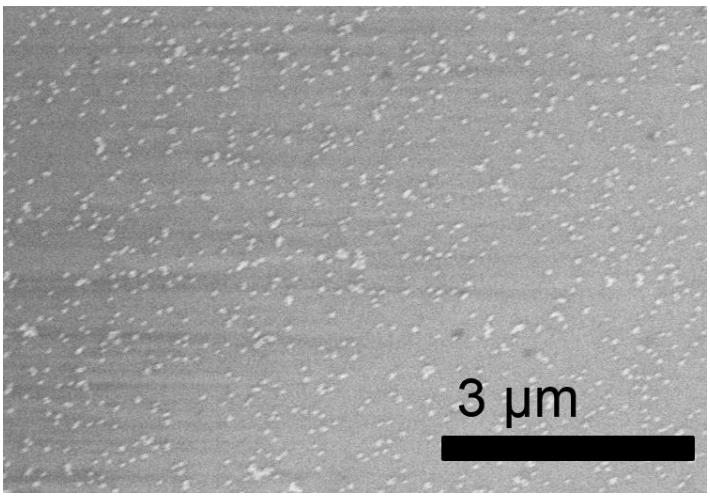

Figure 25 SEM micrograph of a sparse monolayer of 40 AuNPs on an APTES coated substrate.

Once the optical properties of all 2D arrays were confirmed, a common Raman tag,[111] Rhodamine 6G (R6G), was used to characterize the SERS activity of the various substrates prepared for this study. In order to control the amount of R6G deposited on the 2D array of MNPs, the Raman tag was vacuum-sublimated on the array to obtain a surface density of R6G of 8.2×10^{13} molecules/cm^2, corresponding to about 0.3 monolayers.[112,113]

Deposition of Rhodamine 6G (R6G) on the 2D array was performed by vacuum-sublimation of 4 mg of R6G powder. At first R6G powder was introduced in a 300 mL round bottom flask, while the 2D array was attached to the neck of the flask (12 cm distance from the bottom of the flask). The flask was then evacuated (Oil pump connected to a cold trap) and heated to a temperature of 170 °C (with a furnace). Evaporation of the dye was continued for 12 min to achieve the desired concentration.

The concentration of R6G was then evaluated by fluorescence spectroscopy. Preliminarily, a calibration curve of fluorescence intensity *vs* concentration of R6G was obtained, then, from the parameters obtained from the linear regression, it was possible to evaluate the concentration of our vacuum-sublimated samples. As reference sample a silanized (Trimethoxyoctyl silane functionalized) quartz substrates was chosen in order to minimize the attachment of the dye to surface and guarantee an optimal removal of the dye. A few reference samples were coated with R6G (same procedure as for the 2D array) maintaining the same experimental conditions in order to test the reproducibility of this deposition method. Then, the reference samples were rinsed thoroughly with a fixed amount of methanol to dissolve the sub-monolayer of R6G. The solution obtained from this process was then checked by fluorescence spectroscopy and the total amount of R6G was calculated. Finally, surface concentration was estimated by assuming an homogeneous dye coverage of our sample surface (1×1 cm^2). For surface density estimation, an average value of molecular size obtained from literature was used (reports suggest a molecular size in the range of 25-40 Å^2, with saturation surface density of $(2.5–4) \times 10^{14}$ molecules/cm^2).

After R6G deposition, SERS signal was collected from various points on the 2D arrays and the SERS enhancement factor was calculated for each array. In order to calculate the enhancement factor, SERS substrate enhancement factor (SSEF) was used,[114] which is the spatial- and allowed-orientation-averaged single molecule enhancement factor. This definition of enhancement factor presents various advantages, at first it is rigorous, since it originates directly from the definition of the single molecule cross-section; second it takes into account the effect of the substrate coverage (by including the effect of the total metallic surface) allowing comparison of various substrates with different MNPs coverage and MNP size.

The single molecules enhancement factor (SMEF) is defined by:

$$SMEF = \frac{d\sigma_{SERS}/d\Omega}{d\sigma_{RS}/d\Omega} \tag{14}$$

where $d\sigma_{SERS}/d\Omega$ and $d\sigma_{RS}/d\Omega$, respectively, are the differential SERS and non-SERS cross-sections of the same single probe molecule in the same scattering geometry. Thus, the SSEF is defined by: SSEF = {[SMEF]}, where the average denoted by brackets is to be taken over all *allowed* orientations of the molecule in SERS condition; and the average denoted by braces means the spatial-averaging over the scattering area on the SERS substrate. For a micro-Raman experimental geometry, the SSEF can be expressed in terms of the experimentally measured signals for the SERS and non-SERS measurements. In this study, an aqueous solution of R6G (100 μM) was used as the non-SERS reference sample. The experimental geometry for the SERS and non-SERS measurements is shown in Fig. 26. For our geometry, the SSEF can be calculated following the formula reported in ref.:[114]

$$SSEF = \frac{I_{SERS}/(\mu_M \mu_S A_M)}{I_{RS}/(c_{RS} H_{eff})} \tag{15}$$

where A_M represents the (available) metallic nanostructure surface area [m^2] calculated from the diameter of MNPs evaluated from the SEM images under the assumption that probe molecules are adsorbed only on the upper half surface of MNPs, μ_M the density of MNPs on the surface [m^{-2}] evaluated from SEM micrographs, μ_S is the density of dye [m^{-2}], c_{RS} [m^{-3}] is the concentration of dye in solution for normal (non-SERS) Raman scattering experiment and H_{eff} [m] is the effective scattering height, evaluated from axial detection efficiency (intensity profile vs distance from the focal plane along z). H_{eff} was estimated from Eq. 16 to be H_{eff} =178 μm and H_{eff} =15.6 μm, for the 45× objective lens and for 90× objective (see Fig. 27), respectively.

$$H_{eff} = \int_{z=-\infty}^{z=+\infty} \frac{\eta_{\perp}(z)}{\eta_o} dz \tag{16}$$

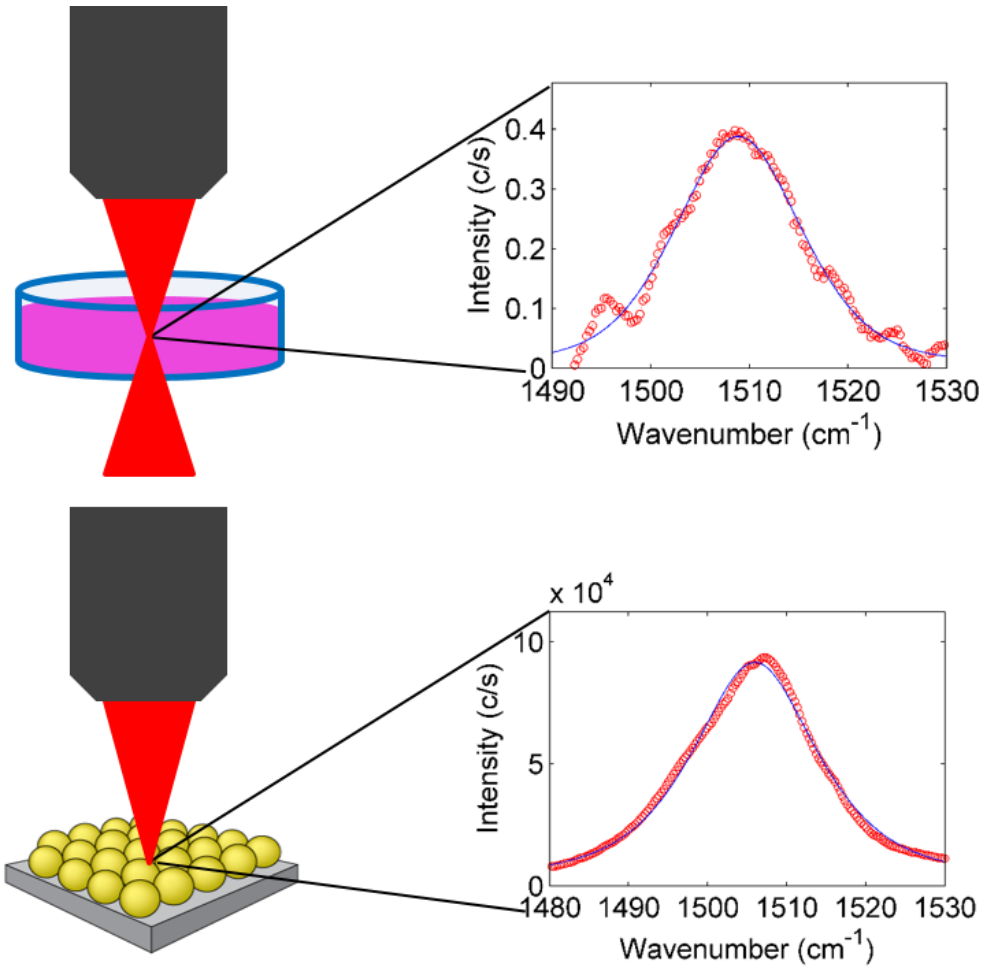

Figure 26 Schematic view of the experimental setup for non-SERS and SERS measurements of R6G, respectively in solution (top) and on a plasmonic substrate (bottom). In the graphs the best fit of the pseudo-Voigt functions is shown for both non-SERS and SERS spectra (fit of 1510 cm^{-1} peak).

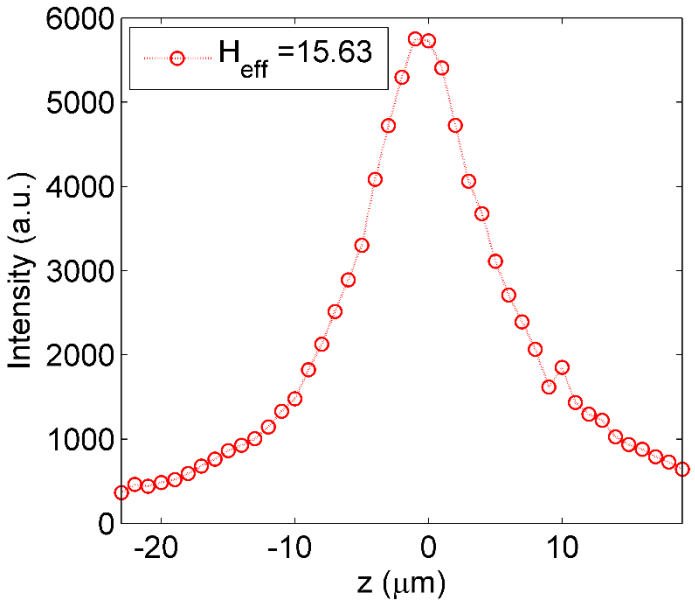

Figure 27 z-profile of intensity of the 521 cm^{-1} Si Raman peak for 90 × objective lens.

The normal Raman experiment was acquired with an aqueous solution of R6G (100 μM) and an integration time of 400 s for 45× objective lens and 800 s for 90× objective. Spectra were averaged over two acquisitions and the peaks were fitted with a pseudo-Voigt function (Eq. 17):

$$I = A \cdot \left[(1-\eta) \cdot \frac{\sqrt{4\ln(2)}}{\sqrt{\pi} \cdot \Gamma} e^{-\frac{4ln(2)\cdot(x-x_0)}{\Gamma^2}} + \eta \frac{2}{\pi} \cdot \frac{\Gamma}{4(x-x_0)^2 + \Gamma^2} \right] \quad (17)$$

In order to validate our reference spectra the cross-section of R6G (612 cm^{-1} peak) was calculated from comparison with the peak of reference compound, in our case the 516 cm^{-1} peak of 2-bromo-2-methylpropane (2BMP) was employed. The R6G cross-section obtained from our experiment $\frac{d\sigma_{RS}}{d\Omega} = 0.63 \cdot 10^{-27}$ [cm^{2}sr^{-1}] was in good agreement with data reported in literature $\frac{d\sigma_{RS}}{d\Omega} = 0.67 \cdot 10^{-27}$ [cm^{2}sr^{-1}].[114]

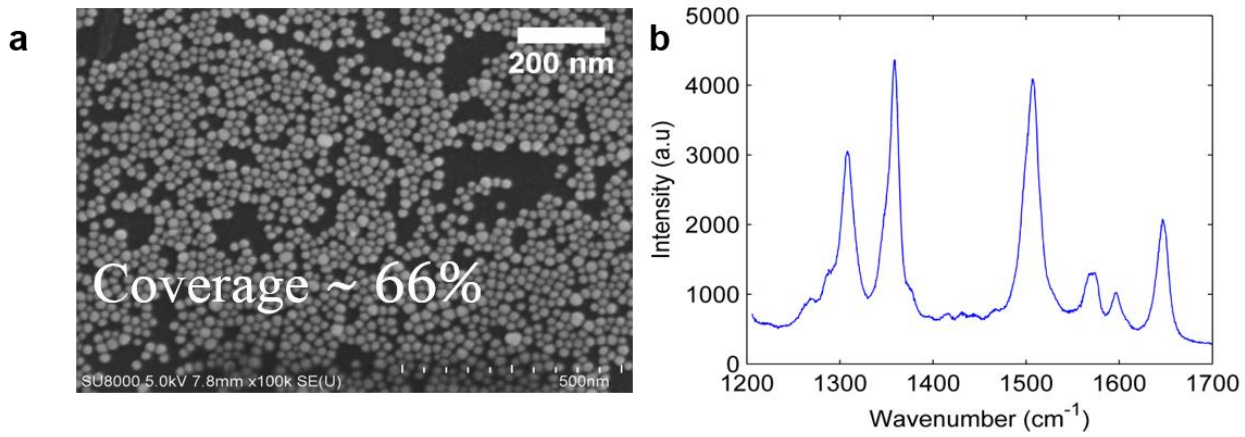

Figure 28 a) SEM micrograph of a certain area of the sample and b) SERS spectrum acquired in a corresponding region of the sample.

Afterwards, SERS spectra were measured with various substrates keeping the same experimental conditions, then the 1510 cm^{-1} peak of R6G was fitted with a pseudo-Voigt function, as shown in Fig 26, to obtain the

value of the peak area that was used to calculate the SSEF. As an example, the calculation of SSEF for 20 nm AuNP 2D array at one point was reported (the sample region under examination corresponds to the SEM image in Fig. S28a). The SERS spectrum was acquired with 45× objective lens, 4.4 mW laser power, 632.8 nm excitation, and 1 s acquisition time, and compared to the normal Raman signal of R6G 100 μM (corresponding to $6.022 \cdot 10^{22}\ molecules/m^3$), with 45× objective lens, 4.4 mW laser power, 632.8 nm excitation, and 400 s acquisition time (the intensity was normalized to the integration time to obtain the final peak area = 8.1). The enhancement factor obtained from analysis of the SERS spectrum in Fig. 28b is $SSEF = 1.2 \cdot 10^5$. Particles density was obtained by dividing the fraction of the substrate covered by MNPs (from SEM image, coverage ratio = 0.66), by the area occupied by each particle assumed perfectly circular and with radius equal to the average one (particle density is of the order of 10^3 [μm^{-2}]), while for the estimation of the metallic nanoparticle surface area the value of half of a sphere with a radius equivalent to the average radius of the particle under consideration was used. The values of sphere surface and surface occupied by a single particle appear as numerator and denominator, therefore they do not appear in the final equation.

$$SSEF = \frac{9.9 \cdot 10^4 / (0.66 \cdot 2 \cdot 0.82 \cdot 10^{18})}{8.1 / (6.022 \cdot 10^{22} \cdot 178 \cdot 10^{-6})}$$

$$\mu_m = (66/100) / (\pi \cdot r^2)$$

$$A_m = 2 \cdot \pi \cdot r^2$$

$$\mu_s = 0.82 \cdot 10^{18} molecules / m^2$$

4.4 Discrete-dipole simulations

DDA simulations performed as described in Chapter 3.2.4 were used to calculate the extinction spectra and compute the enhancement factor of aggregates (trimers) of MNPs. The definition of enhancement factor used for these calculations derives directly from the definition of the electromagnetic enhancement:

$$EF = \left(\frac{|E(\omega_o)|^2}{|E_o(\omega_o)|^2}\right)\left(\frac{\left|\widehat{\boldsymbol{E}} \cdot \widehat{\boldsymbol{\mu}}\right|^2}{\left|\widehat{\boldsymbol{E_o}} \cdot \widehat{\boldsymbol{\mu}}\right|^2}\right)\left(\frac{\rho_{EM}(\omega_o - \Delta\omega)}{\rho^o_{EM}(\omega_o - \Delta\omega)}\right) \tag{18}$$

where $E_o(\omega_o)$ is the magnitude of the incident field at the fundamental frequency, $E(\omega_o)$ is the magnitude of the field at the molecule (emitter), $\widehat{\boldsymbol{E}}$ is the polarization direction of the field at the location of the emitter, $\widehat{\boldsymbol{E_o}}$ is the polarization of the incident field, $\widehat{\boldsymbol{\mu}}$ is the orientation direction of the molecular dipole, $\rho_{EM}(\omega_o - \Delta\omega)$is the electromagnetic density of states at the Stokes frequency in the presence of metallic nanoparticles, $\rho^o_{EM}(\omega_o - \Delta\omega)$ is the density of states in absence of the metallic nanoparticle.[44]

Neglecting polarization effects and assuming that the increase of the electromagnetic density of states corresponds to the increase of the local field, electromagnetic enhancement factor can be expresses as:

$$EF \approx \left|\frac{E(\omega_o)}{E_o(\omega_o)}\right|^2 \left|\frac{E(\omega_o - \Delta\omega)}{E_o(\omega_o - \Delta\omega)}\right|^2 \tag{19}$$

In our simulations, in addition, incident field at various wavelengths is held constant, therefore the expression can be written as:

$$EF \approx \left|\frac{E(\omega_o)}{E_o}\right|^2 \left|\frac{E(\omega_o - \Delta\omega)}{E_o}\right|^2 \quad (20)$$

In case of broad plasmonic resonances, for which the linewidth is much larger than $\Delta\omega$ a further approximation can be introduced, the so-called fourth power approximation:

$$EF \approx \left|\frac{E(\omega_o)}{E_o}\right|^4 \quad (21)$$

In case of 20 Au@Ag NPs, the enhancement factor was computed taking into account the wavelength of the excitation laser relative to the peak wavelength in the extinction spectra (Fig. 20a). The wavelength (632.8 nm) of the laser line used for the SERS experiment is slightly longer (30 nm) compared to the main LSPR wavelength of 20 nm AuNPs array and the 1510 cm^{-1} band of Rhodamine 6G line corresponding to a wavelength of 699.7 nm is further redshifted from the LSPR, therefore near-field simulations were performed with an excitation wavelength located near to the peak position in DDA simulated extinction spectrum of 20 nm AuNP as laser excitation and a wavelength corresponding to the relative Raman shift as Raman scattered light for computing the enhancement factor.

By choosing such formulation the enhancement of the field intensity is calculated at both excitation wavelength (laser excitation) and molecular vibration wavelength (Raman scattered light). Practically, the enhancement factor was evaluated by multiplying the maximum near-field intensity enhancement obtained from DDA simulations at two different wavelengths (Eq. 20), chosen according to experimental conditions and simulated extinction spectra.

In case of 40Au@AgNPs, due to the broad LSPR peaks of the 2D arrays the (overall) maximum enhancement of each array was evaluated (in the wavelength range between 300–700 nm) and the simplified relationship in Eq. 21 was used.

4.5 Comparison of SERS and simulations results

The SERS spectra of R6G deposited on 20AuNPs and 20Au@Ag NPs 2D arrays of are reported in Fig. 29a (only one spectrum for each plasmonic substrate is shown for clarity). In Fig. 29b the experimental SSEFs and their standard deviation (error bar in the plot) are shown; each experimental value in Figure 29b was obtained from the average over 6 different points in the corresponding substrate.

From Fig. 29b a peculiar tendency of the SSEF can be noticed: at first SSEF increases up to 20Au@$Ag_{0.7}$, then drops at 20Au@Ag_1, and increases slightly for 20Au@Ag_3. The maximum value of SSEF in a determined position was obtained for 20Au@$Ag_{0.7}$ 2D array and corresponds to 7.9×10^5, while the average SSEF over 6 points of the same substrate gives a SSEF of 6.4×10^5. Experimental SSEFs are found to be extremely uniform over the substrate with the largest standard deviation being 25% of the relative SSEF value.

To confirm the homogeneous response over the sample, Raman intensity maps were also acquired for a test 2D arrays substrate (Fig. 30) and compared to a sparse sub-monolayer of AuNPs obtained from self-assembly (Fig. 25 for the SEM and Fig. 31 for the Raman intensity map).[23,33] As it can be noticed from comparison of Fig. 30 and 31, our 2D array shows a uniform intensity over the whole area, while the sparse sub-monolayer

shows an inhomogeneous response with local "hot spots", corresponding probably to dimers or small aggregates, similar to the result obtained in ref.[23] in case of sparse MNPs monolayer.

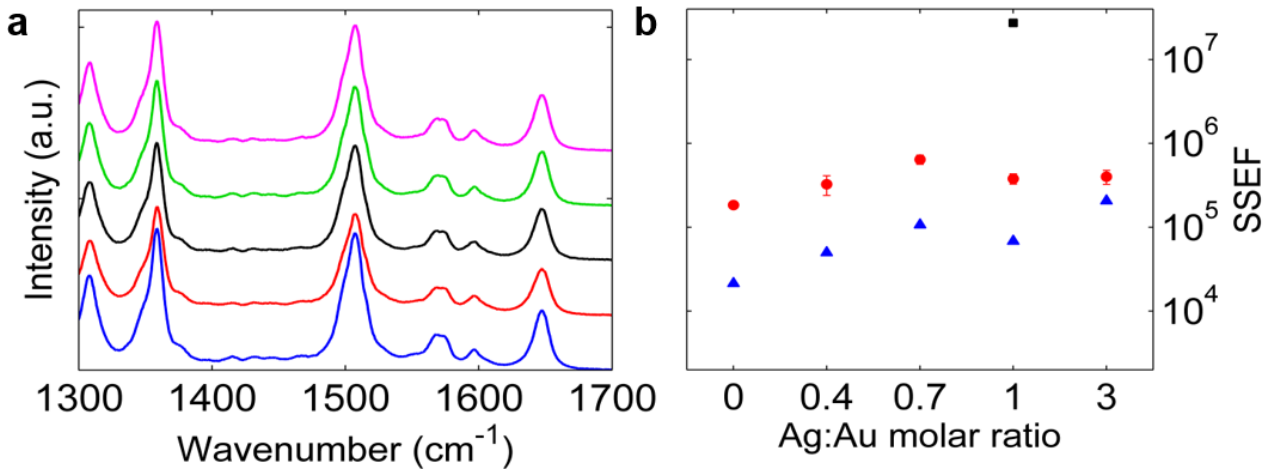

Figure 29 a) SERS spectra of R6G deposited on i) 20AuNPs, ii) 20Au@Ag$_{0.4}$ NPs, iii) 20Au@Ag$_{0.7}$ NPs, iv) 20Au@Ag$_1$ NPs, and v) 20Au@Ag$_3$ NPs 2D arrays. All SERS spectra are shifted by a constant value for clarity. b) Comparison of experimental SSEF obtained from SERS spectra of R6G on 20Au@Ag NPs arrays (circles), corresponding simulated EF for 20Au@Ag NPs trimers (triangles) and simulated EF for 20Au@Ag$_1$ heptamer (square).

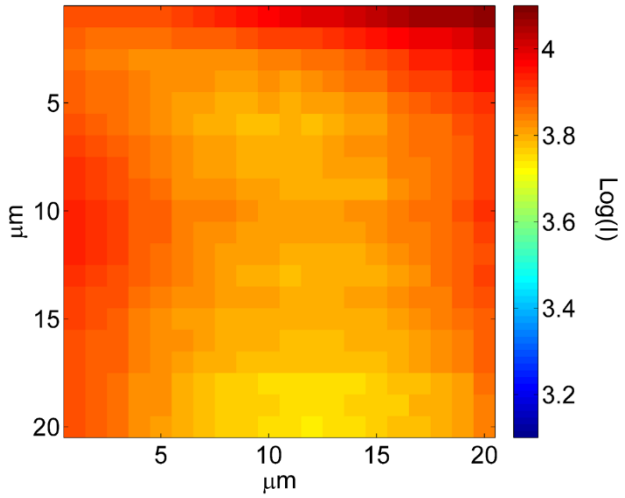

Figure 30 Raman intensity map obtained from 20Au@Ag$_{0.7}$ 2D array with 1 μm step, 45× objective, 1 s accumulation. The logarithm of the intensity of 1510 cm^{-1} peak of R6G was analysed after baseline subtraction. The standard deviation in intensity over the whole 20 × 20 μm^2 area corresponds to 15% of the maximum value of the intensity.

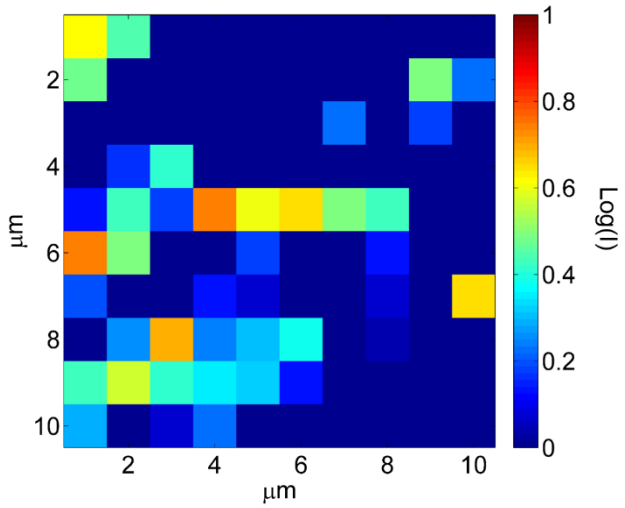

Figure 31 Raman intensity map obtained from a sparse monolayer of 40 AuNPs with 1 µm step, 45× objective, 10 s accumulation. R6G was vacuum-sublimated following the same procedure used for the 2D arrays in order to achieve the same dye density. The logarithm of the intensity of 1510 cm^{-1} peak of R6G was reported after baseline subtraction and division by total accumulation time. The standard deviation in intensity over the whole 10 × 10 μm^2 area corresponds to 93% of the maximum value of the intensity. In the map it is easy to recognize the presence of hot spots due to local high enhancement occurring probably near AuNPs dimers or small aggregates toghether with large area with no intensity coming from totally uncoated regions or regions with isolated AuNPs, as shown in Fig. S (note that the area of the map does not correspond exactly to the area shown in SEM micrograph, therefore correlation cannot be made).

This result confirms the importance of a high and homogeneous coverage of the samples to obtain controllable enhancement over the whole substrate (not dependent on localized "hot spots"), which is a key issue for the development of SERS-based sensors.

After analysis of experimental data, the experimental values of enhancement factor (SSEFs) were compared to the ones obtained from simulations (EF).[115] From Fig. 29b a very good agreement between the SSEF and the EF can be found, apart from the value of the SSEF, which is constantly underestimated by the simulation. Although the value obtained for simulation is only an approximation of the real enhancement factor, such underestimation can be understood by various factors. At first, in our calculations only the electromagnetic enhancement factor was computed, without taking into account the possible contribution of the chemical enhancement to the experimental SSEF. In addition, the model employed in simulations (see Fig. 32a) differs remarkably from the real structure in both extension and geometry. In the model in fact the structure is an isolated trimer whose interparticle distance was set to 3 nm, instead of the experimentally estimated 2.4 nm. The decrease in the interparticle distance is known to have a tremendous effect on the enhancement,[116] especially for very small gaps.[117] To determine instead the effect of the larger extension of the real 2D array, a simulation was performed in which the trimer of $20Au@Ag_1$ NPs was replaced by a corresponding heptamer (close-packed structure with hexagonal lattice) of $20Au@Ag_1$ NPs excited at the same wavelengths. As it can be noticed from Fig. 29b, the enhancement factor predicted for this heptamer is two orders of magnitude higher than the experimental SSEF, therefore suggesting that the possible origin of the high enhancement value for experimental data is related to the highly ordered structure of the array that is not modelled perfectly by an isolated trimer.

From Fig. 29b, it can also be noticed that the tendency of the SSEF cannot be explained trivially as a function of the silver content or the LSPR matching: SSEF is neither proportional to the Ag content in the particles, nor proportional to the distance between the LSPR and the excitation wavelength. Since the far-field response alone was not enough to clarify the origin of this tendency, the simulated near-field spectra of Au@Ag NPs trimers were analysed. The study of the near-field spectra of our 2D arrays was justified by previous reports concerning metallic nanoparticle clusters, namely dimers and

chains of AuNPs and AgNPs,[34,115,118,119] where it was proven that the position of the highest the near-field enhancement does not correspond to the highest peak of the extinction spectra.

Near-field spectra were obtained by plotting the maximum value of the near-field intensity enhancement ($Max(|\mathbf{E}|^2/|\mathbf{E_o}|^2)$ where $\mathbf{E}_o$ is the incident field) outside the nanostructures (0.25 nm far from the surface) for various excitation wavelengths (from 300 to 600 nm, increment of 10 nm, except near LSPR where sampling was increased). At first, taking into account the comparison of experimental and simulated extinction spectra, it can be easily deduced that the excitation light (633 nm laser) is resonant with the long wavelength mode in experimental extinction spectra, that corresponds to the 500–550 nm mode in the simulated spectra. From comparison of far-field spectra and near-field spectra in Fig. 32 (20 nm series), the long wavelength mode is found to be redshifted of about 20 nm in the near-field spectra compared to the same mode in extinction spectra.[120–122] In addition, the intensity ratio of the near-field peaks does not follow the tendency of the corresponding far-field peaks, and additional peaks appear, that can be attributed to dark (subradiant) modes.[123]

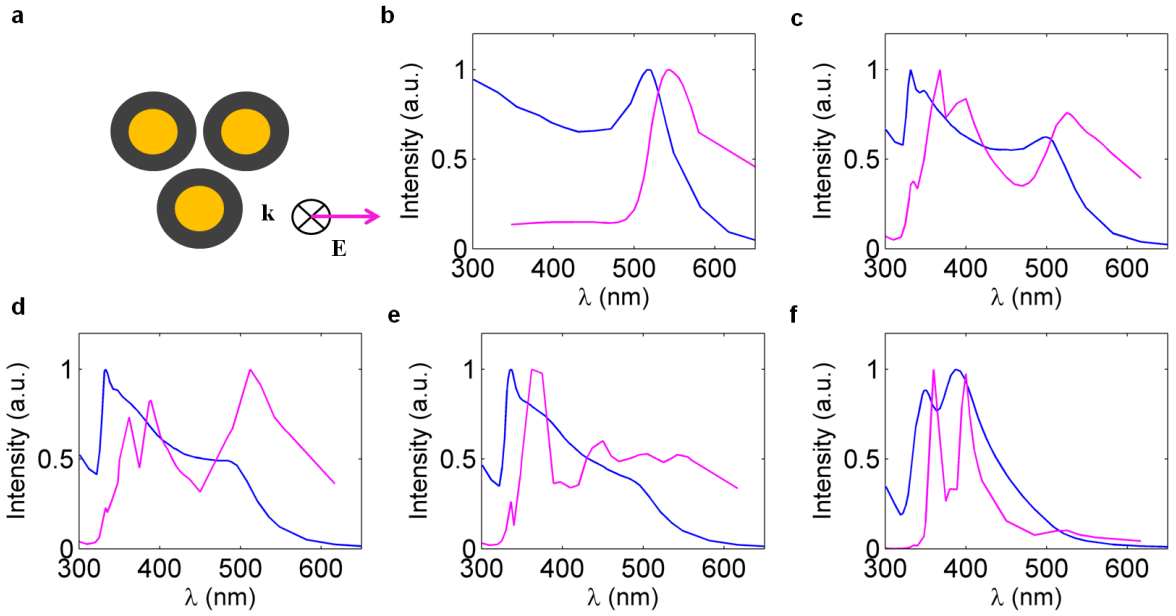

Figure 32 a) Schematic draw of the trimer and the polarization and propagation direction of the field. Comparison of near-field spectra (magenta line) and extinction spectra (blue line) of b) 20Au NP c) 20Au@Ag0.4, d) 20Au@Ag0.7, e) 20Au@Ag1, and f) 20Au@Ag3 NPs trimers. The trimers are excited along the polarization direction reported in a).

From near-field spectra in Fig. 33a, the two smallest core-shell NPs trimers (20Au@$Ag_{0.4}$ and 20Au@$Ag_{0.7}$) can induce the highest enhancement for an excitation wavelength of around 520 nm, in agreement with the most intense peak in the far-field spectra. In case of 20Au@Ag_1 trimer instead, all peaks in the near-field spectrum show comparable intensities and the highest enhancement is lower in intensity if compared to the 20Au@$Ag_{0.7}$ trimer. This phenomenon can be explained heuristically by the transition from a "core-like" behaviour that is dominant only for very thin silver shells, where the dipoles of the gold core and the dipoles of the silver shell respond in phase to the incident electric field, to a "shell-like" behaviour, where the dipoles in the core and the ones in the shell respond out of phase. As it can be deduced from both experimental results and simulations, this transition occurs around Ag:Au molar ratio equal to one. Near the transition point the contribution of the silver shell partially screens the contribution of the gold core (subradiant mode), inducing a decrease in the net dipole of the core-shell and a consequent decrease in the near-field enhancement. Interestingly, the same inversion of the tendency (from increase to decrease in enhancement) was found also for randomly-

aggregated Au@Ag NPs in solution,[30] confirming that this behaviour is linked to the optical response of the core-shell particles and not to this particular ordered structure. For larger shells, instead, the "shell-like" behaviour becomes dominant and the net dipole of the core-shell increases again together with the near-field enhancement, as confirmed experimentally.

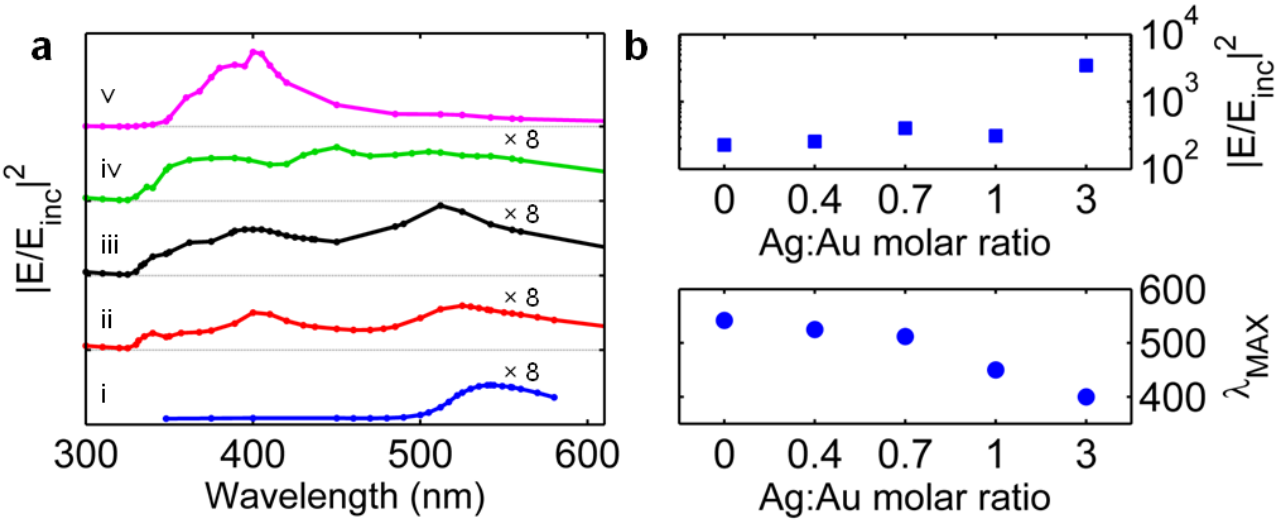

Figure 33 a) Comparison of near-field intensity enhancement spectra (averaged over two perpendicular polarizations) for the 20Au@Ag series. The spectra are normalized to the maximum enhancement of the whole series (value relative to 20Au@Ag$_3$). From the bottom: near field enhancement spectrum of trimer of i) 20AuNPs, ii) 20Au@Ag$_{0.4}$ NPs, iii) 20Au@Ag$_{0.7}$ NPs, iv) 20Au@Ag$_1$ NPs, and v) 20Au@Ag$_3$ NPs. Spectra from i) to iv) were multiplied by a factor of 8 and all spectra are shifted by a constant value for clarity. b) Top: maximum of simulated near-field intensity enhancement vs. Ag:Au ratio, bottom: dependence of wavelength position relative to maximum enhancement on Ag:Au molar ratio.

An analogous characterization was performed for the 40 nm core series (see Fig. 34). The maximum SSEF achieved for the 40Au@Ag$_3$ at one point is 7.5×10^6, comparable with reports from self-assembled films of silver nanoparticles,[23] while the average SSEF over 6 points in the same sample gives a value of 5.9×10^6, one order of magnitude bigger than for 20Au@Ag NPs arrays. This result can be related to the size effect,[124] and good matching of LSPR with excitation and emission wavelengths, since the broad LSPR peak is resonant with both laser excitation and Raman scattered light.

The effect of the silver shell can also be noticed from comparison of 2D arrays of metallic nanoparticles of similar final size and different metallic composition: 40AuNPs 2D array (average diameter = 38 nm) gives an average enhancement of 6.2×10^4, while core-shell 20Au@Ag$_3$ 2D array (average diameter = 34 nm) gives a 6.5 times higher average enhancement (4.0×10^5), showing that silver contribution to SERS enhancement is stronger than gold even for excitation in the red region of the spectrum (633 nm), where losses in silver start becoming relevant.

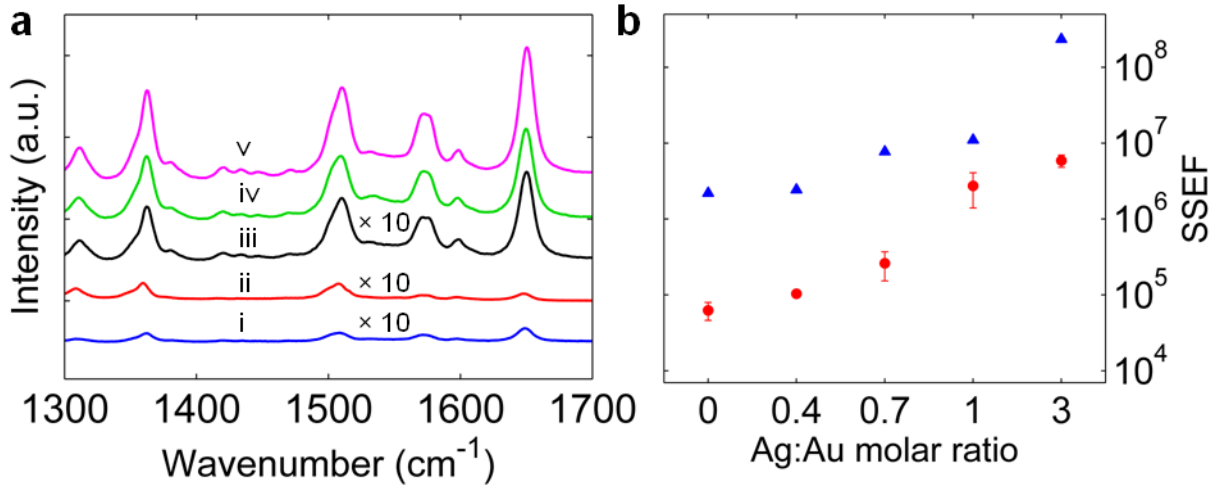

Figure 34 a) SERS spectra of R6G deposited on i) 40AuNPs, ii) 40Au@Ag$_{0.4}$ NPs, iii) 40Au@Ag$_{0.7}$ NPs, iv) 40Au@Ag$_1$ NPs, and v) 40Au@Ag$_3$ NPs 2D arrays. Spectra from i) to iii) are multiplied by a factor 10 and all SERS spectra are shifted by a constant value for clarity. b) Comparison of experimental SSEF obtained from SERS spectra of R6G on 40Au@Ag NPs arrays (circles), corresponding simulated EF for 40Au@Ag NPs trimers (triangles).

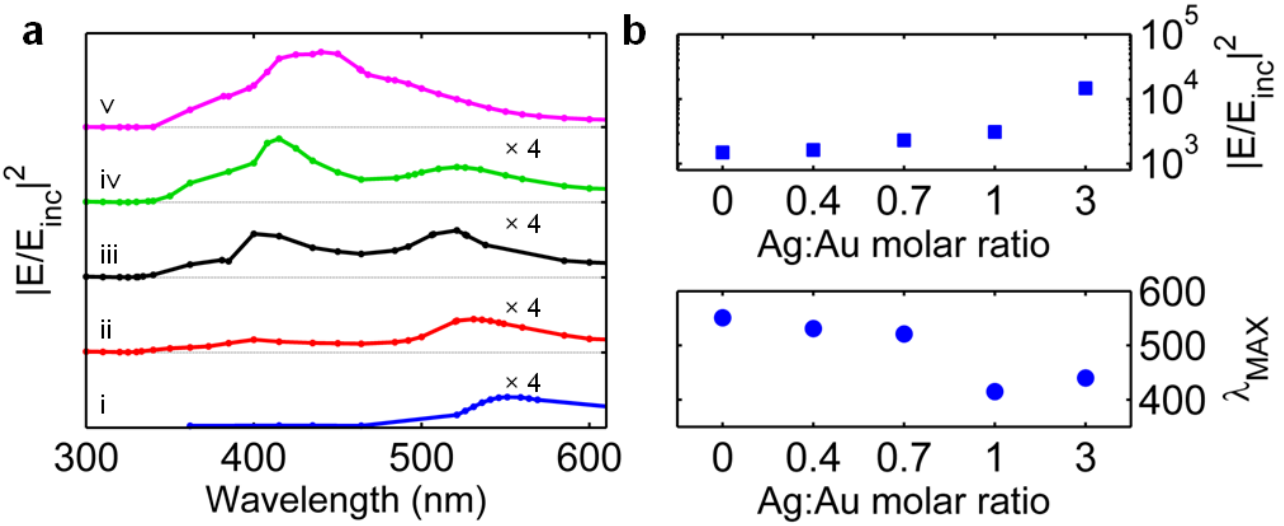

Figure 35 a) Comparison of near-field intensity enhancement spectra (averaged over two perpendicular polarizations) for the 40Au@Ag series. The spectra are normalized to the maximum enhancement of the whole series (value relative to 20Au@Ag$_3$). From the bottom: near field enhancement spectrum of trimer of i) 40AuNPs, ii) 40Au@Ag$_{0.4}$ NPs, iii) 40Au@Ag$_{0.7}$ NPs, iv) 40Au@Ag$_1$ NPs, and v) 40Au@Ag$_3$ NPs. Spectra from i) to iv) were multiplied by of a factor of 4 and all spectra are shifted by a constant value for clarity. b) Top: maximum of simulated near-field intensity enhancement vs. Ag:Au ratio, bottom: dependence of wavelength position relative to maximum enhancement on Ag:Au molar ratio.

From Fig. 34b a very good agreement between the simulated EFs obtained from near-field spectra in Fig. 35 and the experimental SSEFs for 40Au@Ag NPs was found, with the simulated values being an order of magnitude higher than the experimental ones, probably due to the poor close-packing of the 2D array of large MNPs and the consequent larger gap between MNPs (compared to the value chosen for simulations), that negatively affects enhancement.[116] In case of 40Au@Ag NPs arrays, no decrease of the enhancement factor is obtained for increasing silver content, both from experiments and numerical simulations; this phenomenon may be due to the fact that this transition between the two behaviors occurs at a ratio slightly smaller than one (see Fig. 35), due to the intrinsically different optical response of silver and gold. In addition, the average size of 40Au@Ag$_1$ NPs (Table 2) slightly exceeds the one expected from the synthetic procedure, inducing

therefore a larger enhancement than for the simulated Au@Ag NP (Table 3) with 1:1 Ag:Au molar ratio, as shown in Fig. 34b.

To summarize, different 2D arrays of Au@Ag NPs were characterized by SERS and their near-field response was found to be strongly dependent on the Au@Ag NP final size and silver to gold ratio. In addition SERS enhancement was found to be affected by the position (compared to excitation wavelength) and intensity of the near-field modes which differ from the far-field ones, suggesting that the study and optimization of far-field spectra alone is not sufficient to design plasmonic substrates with high enhancement in the wavelength region of interest.

4.5 Conclusions

In conclusion, promising plasmonic arrays of Au@Ag NPs were obtained by means of a facile self-assembly-based bottom-up deposition method. These arrays were characterized experimentally by UV-Vis spectroscopy and SERS, and their optical response was also studied computationally, revealing their potential as efficient SERS substrate in the visible range. The highest average enhancement factor was achieved for 2D array prepared with the largest Au@Ag NPs (5.9×10^6) comparable with results from self-assembled films of silver nanoparticles. The SERS enhancement factor was also proven to be homogeneous over the substrate, showing the high potential of this self-assembled 2D array as SERS-based sensor. In addition, SERS and DDA simulations revealed that the near-field optical response of Au@Ag 2D arrays can be greatly affected by various parameters, such as particle size, Ag:Au ratio and aggregation. In case of 40Au@Ag series, in fact, an increase of the enhancement factor close to two orders of magnitude was found upon silver shell growth. In addition, it was found that the near-field response of the 2D array cannot be straightforwardly predicted from the study of its far-field response, since the latter cannot account both for the exact position (redshift) and for the intensity of the maximum enhancement.

5. 2D array as plasmonic photoreactor for TPA-induced photodimerization

5.1 Introduction

Multiphoton processes are attracting a great deal of attention due to their interesting properties such as 3D spatial resolution, and their ability to shift the excitation wavelengths from UV to Vis or NIR. Nevertheless, such photoreactions can only be achieved with high-power pulsed lasers and molecules with huge two-photon absorption cross sections (e.g., porphyrin derivatives), limiting their actual application.[35] 2D or 3D metallic nanostructures are expected to break this limitation and expand the applications of multiphoton processes to a wide range of materials and weaker irradiation sources, because metallic nanoparticles (MNPs), especially gold and silver nanoparticles, possess intriguing plasmonic properties that allow them to harvest and concentrate light at their surface.[22,125]

Multiphoton-induced photoreaction in the presence of a plasmonic substrate (near-field enhanced photoreaction) was recently reported for a limited class of materials, such as diarylethenes,[38,72] photoresist polymers,[37,126] and more recently, semiconductor photocatalysts.[127,128] The plasmonic substrate serves to make up for the low quantum efficiency of the two-photon process (third-order quantum process) by increasing the electric field in the proximity of the metallic nanostructures.[36,39] Up to now, the use of such metallic nanostructured substrates for TPA reactions suffered from some major limitations linked to the fabrication method, mainly lithography or wet chemistry process (colloidal MNPs). These limitations originate in the poor control of optical properties of the metallic nanostructures or small total area of the plasmonic substrates (typically in the range of a few μm^2 for lithography). In the case of colloidal MNPs attached to the target material for the multiphoton process, the MNP loading is usually low[127] and thus it is not possible to take advantage of the "hot spots" (regions in the gap between particles) where MNPs exhibit strong near-field enhancement.[129] In the case of plasmonic substrates prepared by top-down techniques, in addition to size and cost issues, the range of applications is limited to solid-state reactions. In order to apply plasmonic TPA reactions to a wide range of photochemical processes, scalability and generality need to be achieved. Regarding scalability, solution-phase TPA reaction with an incoherent light source was already successfully performed[39] by taking advantage of a large-area plasmonic substrate prepared by a hybrid method developed by our group.[25] For generality, a different type of photoreaction needs to be proven to verify the wide-range applicability of our plasmonic TPA excitation system. Thus, a plasmonic substrate is to be fabricated bearing a localized surface plasmon resonance (LSPR) that matches the optimal condition for TPA in the anthracene derivative to induce photodimerization in the molecule with visible light irradiation. Here, the successful fabrication of different plasmonic substrates with high gap ("hot spots") density and LSPR in a wide range of wavelengths depending on the AuNP size was demonstrated.

In this work, plasmon-induced two-photon reaction was successfully applied to the photodimerization of an anthracene derivative, i.e., anthracene carboxylic acid. The photoreaction of anthracene derivatives, which has been well investigated, gives anthraquinone in the presence of O_2,[130,131] photodimer in the absence of O_2,[40] and radical-mediated dihydroxybianthryl in the absence of O_2 under a diluted aqueous condition[41] respectively, by UV irradiation for wavelengths longer than 300 nm. Among these photoreactions, the photodimerization of anthracene is a well-known reversible photoreaction that proceeds under UV irradiation for wavelengths longer than 300 nm and can be reversed thermally or under UV irradiation for wavelengths shorter than 300 nm, and thus is frequently used as a probing reaction for asymmetric photoreactions in the field of supramolecular photochemistry.[132–134] Despite the efficient photoreaction property of anthracene derivatives, to our knowledge,

there have been no reports about TPA-induced photoreaction of anthracene, with the exception of a reverse photoconversion of anthracene photodimer to monomer with three-photon absorption.[43] Here, the first plasmonic TPA-induced photoreaction of anthracene-2-carboxylic acid (ACA) was demonstrated, which gave different photoproducts according to the reaction media (Scheme 1).

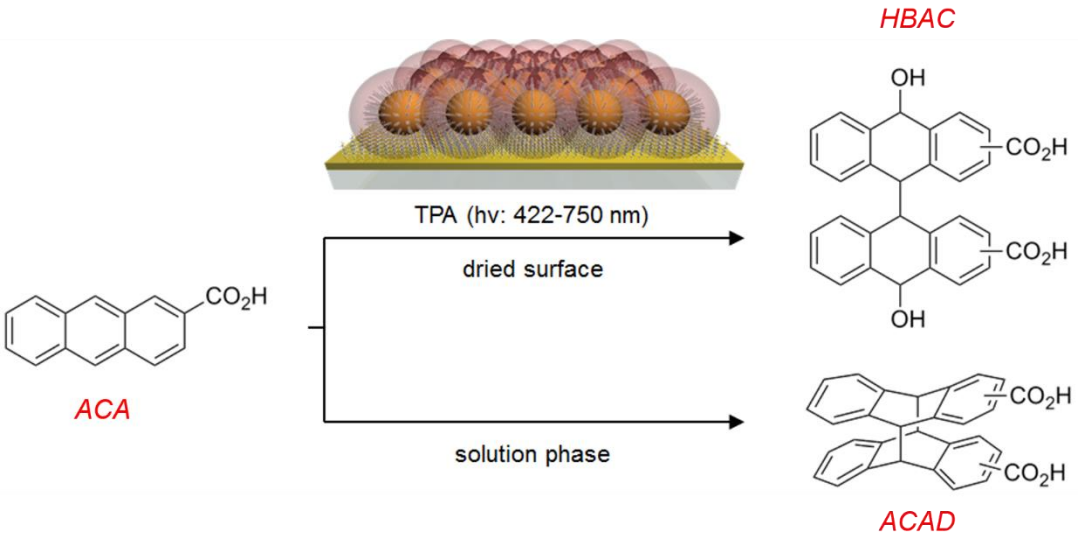

Scheme 1. Selective TPA-induced reactions of anthracene-2-carboxylic acid (ACA) both on dried surface and in solution phase with AuNP array, whose respective products were identified as anthracene-2-carboxylic acid dimer (ACAD) and 10,10'-dihydroxy-9,9',10,10'-tetrahydro-bianthryl-dicarboxylic acid (HBAC).

5.2 2D array deposition

In order to obtain a large-scale and efficient plasmonic substrate for TPA-induced photoreaction, a series of gold nanoparticle (AuNP) arrays, dodecanethiol-capped 10-nm AuNP array (10Dod array) and mixed hexanethiol-dodecanethiol-capped 23- and 39-nm AuNPs arrays (23HexDod, 39HexDod arrays), was prepared by a hybrid deposition method.[25,39] The high density and close-packed morphology of these arrays were characterized by SEM observation (Fig. 36, 37b). Optical properties of the AuNP arrays were analyzed by UV-Vis-NIR extinction spectroscopy (Fig. 37c, 38), and their LSPR was found to lie in different regions, from 605 nm of the 10Dod array, to 722 nm of the 23HexDod array, and 966 nm of the 39HexDod array, making them good candidates for visible and NIR light irradiation.

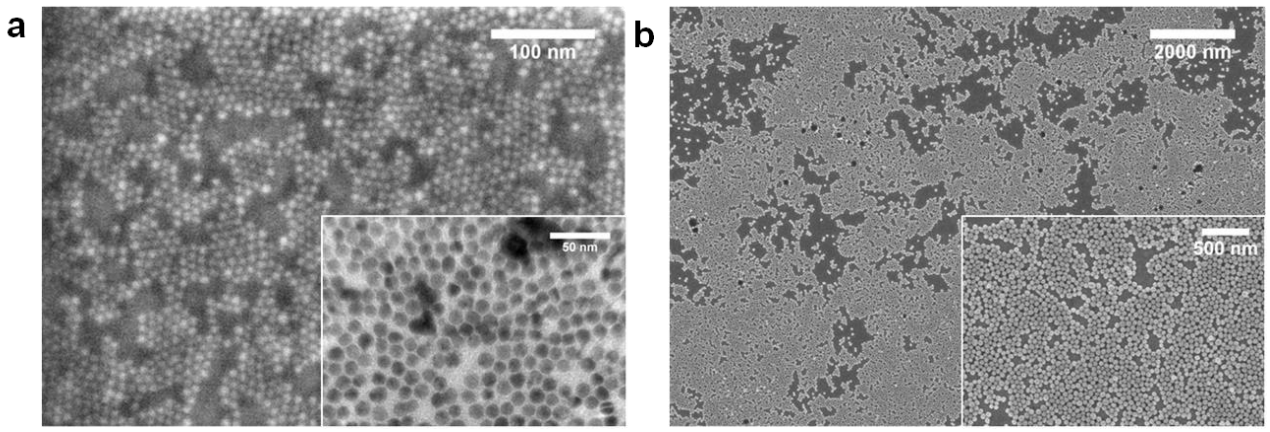

Figure 36 SEM image of a) 10Dod 2D array, and b) 50HexDod 2D array; insets show higher magnification.

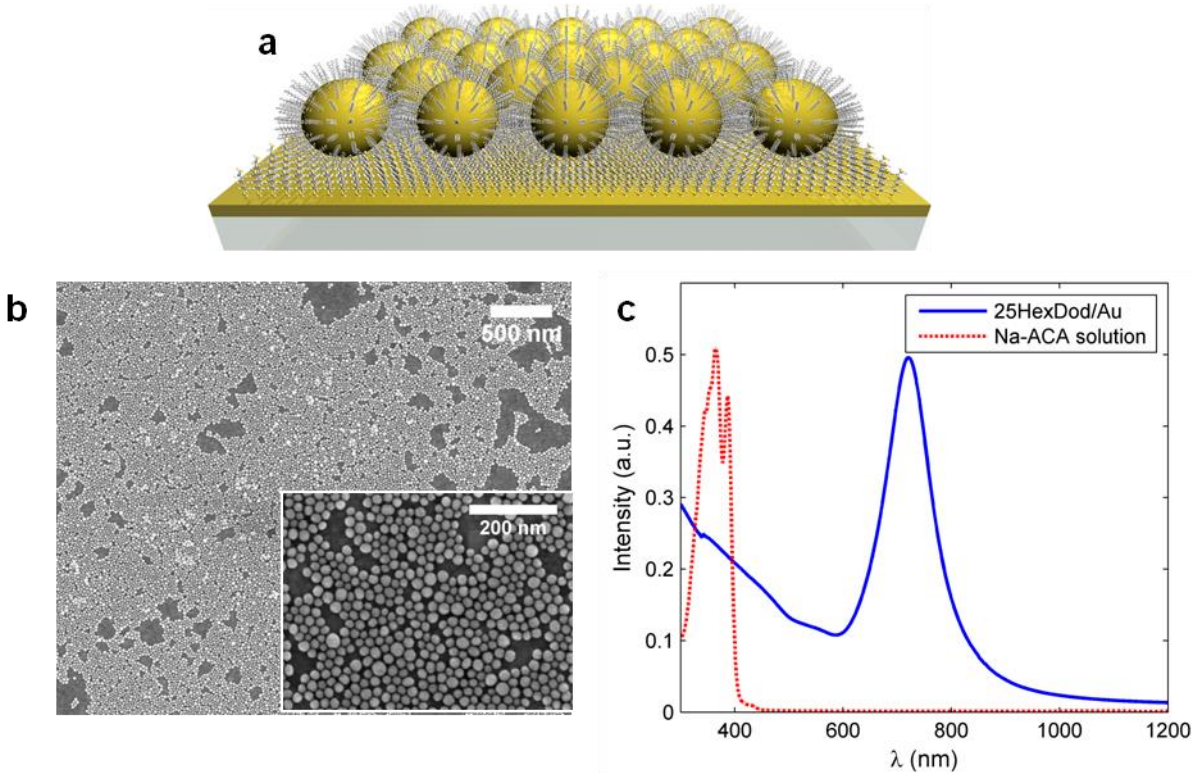

Figure 37 a) Schematic illustration of sample structure, b) SEM image; inset shows higher magnification, and c) extinction spectrum of 25HexDod array; UV spectrum of ACA is overlaid.

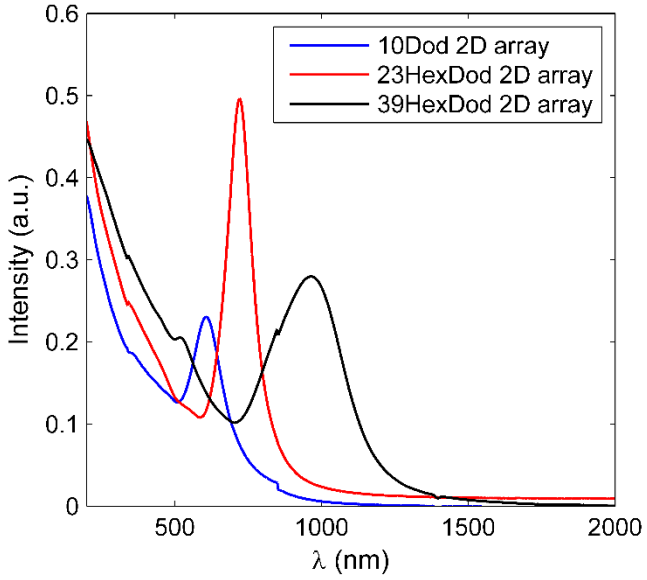

Figure 38 Extinction spectra of 10Dod (blue line), 23HexDod (red line), 39HexDod (black line) 2D array on Au substrate.

5.3 Deposition of anthracene derivative

ACA, AQCA, and ACA photodimer (ACAD) were deposited onto the AuNP 2D arrays by immersion. Deposition by immersion was performed by introducing a substrate in a sealed vessel containing a nitrogen gas-purged (15 min bubbling with N_2 gas) 5 mM anthracene derivative solution prepared by adding 1 mL of 50 mM anthracene derivative solution in DMSO to 9 mL of 6 mM aqueous NaOH solution. The samples were kept overnight in the anthracene derivative solution and then dried under a nitrogen stream. The anthracene derivative-coated samples were then characterized by Raman spectroscopy to verify the effective deposition of the molecule.

5.3.1 Synthesis of ACAD

ACAD was prepared by photodimerization under UV light irradiation (UV handheld lamp, HIROTA Co.). 15 mL of a 50.3 mM solution of ACA in DMF was irradiated with 365 nm excitation (power density 1407 μW/cm^2 at 0.5 cm distance) for 12 h in a sealed glass vessel under N_2 atmosphere. After irradiation, ACA photodimer (white precipitate) was collected with a filter paper (Kiriyama Glass Works Co.). The product was confirmed by thin-layer chromatography (hexane/ethyl acetate 1/2 v/v as mobile phase) and by ^{1}H NMR spectrum.

5.4 Raman measurements

Raman measurements were performed in order to characterize all ACA, AQCA and ACAD coated samples. Raman spectra of anthracene compounds on 23- and 39-nm AuNPs 2D arrays were acquired with an incident power of 95 μW (with a 5% ND filter), 0.42 NA objective lens (45× Super Long Working Distance Plan APO from Photon Design), integration time of 60 s and two acquisitions averaging. For detection of ACA Raman peaks with the 10-nm AuNP 2D array as substrate, the power at the sample was set to 190 μW (with a 10% ND filter), and acquisition time was set to 180 s (due to the low near-field enhancement of the substrate). The

Raman peaks relative to ACA, ACAD and AQCA were identified by comparison of the SERS spectra with DFT-calculated spectra of the same compounds, as shown in Table 4.

Table 4: Comparison of experimental (normal Raman NR and surface-enhanced Raman SERS) and DFT (B3LYP/6-31G(d)//B3LYP/6-31G(d))-calculated intense Raman lines of ACA, AQCA, ACAD and HBAC. All experimental data except NR AQCA peaks (obtained from [135]) was collected during this study.

ACA (NR - SERS on 2D array)	*ACA (DFT)*	*AQCA (NR[135] - SERS on 2D array)*	*AQCA (DFT)*	*ACAD (NR - SERS on Au)*	*ACAD (DFT)*	*HBAC (DFT)*
–	*–*	*687 – 696*	*712*	*718 – 710*	*712*	*679*
754 – 756	*776*	*–*	*–*	*–*	*–*	*733*
–	*–*	*839 – 852*	*856*	*–*	*–*	*877*
–	*–*	*–*	*–*	*–*	*944*	*958*
–	*1040*	*1037 – 1034*	*–*	*1032 – 1035*	*1040*	*1075*
–	*1168*	*1173 – 1179*	*1072*	*1177 – 1179*	*1192*	*1156*
1248(?) – 1250	*1248*	*–*	*1272*	*–*	*1264*	*1237*
–	*–*	*–*	*1352*	*–*	*1320*	*1345*
1406 – 1409	*1456*	*–*	*–*	*–*	*–*	*–*
1556 – 1560	*1536*	*1605 – 1598*	*1608*	*1610 – 1608*	*–*	*–*
1631 – 1631	*1600*	*1668 – 1667*	*1656 (1672)*	*–*	*1648*	*1660 (1696)*

5.5 Photodimerization experiment

These AuNP arrays were immersed in 5 mM ACA solution in H_2O–DMSO containing 5.4 M NaOH to adsorb ACA molecules at the AuNP surface by hydrophobic interaction with alkanethiols.[6] Irradiation of samples proceeded under continuous Ar flow in a 5-mL glass (cutoff wavelength 300 nm) vessel sealed with a natural rubber septum (Aldrich). ACA-coated AuNP array samples were irradiated from the top with UV light (285–400 nm, 300–400 nm at the sample, 59 mW/cm^2) for 24 h, Vis light (422–750 nm, 220 mW/cm^2) for 60 h, and NIR light (750–1050 nm, 294 mW/cm^2) for 48 h, respectively.

First, the plasmonic TPA-induced photoreaction of ACA was demonstrated on a dried surface (Scheme 1). Due to low ACA concentration on the surface, common spectroscopic techniques (e.g., UV-Vis) could not be used to study the photoreaction at the surface of the 2D array; therefore, Raman scattering (SERS) was used to determine the progress of the two-photon-induced reaction. SERS, in fact, takes advantage of the intrinsic ability of our array to enhance both incident (laser excitation) and scattered electromagnetic fields to monitor the photodimerization of dried ACA. The photoreaction progress was confirmed by comparing the SERS spectra of the photoreaction product with the spectra of the starting ACA, and of all possible photoreaction products such as anthraquinone-2-carboxylic acid (AQCA), and photodimer of ACA (ACAD), see Fig. 39.

The most intense peaks for these compounds were observed at 756, 1409 cm^{-1} for ACA; 710, 1035, 1179 and 1608 cm^{-1} for ACAD; 1034, 1179, 1598 and 1667 cm^{-1} for AQCA (Fig. 39a–c), respectively.

After Vis light irradiation, the SERS spectra of both the 10Dod and 39HexDod arrays still presented the typical features of ACA along with a clear contribution from AQCA (Fig. 40c, 41c). Contrastingly, the Vis-irradiated 23HexDod array showed a dramatic change in the SERS spectrum (Fig. 39e), which has some features common to both ACAD and AQCA at 1040, 1179, 1608 cm^{-1}, and almost no contribution from ACA. This result suggests that ACA is completely converted to photoproducts by TPA-induced photoreaction at the surface of the 23HexDod array.

In order to explain the lower activity of the 10Dod array, it is important to take into account the different enhancement[124] and extension of the "hot spot" volume that can be achieved with different nanoparticles sizes. The near-field enhancement at a given wavelength (532 nm) was recently proven to increase with nanoparticle size for single AuNPs up to around 60 nm diameter and then decrease for larger sizes. In case of nanoparticles aggregates with small interparticle distance, though, the effect of the coupling becomes dominant[118], therefore the aforementioned result cannot be straightforwardly generalized to our samples, where gap between AuNPs. To verify this tendency we performed DDA simulations performed with DDSCAT 7.3, as described in Chapter 3.2.4.,[58–60](for simplicity 10 nm, 20 nm, 40 nm diameter AuNPs trimers with 0.5 interdipole spacing and 3 nm interparticle distance) with air as surrounding medium. These simulations confirmed the increase on the maximum near-field enhancement, and the gradual redshift of the peak with size. The maximum intensity enhancement varies from 47 in case of 10 nm trimer, to 194 in case of 20 nm trimer, to 1681 for 40 nm trimer. For what concerns the hot spot area, the enhancement was evaluated for each pixel (cube of 0.5 nm side) over the surface of the AuNPs and we can estimate that for all trimers only about 3% of the surface shows large enhancement, accounting for about 90% of the total enhancement produced by the plasmonic structure (enhancement factor defined as in Eq. 21), in agreement with previous results.[115] This result is the consequence of the criterion chosen to determine the hot spot region, that is the total area whose intensity enhancement ($\boldsymbol{|E|^2/|E_0|^2}$) verifies the request $\mathcal{E}_{surf} > \bar{\mathcal{E}}_{surf} + 2\sigma$, where $\mathcal{E}_{surf}$ is the intensity enhancement over the surface, $\bar{\mathcal{E}}_{surf}$ is the surface average of the intensity enhancement, and σ is the standard deviation of the surface intensity enhancement. Although this result would suggest that all arrays have a similar hot spot area available for TPA-induced reactions (the small area available for small AuNPs is in fact compensated by the larger particle density over the substrate), the difference in maximum enhancement is to be considered. In fact, the area of the trimer that shows an intensity enhancement higher than a threshold value equal for all arrays (chosen to be 30) is found to be very different for different sizes: for 10 nm trimer only this area correspond to 0.2% of the surface, for 20 nm trimer about 4.5%, and for 40 nm trimer about 9%. These results are affected by the intrinsic discretization of the volume DDA simulations, since each value corresponds to the enhancement calculated in the center position of the finite cubic volume determined by the interdipole spacing (volume = $0.5 \times 0.5 \times 0.5$ nm^3). The surface values reported above, therefore, do not correspond to the enhancement at the AuNP surface, but at 0.25 nm distance from it. This apparent limitation does not affect the validity of our conclusions, to the contrary the finite distance from the surface and the discretized volume are indeed helpful to take into account of the finite volume occupied by the molecule (for anthracene a volume of about 0.34 nm^3 was reported,[136] therefore for ACA a larger volume is expected due to the additional carboxyl group) and the probability of the molecule to experience a certain enhancement. By considering the size effect only, we can infer that large AuNPs are expected to give large area with high enhancement, suitable for the development of efficient plasmonic reactors.

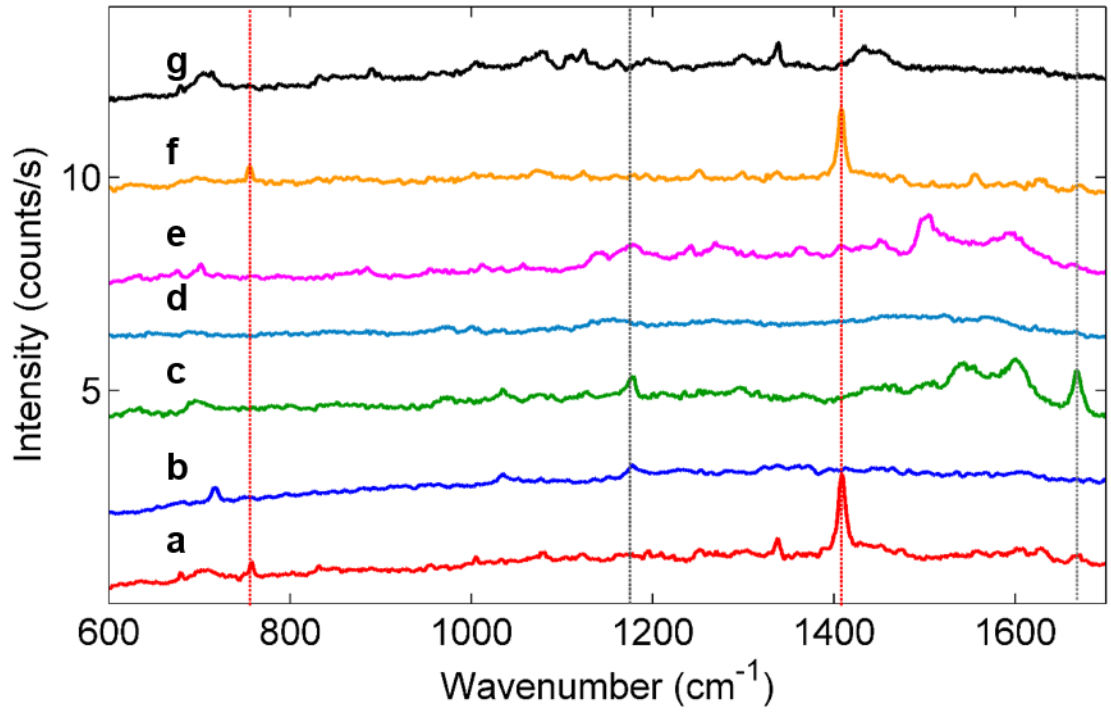

Figure 39 Raman spectra of (a) ACA on 23HexDod 2D array, (b) ACAD on Au substrate, (c) AQCA on 23HexDod 2D array, (d) UV- (e) Vis- (f) NIR-irradiated ACA-coated 23HexDod arrays, and (g) bare 23HexDod 2D array.

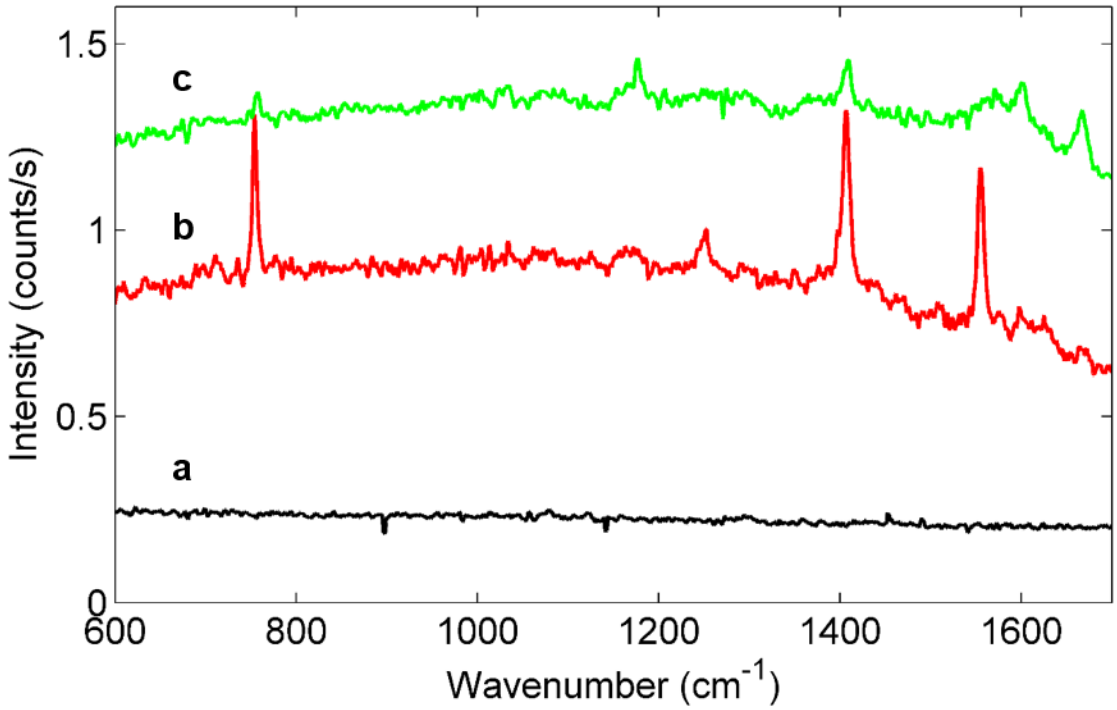

Figure 40 Raman spectra of a) bare 10Dod array on Au substrate, b) ACA/10Dod array, and c) visible light irradiated ACA/10Dod array (green line).

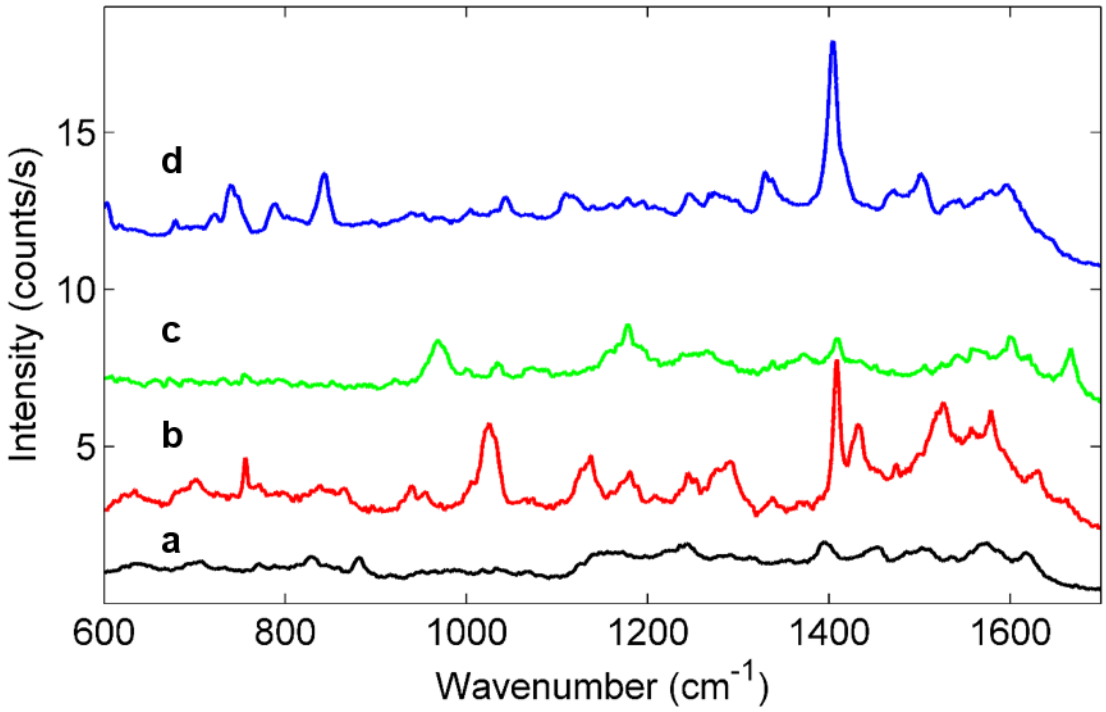

Figure 41 Raman spectra of a) bare 39HexDod array on Au substrate, b) ACA/39HexDod array, c) visible light irradiated ACA/39HexDod array, and d) NIR light irradiated ACA/39HexDod array.

A second consideration can be drawn from the photoreactions results concerning the resonant excitation of the array. The photoreactions results in fact, do not depend only on the AuNPs size, but also on the excitation conditions. As can be seen from Fig. 38, Vis light is capable of exciting LSPR in the case of the 10Dod and 23HexDod arrays, while for the 39HexDod arrays Vis light can only excite the quadrupole peak (500 nm) and the shoulder of the main LSPR peak. The performance of the 39HexDod array, which was found to be the highest when considering only the effect of the AuNP size, is instead inferior to the one of 23HexDod array. This result, in fact, is probably due to the excitation wavelengths used for photoreaction, which are far from the resonant condition of the array (LSPR is in the NIR). It is well known that the excitation of the array with light whose wavelength is resonant with the LSPR results in intensity enhancement more than 1 order of magnitude higher than for off-resonance conditions. At first, the effect of resonance matching for our arrays was studied numerically by means of DDA simulations of a 40 nm AuNPs trimer. As a result, when the trimer is excited in resonance an intensity enhancement of 1681 is obtained, while for excitation with a wavelength 100 nm shorter than the resonant wavelength, the intensity enhancement is 100, which is only 6% of the maximum value, thus explaining the lower activity of 39HexDod array.

In order to prove further the importance of the correct choice of the excitation wavelength, we performed various photoreactions experiments with different excitation wavelengths corresponding to the 2D arrays' LSPR, λ_{TPA}, λ_{OPA} (wavelength corresponding to one-photon absorption) and an off-resonant wavelength. In detail, the 23HexDod array (2D array with the best match between LSPR and λ_{TPA}) was irradiated with UV (λ_{OPA}) and NIR light (off-resonance wavelength) (Fig. 39d, f). It can be clearly seen that the ACA contribution (red dotted line in Fig. 39) is still dominant after NIR irradiation, which suggests that no reaction occurred, as expected. In the case of UV irradiation (λ_{OPA}), no clear peaks were observed, which was confirmed by SEM measurement to have arisen from the sintering of AuNPs caused by the cleavage of surface alkanethiols.[137] Next, in the case of the 39HexDod array, irradiation was also performed with light in a suitable range to excite

the LSPR in the array (NIR light). NIR irradiation on the ACA-coated 39HexDod array resulted in no detectable change from the original ACA spectrum (see Fig. 41d). This result suggested that excitation of the 2D array under resonant conditions alone ($\lambda_{ex} \equiv \lambda_{LSPR}$) is not sufficient to trigger photoreaction, and that suitable irradiation wavelengths are needed to induce any photoreaction in the dried ACA (overlapping between λ_{ex} and λ_{TPA} is small in the case of 39HexDod 2D array).

In synthesis, we can state that a tradeoff should be found between the maximization of AuNP size (up to around 60 nm diameter) and the best matching of the LSPR position, since those two parameters are intrinsically related (AuNP size affect its LSPR position) and the increase in intensity enhancement induced by one effect can result in the decrease by the second.

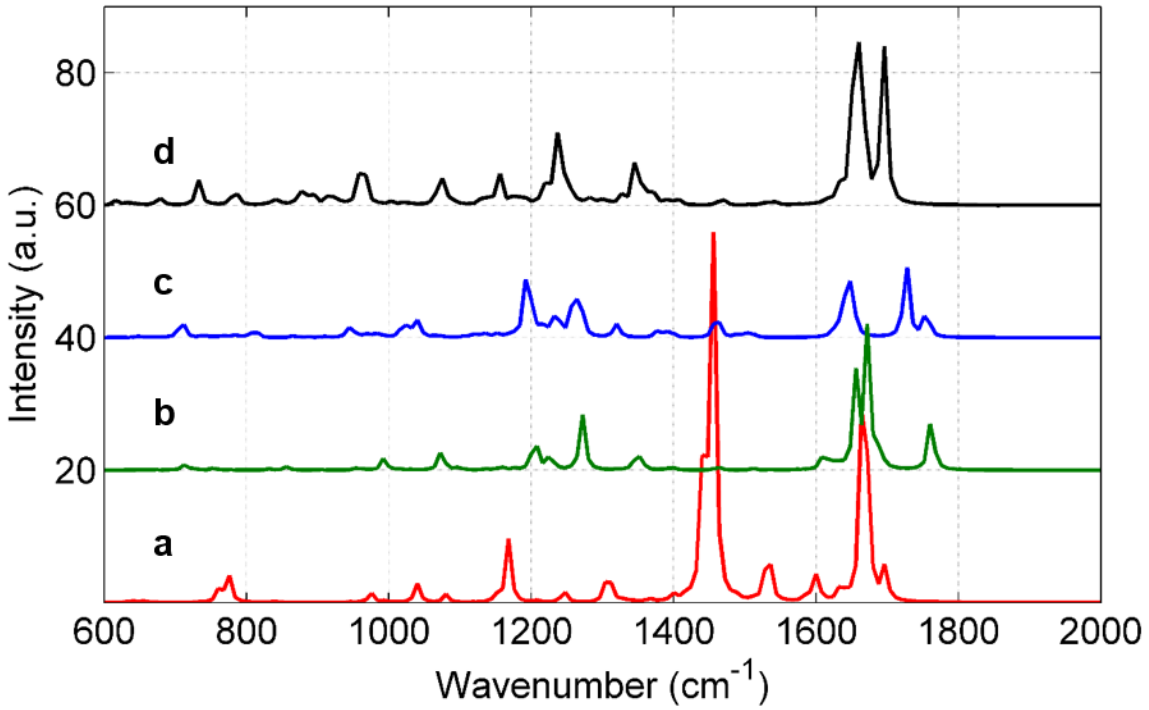

Figure 42 DFT-calculated Raman activity of a) ACA, b) AQCA, c) ACAD obtained by averaging the 4 stereomers of ACAD, and d) 10,10'-dihydroxy-9,9',10,10'-tetrahydro-bianthryl-dicarboxylic acid (HBAC).

After a first comparison between the photoreaction progresses for various plasmonic substrates was performed, it was deemed necessary to identify clearly the photoproduct of the Vis-light-irradiated ACA-coated 23HexDod 2D array to gain further insight into the photoreaction mechanism. Thus, DFT calculation of Raman spectra of all candidate products was performed, such as ACAD, AQCA, and 10,10'-dihydroxy-9,9',10,10'-tetrahydro-bianthryl-dicarboxylic acid (HBAC), see Fig. 42 and Table 4. Although DFT-calculated Raman spectra and experimental data do not match completely for all compounds under investigation (Table 4), the formation of HBAC could explain the appearance of several peaks around 870–890 cm^{-1} (877–895 in DFT), 1140 cm^{-1} (1156 in DFT), 1179 cm^{-1} (1156 in DFT), 1250 and 1320 cm^{-1} (1237 and 1345 in DFT) without any increase in intensity of the C=O peak at 1660 cm^{-1} (strong peak of AQCA). The formation mechanism of HBAC was previously suggested to have originated from photo-induced one-electron oxidation of anthracene backbone, following a reaction with water and dimerization.[41] As it was recently reported by our group,[6] the alkanethiol-capped AuNP surface can trap molecules inside the hydrophobic molecular interface where ACA and water can be concentrated. Thus, once ACA is excited by TPA, such sequential reaction is supposed to occur at the AuNP surface. Also, placing ACA near the AuNP surface is considered to accelerate the one-electron oxidation of ACA by AuNP's electron relay property.[138]

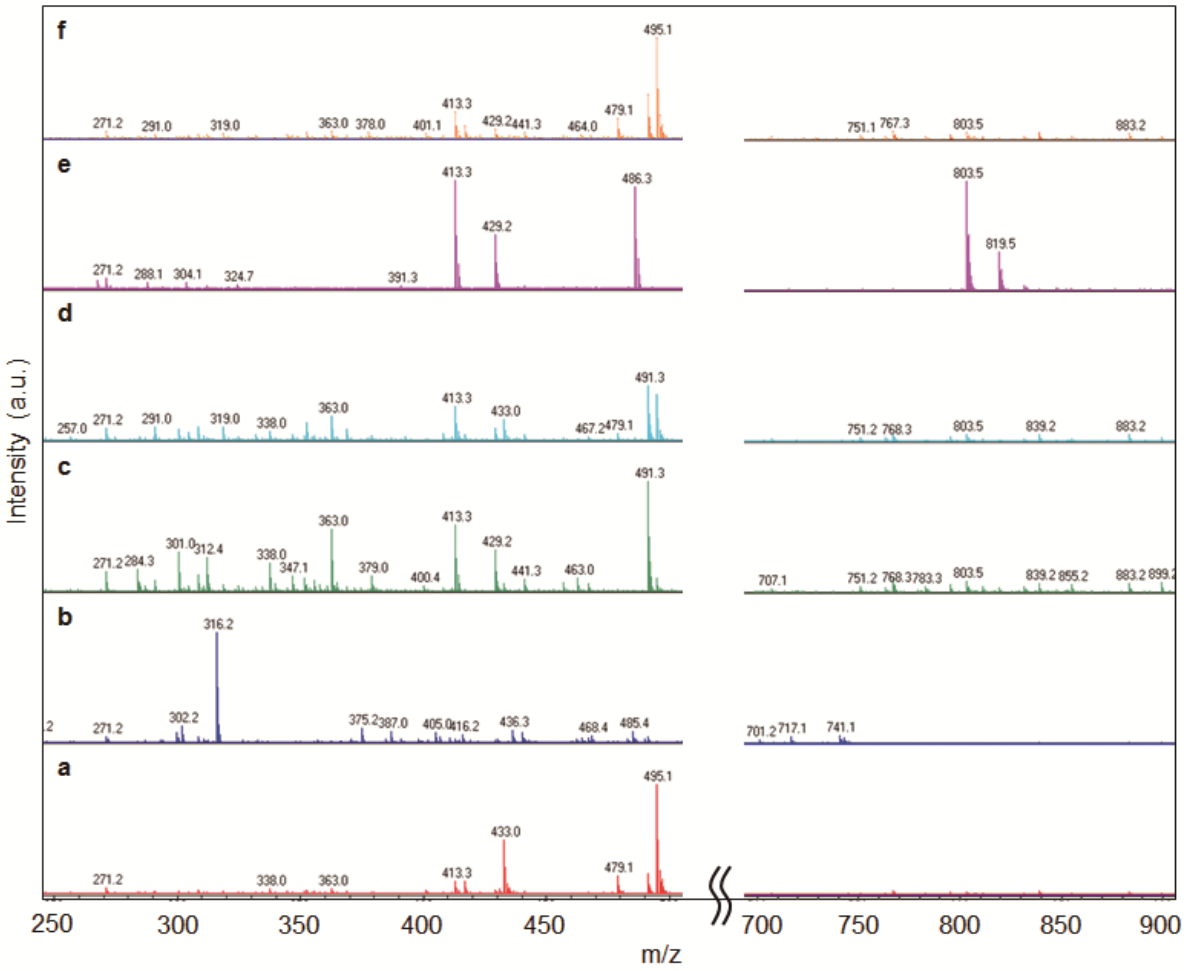

Figure 43 ESI mass spectra of (a) ACA, (b) ACAD, (c) AQCA, reaction products of (d) UV-, (e) Vis-, and (f) NIR-irradiated ACA-coated 23HexDod arrays.

In order to confirm the SERS results, all photoreaction products were analyzed by mass spectra. NIR-irradiated ACA on the 23HexDod array was confirmed to have no changes from the starting ACA (m/z 495.1 [Na-ACA + ACA − CO_2 + CH_3OH + H_2O + Na]$^+$) similar to the SERS result (Fig. 43a,f). Mass analysis revealed that some ACA content on the 23HexDod array was converted to AQCA (m/z 491.3 [AQCA − H + AQCA – CO_2 + CH_3OH]$^-$) by UV irradiation (Fig. 43c,d). Surprisingly, Vis-irradiated ACA on the 23HexDod array gave a clear mass spectrum with no remaining ACA, which confirms the formation of HBAC (m/z 803.5 [2BHAC − 2CO_2 + Na]$^+$) (Figure 43e), as suggested by DFT calculation. From these results, the 23HexDod array was found to act as plasmonic substrate for TPA-induced photoconversion of ACA.

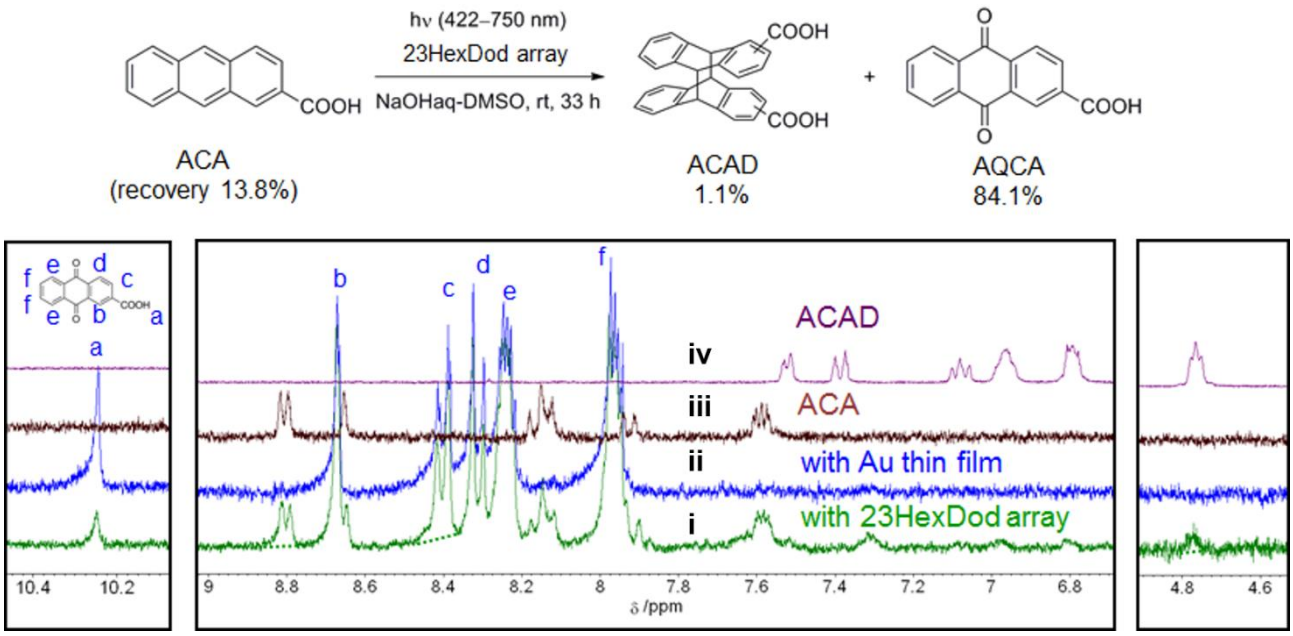

Figure 44 ^{1}H NMR (300 MHz, DMSO-d_6) spectra of Vis-irradiated ACA solution with (i) 25HexDod-array, (ii) Au thin film, (iii) ACA, and (iv) ACAD.

Second, plasmonic TPA-induced photoreaction ACA was performed in the solution phase (Scheme 1). The best substrate, the 23HexDod array, was applied to solution-phase TPA-induced reaction of ACA (Fig. 44), which is of greater interest for future applications. The substrate of the 23HexDod array was immersed in0.5 mL of 10 mM ACA solution containing 10.8 mM NaOH in H_2O–DMSO, where Vis light was irradiated for 33 h. The resultant solution was neutralized and extracted for ^{1}H NMR analysis. The ^{1}H NMR spectrum revealed the formation of trace amounts of ACAD (1.1% yield) and AQCA (84.1% yield) as a major product. This result is very interesting, since the limited yield of ACAD can be due to the small area that can generate efficient TPA-induced photodimerization. The yield can therefore provide an indirect estimation of the available hot spot area of the substrate under consideration. Summing up SEM and simulations results, we can estimate roughly the total hot spot area of the 23HexDod array to be between 1.5-2.5 % of the substrate area (average coverage of the array is 50% from SEM, hot spot area is 3-5% of the AuNPs surface), comparable with the 1.1% yield achieved for photodimerization. The slightly smaller value of the yield compared to the probability of the molecule to lay in the hot spot region can be due to the non-complete reaction of ACA in solution. The limited hot spot area of the array is also related to the formation of AQCA. In fact, the majority of ACA molecules lay on the surface of AuNPs, far from the hot spots, or on the Au substrate, and therefore will likely undergo photocatalytic oxidation with Au to give AQCA as product.[139]

A similar experiment was carried out to check the contribution of Au thin film used for the substrate of AuNP arrays, where complete conversion of ACA to AQCA was confirmed.[139] Of course, without Au substrates, the ACA solution alone did not show any spectral change by Vis irradiation because of the absence of absorption bands at this wavelength range (Fig. 37c). Considering these results, although the background single-photon-based photocatalytic oxidation reaction by Au film is dominant, conversion of ACA to ACAD was successfully achieved by TPA-induced reaction by AuNP array. Our discovery of solution-phase as well as surface-phase TPA reactions paves the way for the selection of TPA reaction depending on the reaction media.

5.6 Conclusions

In conclusion, plasmonic metallic nanostructures were proven to successfully induce TPA reaction in a molecule deposited in their proximity. A series of AuNP arrays was fabricated bearing LSPR from UV, Vis,

to NIR region depending on the AuNP size. Incoherent light in various wavelength ranges was irradiated to ACA-coated AuNP arrays and the photoreaction products were analyzed by SERS measurement and mass spectroscopy. The results confirmed that TPA-induced reaction requires matching between irradiation wavelength, LSPR, and twice the wavelength (half photon energy) of molecular excitation ($\lambda_{irr} \equiv \lambda_{LSPR} \equiv 2 \lambda_{ex}$). In addition, it was found that even when matched conditions are met, the size of the AuNPs strongly affects the progress of the TPA-induced reaction. It was suggested by both DFT-calculated Raman analysis and mass spectra that the formation of HBAC had occurred through TPA-induced reaction at the surface of the 23HexDod array by Vis irradiation, while it was demonstrated by ^{1}H NMR that solution-phase TPA-induced reaction of ACA gave ACAD. Although higher reaction efficiency is necessary to apply TPA-induced reaction for chemical synthesis, this limitation should be overcome by combining AuNP array substrates with microchannel reaction systems, making this system a promising candidate for the development of an efficient and cost-effective "lab-on-a-chip" for photoreactions.

6. 2D array as plasmonic photosensitizer for wide bandgap semiconductors

6.1 Introduction

Here, the development of a bottom-up, large-scale, cheap (no clean room facilities or high temperature are needed) and reproducible photocatalytic device is reported whose optical properties can be controlled by fine LSPR tuning via metal nonoparticle (MNP) size and interparticle distance.[25]

A hybrid deposition method was recently developed by our group, which overcomes the common limitations of both the top-down and bottom-up processes listed above; in fact, this method enables MNP two-dimensional (2D) arrays to be deposited over large substrates with high mechanical stability and high MNP coverage. Under resonant conditions (light excites LSPR in the MNPs), the 2D array generates strong NF light in the proximity of the MNPs ("hot spots"), which was shown to be able to induce two-photon absorption (TPA) in a fluorescent dye deposited on gold nanoparticles (AuNPs).[25]

The aim of this work is to demonstrate the capability of our 2D array of MNPs to induce visible light activity in an otherwise inactive material (undoped titania) and to prove the intrinsic plasmonic origin of such effect. In addition, various plasmonic-related processes are investigated to fully understand the mechanism responsible for the visible light induced photocatalytic reaction.

6.2 Synthesis of titania nanocrystals

Titania nanocrystals solution was prepared from the controlled hydrolysis of tetraisopropyl titanate according to the procedure reported in literature,[140] and the concentration was then adjusted to 10 mg/ml in ethanol–water 2:1 vol by rotary evaporation. The average size of the titania nanocrystals (3.5 nm) was determined from TEM micrographs and confirmed from XRD pattern (3 nm from the Debye-Scherrer equation) and Raman spectra[141] (below 4 nm as determined from FWHM of the E_G phonon peak) (see Fig.45). The titania nanocrystals were proven to be mainly in the anatase form, as shown in the XRD pattern (only trace of rutile) and Raman spectrum (no rutile contribution was detected from the Raman spectrum) (see Fig. 45). The bandgap of a thin film of titania nanocrystals was determined from equation:[142]

$$\alpha = B_i(h\nu - E_G)^{1/2} / h\nu \qquad (22)$$

where B_i is the absorption coefficient for a direct transition, α is absorbance and E_G is the bandgap energy of the semiconductor. From the linear fit of $(\alpha h\nu)^2$ versus $h\nu$ the value for the bandgap energy was obtained as 3.34 eV (see Figure 45b). Titania nanocrystals show a direct transition instead of an indirect transition and an energy gap larger than expected for bulk anatase titania (3.2 eV) in agreement with previously reported results[142] for nanosized titania samples.

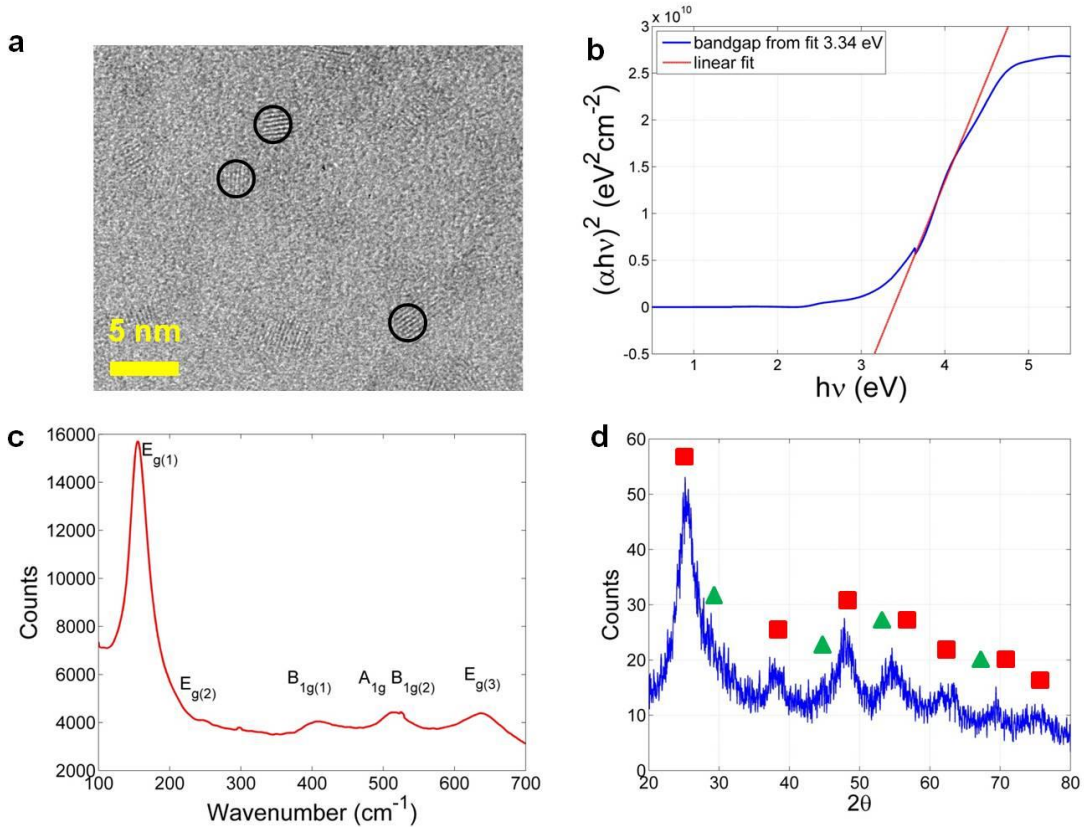

Figure 45 a) TEM micrograph of titania nanocrystals on copper grids, b) plot of $(\alpha h\nu)^2$ versus $h\nu$ for a titania nanocrystals film, c) Raman spectrum of titania nanocrystals film, each phonon peak identified belongs to anatase titania, d) XRD spectrum of titania nanocrystals powder, red square: titania anatase peaks, green triangles: titania rutile peaks.

6.3 Deposition of titania layer

The effectiveness of trimethoxyoctylsilane (TMOS) as an anchoring agent was verified by preparing two identical 2D arrays of AuNPs: one of them was coated with TMOS prior to immersion in titania solution, while the other was directly immersed in titania solution without anchoring molecules. Both samples were sonicated repeatedly to test the mechanical stability of titania. As a result, the sample without TMOS presented a clear change in the extinction spectrum with increasing sonication time while the sample protected with the TMOS layer exhibited only a minor change, as shown in Fig. 46.

The effectiveness of titania nanocrystals deposition was determined by contact angle measurements, comparing the contact angle before and after titania deposition. A change from hydrophobic to hydrophilic behavior was observed (see Fig. 47), in good agreement with the reported hydrophilicity of titania.[143]

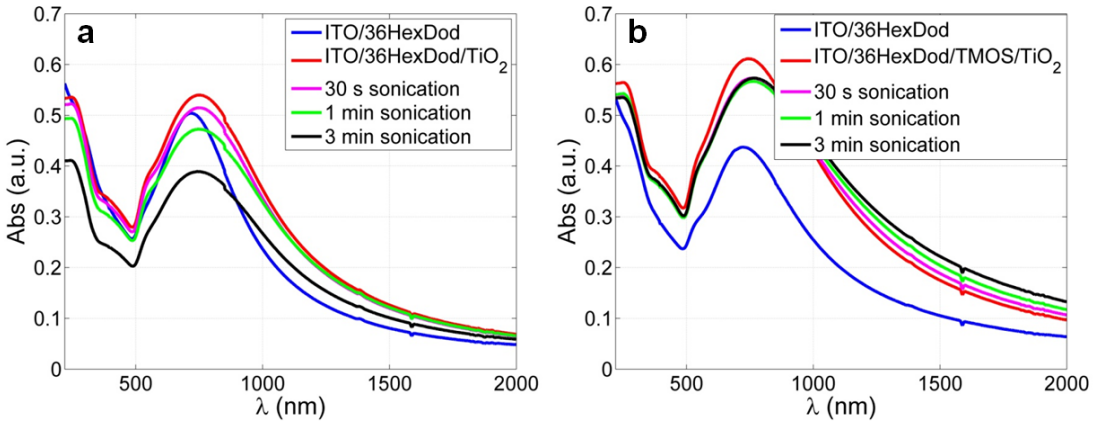

Figure 46 Extinction spectra of AuNPs 2D array without (a) and with (b) TMOS layer. Blue line: 2D array, red line: titania on 2D array, magenta line: sample after 30 s sonication in DI water, green line: sample after 1 min sonication in DI water, black line: sample after 3 min sonication.

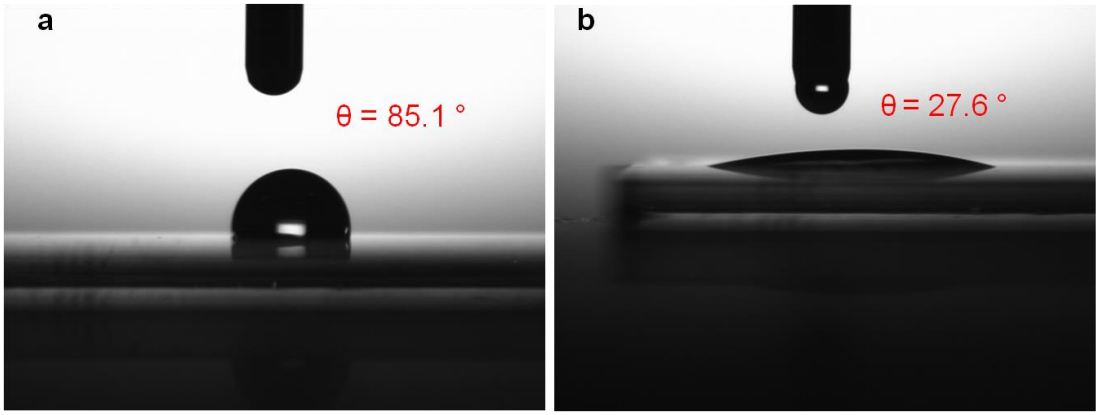

Figure 47 Contact angle before (a) titania nanocrystals deposition and after titania nanocrystals deposition (b).

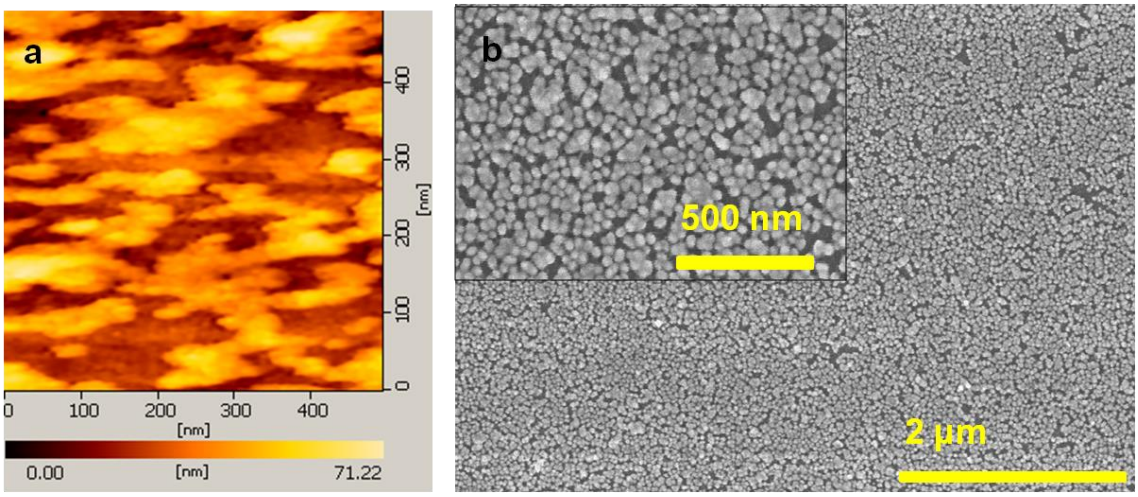

Figure 48 a) AFM image and b) SEM micrograph of 2D array of 36 nm AuNPs coated with titania nanocrystals, inset: higher magnification.

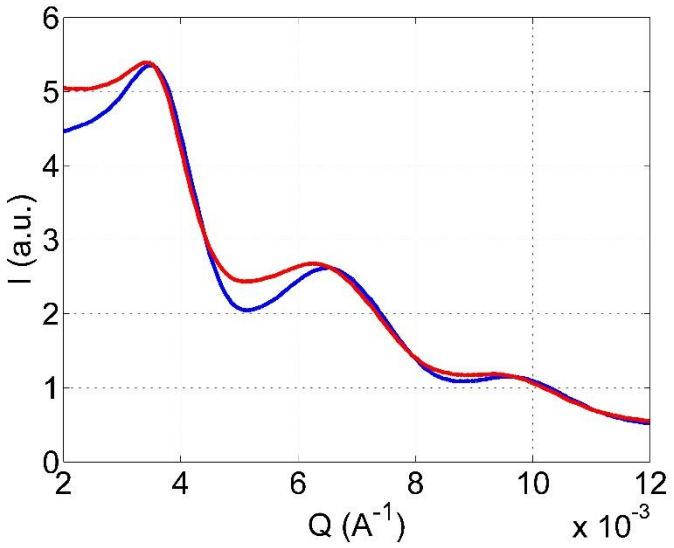

Figure 49 SAXS patterns of 2D array of 30 nm AuNPs before (blue line) and after (red line) functionalization with TMOS and deposition of titania nanocrystals.

After titania deposition, the sample was also characterized with SEM and AFM (see Fig. 48), as well as SAXS (performed at Spring-8, beamline BL40B2, see Fig. 49), to evaluate the effect of titania deposition on sample morphology and 2D array structure. The SEM and AFM images reveal that titania is deposited on the array, preferably in the space near the gap between AuNPs, even though the titania layer is inhomogeneous, while the SAXS patterns indicate that the 2D array structure is retained, since only a small shift in the peak position was observed (corresponding to a shift in the interparticle distance of about 0.8 nm comparing the SAXS pattern before and after TMOS and titania deposition).

6.4 Preparation of control samples for photocatalytic degradation of methylene blue

A quartz sample coated with titania nanocrystals was prepared by immersing an ITO substrate in a 5% v/v 3-mercaptopropyltrimethoxysilane solution in methanol overnight and then rinsing with methanol three times. With this method a silane terminated substrate was obtained, analogous to the terminal group of the TMOS coated 2D array. The MPTMS functionalized substrate was then immersed in the titania nanocrystals solution at 37 °C overnight, rinsed in DI water and annealed at 90 °C for 12 h.

The quartz reference sample was prepared by immersing the quartz substrate in piranha solution (H_2SO_4 30%: H_2O_2 = 2:1 v/v; handle with care: piranha solution is highly corrosive and reacts violently with organic matter). The AuNPs 2D array reference sample was prepared following the same procedure reported in Chapter 3.1.4.

6.5 TPA-induced photodegradation of methylene blue

The layered device was designed and fabricated to enable visible light activity in titania nanocystals deposited on the top of the array by means of the strong NF light induced by the 2D array of AuNPs. The device was prepared as follows: a 2D array of AuNPs was deposited on a transparent conductive substrate (10 nm ITO on quartz), then an anchoring molecule (TMOS) was arranged on the array to enable strong attachment between AuNPs and the titania nanocrystals, as shown in Fig. 50.

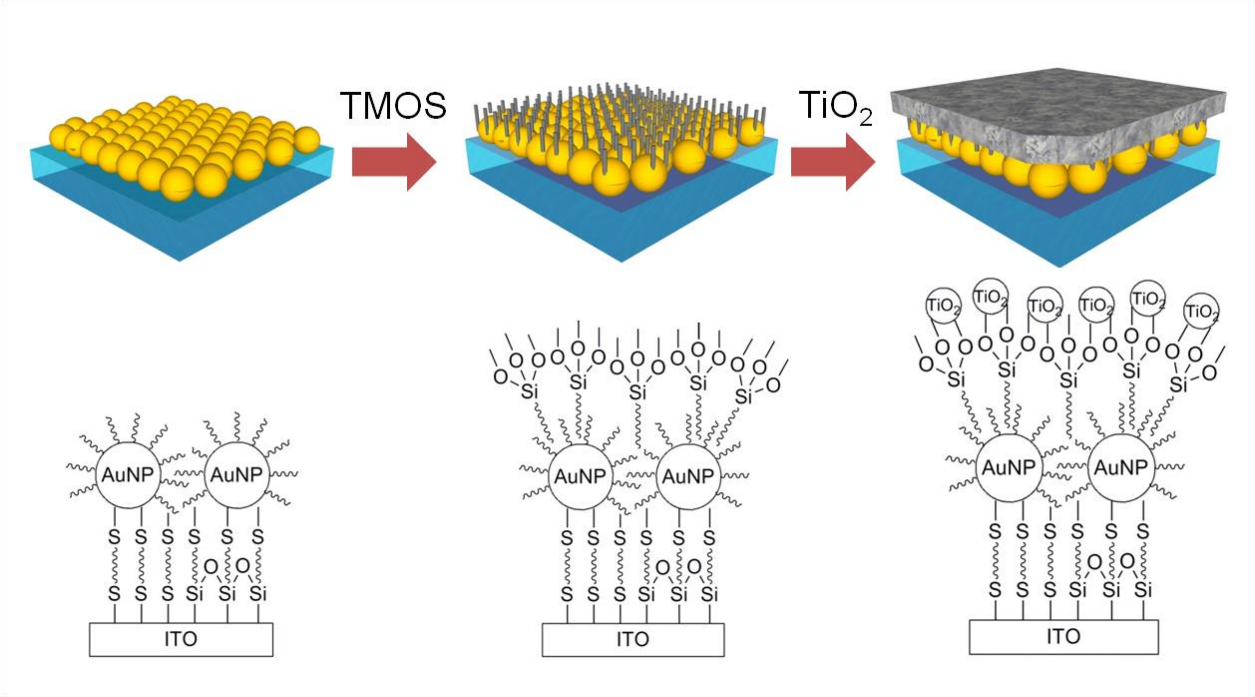

Figure 50 Schematic illustration of process of preparing the proposed plasmonic photocatalyst.

AuNPs were synthesized by the citrate reduction method (average size 36 nm ± 6), as described in Chapter 3.1.3.[28] The 36 nm AuNPs were then capped with mixed alkanethiols (hexanethiols:dodecanethiols = 3:1). The AuNPs were then arrayed on a thiol-terminated ITO/quartz substrate by means of our hybrid deposition method, which uses electrophoretic deposition, solvent evaporation and self-assembly to form a monolayer which is strongly bound to the substrate. Briefly, AuNPs were redispersed in 6 mL of hexane–acetone (3:1 v/v) and added to an open vessel where a voltage (1.1 V) was applied between the thiol-terminated ITO substrate (cathode) and plastic carbon (anode) electrodes placed 1.2 mm apart from each other. After solvent evaporation was completed, the sample was annealed at 50 °C for 12 h to enable chemisorption (Au-S bond) of AuNPs on the functionalized ITO substrates. Finally, the sample was sonicated in hexane for 30 s to remove multilayers. The AuNP coverage exceeded 90% over the whole substrate area (1 × 1 cm^2) as shown in Fig. 51a.

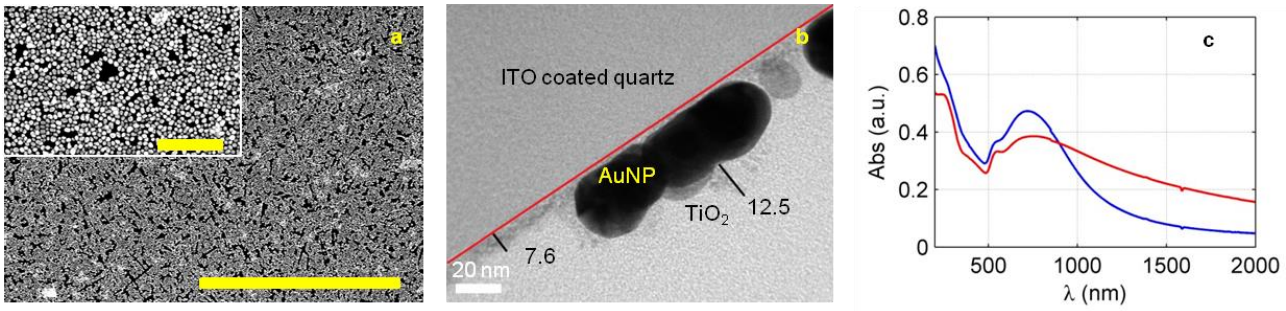

Figure 51(a) SEM micrograph of the 2D array of 36 nm AuNPs (the scale bar is 5 μm). Inset: high magnification (the scale bar is 500 nm). (b) TEM cross-sectional image of the titania coated 2D array. The two black lines indicate the titania layer thickness in nm, the red line indicates the top of the ITO layer. (c) Extinction spectra of 2D array before (blue line) and after titania coating and annealing (red line).

The surface of the 2D array was further functionalized by TMOS to result in siloxane termination, taking advantage of the intermolecular hydrophobic interaction between alkyl chains. The 2D array of AuNPs was coated with a monolayer of TMOS by dropping 20 μL of a 1% v/v solution of TMOS in MeOH onto the 2D array. The sample was kept in a MeOH vapor-saturated environment for 1 h, rinsed with MeOH and dried with

a nitrogen stream. The anchoring molecule will both induce strong mechanical durability of the titania layer (see Fig. 46) and act as a thin dielectric layer to partially inhibit charge transfer between AuNPs and TiO_2. Small titania nancocrystals (mean diameter of approx. 3.5 nm, anatase phase with trace rutile, see Fig. 45) were chosen to allow fast migration of the e–h pair at the surface and also to fully take advantage of the NF light in the proximity of the gap between AuNPs. Titania deposition was performed by immersing the sample in a solution of titania nanocrystals in ethanol–water overnight at 37 °C, rinsing the sample with DI water and annealing at 90 °C for 12 h.

The titania coated 2D array was then characterized by UV-Vis-NIR spectroscopy, SEM, AFM and SAXS to verify the effective deposition of the titania nanocrystals (see Fig. 48, 49, 51). The average thickness (7.6 nm) of the titania layer on the array corresponds to about two layers of nanocrystals, as confirmed from TEM cross-sectional images (see Fig. 51b). As these results indicate, this device takes full advantage of a chemical bottom-up approach since each solid layer is strongly attached by molecular building blocks whose mutual interactions contribute to the construction of a complex multilayered device: dithiols self-organize on the ITO surface, metallic nanoparticles are immobilized on the substrate due to Au-S bonds, TMOS is attached to the metallic particles via hydrophobic interaction, and titania is immobilized through Ti–O–Si covalent bonds.[144]

In order to test the visible light activity of our device, photocatalytic degradation of methylene blue (MB) was performed by illuminating our device and the control samples with visible light (700 nm light) and UV light (250–380 nm). Irradiation with 700 nm light was chosen in order to excite the LSPR of the 2D array, while concurrently minimizing the direct excitation of MB. Instead, UV irradiation was used to verify the photodegradation activity of the array when TiO_2 was excited directly (photon energy is sufficient to induce e–h pair creation). Control samples, namely bare quartz, a 2D array of AuNPs and quartz coated with titania nanocrystals, were prepared in order to rule out different pathways for organic dye photodegradation, such as self-sensitization,[145,146] direct photolysis,[147] and degradation by LSPR heating.[95]

Samples for photocatalytic degradation of MB were prepared by drop-casting 40 μL of 65 μM solution of MB in MeOH on the samples (at 90 °C) giving a dye density of about 16 nmol/cm^2. Each sample was irradiated with a 300 W Xe lamp (MAX-302, Asahi Spectra Co., Ltd.) equipped with UV (250–385 nm), Vis (385–740 nm) and IR (750–1050 nm) mirrors and different bandpass filters (700 nm with 10 nm FWHM filter). MB photodegradation was performed in air since oxygen in air acts as an electron scavenger, having the multiple effects of inhibiting fast recombination of the e–h pair, avoiding the reduction of MB to leucomethylene blue (LMB), and providing reactive oxygen species that contribute to MB photodegradation.[148]

In order to evaluate the photocatalytic activity of all samples, the extinction spectrum was checked at regular intervals and the degradation rate was evaluated from the peak intensity decrease versus irradiation time (see Fig. 52).

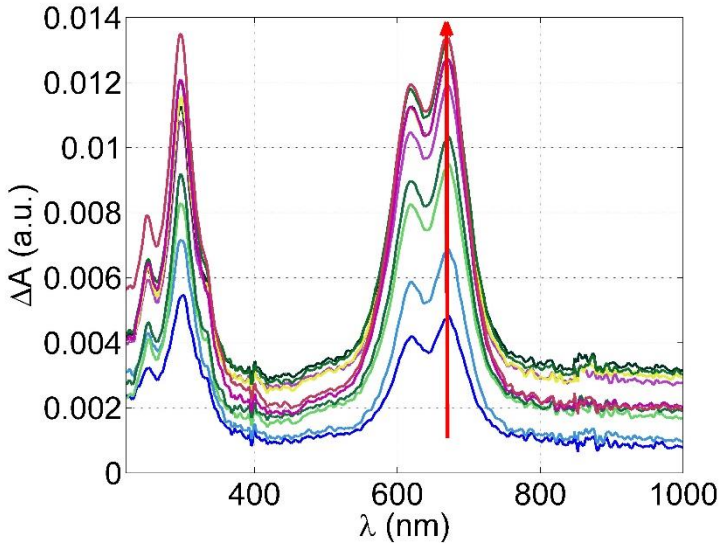

Figure 52 Plots of di_erence absorbance (ΔA) spectra (spectrum after irradiation is sub-tracted from initial spectrum) obtained after MB photocatalytic degradation on titania coated 2D array with 700 nm light irradiation (excitation λ=700 nm, FWHM= 10 nm) for different amounts of time: delta absorbance increases from 1 min irradiation (blue line) to 15 min irradiation (brown line). Spectra were acquired at 1 min intervals from 1 min to 8 min and then after 10 and 15 min of irradiation.

For each value of MB peak intensity the sample was stored in the dark for 15 min after irradiation and prior to acquisition of the UV-Vis spectrum to ensure equilibrium (three UV-Vis spectra were collected after irradiation at 5 min intervals to verify the relaxation to equilibrium). Initial reaction steps of all samples showed pseudo first-order kinetics, thus each photocatalytic degradation rate k was obtained from the linear fit of:

$$\ln(I / I_0) = -k \cdot t \qquad (23)$$

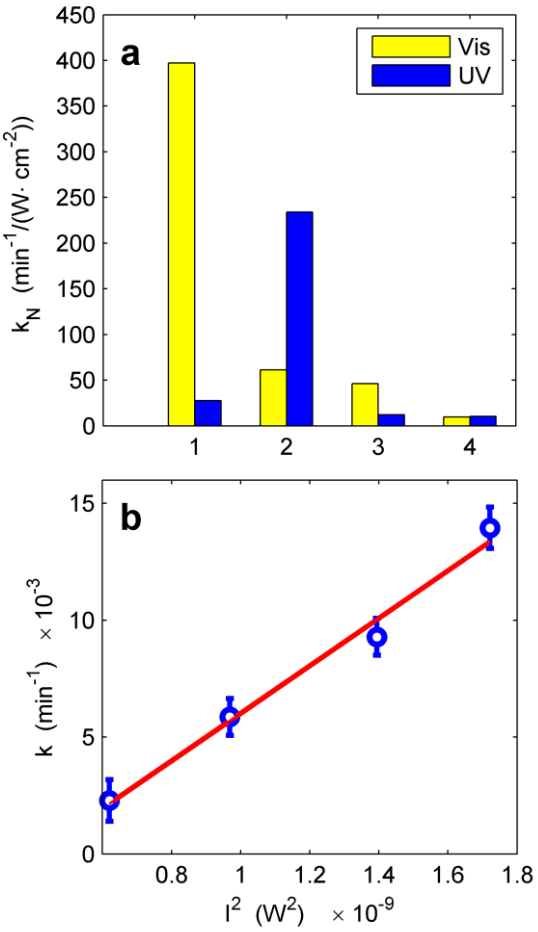

Figure 53 (a) Histogram showing the normalized photocatalytic degradation rate calculated from the initial photocatalytic degradation rate for various samples. Values on the x axis correspond to four different samples coated with MB to perform the photocatalytic degradation experiment. The samples are: (1) titania coated 2D array, (2) titania coated ITO substrate, (3) 2D array and (4) bare quartz substrate. (b) Linear fitting of photocatalytic degradation rate versus second power of the incident light.

The values of photocatalytic activity are shown in Fig. 53 as MB degradation rate divided by incident power for all samples (device and control samples) and for both visible (700 nm, 10 nm FWHM) and UV irradiation (250–385 nm). The maximum photocatalytic activity was achieved with the titania coated 2D array excited with visible light as expected. Note that the value of photocatalytic activity of the titania coated 2D array exceeds the photocatalytic activity of the titania nanocrystal coated ITO sample irradiated with UV light by 1.7 times. In addition, the photocatalytic activity of the titania coated 2D array irradiated with visible light was 14 times higher than that irradiated with UV light; the low photocatalytic activity of the layered device under UV irradiation is probably due to the previously proposed[93] charge depletion (Schottky barrier at the titania/Au interface) from titania to AuNPs and to the high extinction of Au in the UV region. By evaluating the photocatalytic degradation rate for the titania sample irradiated with visible light in Fig. 53, it was possible to exclude major contributions from the direct visible light activity of titania (the bandgap of titania nanocrystals was calculated from the UV-Vis extinction spectrum to be 3.34 eV) and self-sensitization, which consist of excitation of dye by visible light, consequent transfer of energy from the dye (typical mechanism of dye-sensitized cells) to the oxide semiconductor which then undergoes e–h pair creation, and finally charge transfer to the dye, inducing photocatalytic degradation. The low degradation rate for the MB coated quartz substrate also indicated that direct photolysis was not the main contributor to the visible light activity of the device. Lastly, by comparing the photocatalytic degradation rate of the titania coated array and the uncoated 2D array, the possibility that the LSPR effect by itself (plasmonic heat[149] or energy transfer[150]) is responsible for visible light photocatalytic degradation was excluded, that is, excitation of MNPs alone is not able to induce a

noticeable modification of MB. In conclusion, the combination of MNPs 2D array and titania layer was proven indispensable for obtaining visible-light induced photocatalytic activity.

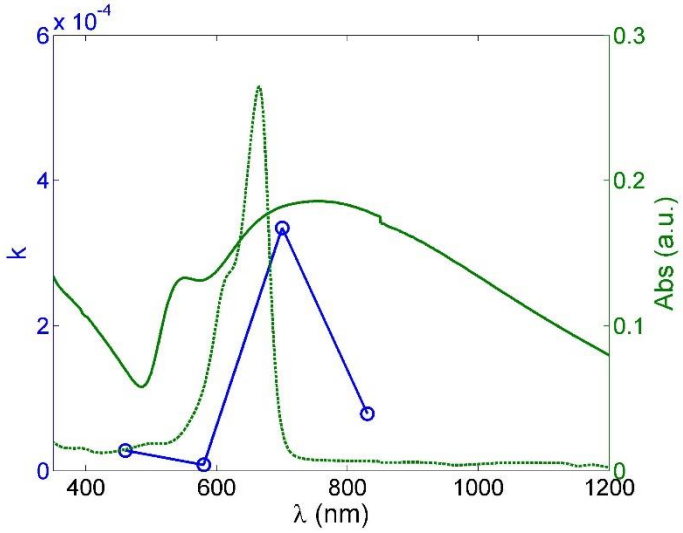

Figure 54 Action spectra of photocatalytic degradation rate per unit power versus excitation wavelength (λ = 480, 560, 700, 830 nm). Comparison of photocatalytic degradation rate (k) with absorbance spectrum of MB (dotted line) and extinction spectrum of titania coated 2D array (green line).

Once different reaction pathways were excluded, the origin of the visible light activity of titania could be investigated. To do this, the dependence of photocatalytic degradation rate on excitation wavelength (see Fig. 54) was checked. From analysis of the action spectrum it was found that the maximum photodegradation rate corresponded with the peak value of LSPR, and that the tendency of the rate was similar to the shape of the LSPR peak, suggesting plasmon-induced visible light activity. In fact, this tendency is in agreement with a well-known property of MNPs (this property is valid for small spherical MNPs for which the far-field and near-field resonant frequencies overlap completely[120]), namely that the highest near-field enhancement can be achieved when light is resonant with the MNPs' LSPR (wavelength of the excitation light corresponds to the LSPR peak of the MNPs' UV-Vis spectrum).

Plasmon-induced visible light activity can originate from different interactions of MNPs with titania, therefore further analysis is needed. Direct plasmonic excitation can be partially ruled out, namely direct enhancement of visible light activity, due to the large bandgap of titania nanocrystals, allowing excitation only by UV light and LSPR of the 2D array, which instead lies in the NIR region of 755 nm. A second direct mechanism, "hot electron" transfer, is also partially inhibited owing to the TMOS layer deposited on the AuNPs. Excluding these two mechanisms and considering that the LSPR wavelength of our plasmonic device (755 nm) corresponds to about twice the wavelength relative to the titania bandgap (371 nm), TPA was assumed to be the main contributor to the visible light activity of titania (excitation resonant with the LSPR is able to induce the formation of e–h pairs in titania due to simultaneous absorption of two photons). To verify this assumption MB photocatalytic degradation was performed with 700 nm light while varying the incident power with a neutral density filter. It is well-known that the power dependence of titania photocatalytic reactions is affected by the titania thickness; in the case of the bulk state, only the region near the surface of titania would contribute to photocatalytic reactions owing to the short lifetime of the photocarriers and the power dependence would follow a root-square power law. In the case of nanosized titania, a linear power dependence was verified since all photogenerated charges can migrate at the interface and contribute to the reaction. In our experiment the small size of titania nanocrystals (3.5 nm) would suggest a linear behavior in case of linear absorption.

However, the experimental results shown in Fig. 53b indicate a square power dependence, which clearly shows that the photocatalytic degradation of MB is induced by TPA with embedded AuNP arrays.

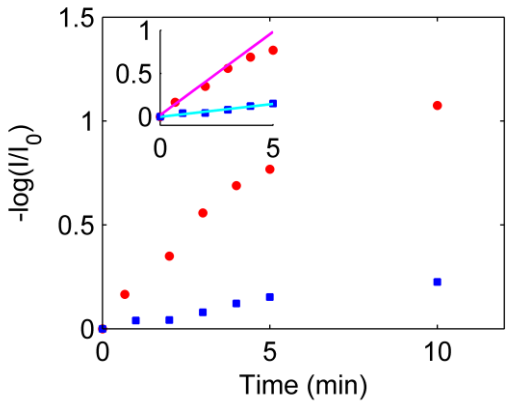

Figure 55 MB photocatalytic degradation under wide band visible light illumination. The photocatalytic degradation experiment was performed with titania coated ITO substrate (red circles) and titania coated 2D array (blue squares). Inset: pseudo first-order kinetics of initial reaction steps for titania coated 2D array and titania sample.

Finally, the photocatalytic activity of our device was investigated under wide band visible light illumination (Xe lamp with 422–750 nm filter). The result of visible light irradiation confirmed the higher photocatalytic activity (6.5 times higher) of our sample compared to the reference sample, as shown in Fig. 55. This result shows that visible light is suitable for the excitation of wide LSPR absorption of 2D arrays of AuNPs.

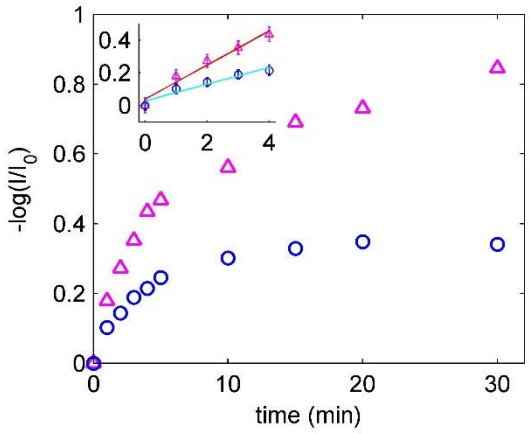

Figure 56 MB photocatalytic degradation under solar illumination. The photocatalytic degradation experiment was performed with titania coated ITO substrate (circles in the figure) and titania coated 2D array (triangles in the figure). Inset: pseudo first-order kinetics of initial reaction steps for titania coated 2D array and titania sample.

In addition, solar light irradiation was tested and the result (the photocatalytic activity of our device was twice that of the titania reference; see Fig. 56) showed the potential of our photocatalytic device for converting solar energy to chemical energy.

6.6 Conclusions

In summary, a visible light photocatalytic device was fabricated by means of only wet chemical bottom-up deposition processes, without needing expensive clean-room deposition processes or high-temperature

treatments. The photocatalytic activity of the device was investigated by photocatalytic degradation of MB with visible and UV irradiation. In comparison with other control samples, our device showed the highest photocatalytic activity with visible irradiation, which was 1.7 times higher than that of titania with UV irradiation. The origin of such visible light activity was confirmed to be TPA by both quadratic incident light power dependency and action spectrum. TPA was proven to be induced by the strong NF light originating in the proximity of AuNPs when localized surface plasmons were excited ($\lambda_{ex} \approx \lambda_{LSPR}$). The result of MB photocatalytic degradation with a titania coated 2D array under wide band visible light irradiation is encouraging, since the photocatalytic degradation rate for a titania coated 2D array is more than six times that of the titania sample.

7. Conclusions

In conclusion, promising plasmonic arrays of Au@Ag NPs were obtained by means of a facile self-assembly-based bottom-up deposition method. These arrays were characterized experimentally by UV-Vis spectroscopy and SERS, and their optical response was also studied computationally, revealing their potential as efficient SERS substrate in the visible range. The highest average enhancement factor was achieved for 2D array prepared with the largest Au@Ag NPs (5.9×10^6) comparable with results from self-assembled films of silver nanoparticles. The SERS enhancement factor was also proven to be homogeneous over the substrate, showing the high potential of this self-assembled 2D array as SERS-based sensor. In addition, SERS and DDA simulations revealed that the near-field optical response of Au@Ag 2D arrays can be greatly affected by various parameters, such as particle size, Ag:Au ratio and aggregation. In case of 40Au@Ag series, in fact, an increase of the enhancement factor close to two orders of magnitude was found upon silver shell growth. In addition, the near-field response of the 2D array was found to differ remarkably from the far-field response, the latter in fact cannot account both for the exact position (redshift) and for the intensity of the maximum enhancement.

By employing the same 2D arrays it was possible to expand the applicability of plasmonic metallic nanostructures to induce a TPA reaction. A series of AuNP arrays was fabricated bearing LSPR ranging from UV, Vis, to NIR region depending on the AuNP size. Incoherent light in various wavelength ranges was irradiated to ACA-coated AuNP arrays and the photoreaction products were analyzed by SERS measurement and mass spectroscopy. The results confirmed that TPA-induced reaction requires matching between irradiation wavelength, LSPR, and twice the wavelength (half photon energy) of molecular excitation ($\lambda_{irr} \equiv \lambda_{LSPR} \equiv 2\,\lambda_{ex}$). In addition, it was found that even when matched conditions are met, the size of the AuNPs strongly affects the progress of the TPA-induced reaction. It was suggested by both DFT-calculated Raman analysis and mass spectra that the formation of HBAC had occurred through TPA-induced reaction at the surface of the 23HexDod array by Vis irradiation, while it was demonstrated by ^{1}H NMR that solution-phase TPA-induced reaction of ACA gave ACAD. Although higher reaction efficiency is necessary to apply TPA-induced reaction for chemical synthesis, this limitation can be overcome by combining AuNP array substrates with microchannel reaction systems, making this system a promising candidate for the development of an efficient and cost-effective "lab-on-a-chip" for photoreactions.

Lastly, a visible light photocatalytic device was fabricated incorporating our 2D array of metallic nanoparticles in a self-assembly-based layered structure. The photocatalytic activity of the device was investigated by photocatalytic degradation of MB with visible and UV irradiation. In comparison with other control samples, our device showed the highest photocatalytic activity with visible irradiation, which was 1.7 times higher than that of titania with UV irradiation. The origin of such visible light activity was confirmed to be TPA by both quadratic incident light power dependency and action spectrum. TPA was proven to be induced by the strong near-field light originating in the proximity of AuNPs when localized surface plasmons were excited ($\lambda_{ex} \approx \lambda_{LSPR}$). The result of MB photocatalytic degradation with a titania coated 2D array under wide band visible light irradiation is encouraging, since the photocatalytic degradation rate for a titania coated 2D array is more than six times that of the titania sample.

References

(1) Shalaev, V. *Nat. Photonics* **2007**, *1*, 41–48.

(2) Butet, J.; Bachelier, G.; Russier-Antoine, I.; Jonin, C.; Benichou, E.; Brevet, P.-F. *Phys. Rev. Lett.* **2010**, *105*, 077401.

(3) Orsi, D.; Cristofolini, L.; Baldi, G.; Madsen, A. *Phys. Rev. Lett.* **2012**, *108*, 105701.

(4) Mazurenko, D.; Shan, X.; Stiefelhagen, J.; Graf, C.; van Blaaderen, a.; Dijkhuis, J. *Phys. Rev. B* **2007**, *75*, 161102.

(5) Haruta, M. *Chem. Rec.* **2003**, *3*, 75–87.

(6) Taguchi, T.; Isozaki, K.; Miki, K. *Adv. Mater.* **2012**, *24*, 6462–6467.

(7) Geddes, C.; Cao, H. *J. Phys. Chem. A* **2003**, *107*, 3443–3449.

(8) Atwater, H. A.; Polman, A. *Nat. Mater.* **2010**, *9*, 205–213.

(9) Kennedy, L. C.; Bickford, L. R.; Lewinski, N. A.; Coughlin, A. J.; Hu, Y.; Day, E. S.; West, J. L.; Drezek, R. A. *Small* **2011**, *7*, 169–183.

(10) Daniel, M. M.-C.; Astruc, D. *Chem. Rev.* **2004**, *104*, 293–346.

(11) Lee, J.; Mubeen, S.; Ji, X.; Stucky, G. D.; Moskovits, M. *Nano Lett.* **2012**, *12*, 5014–5019.

(12) Haruta, M. *Catal. Today* **1997**, *861*, 153–166.

(13) Lee, K.-S.; El-Sayed, M. a. *J. Phys. Chem. B* **2006**, *110*, 19220–19225.

(14) Liz-Marzán, L. *Langmuir* **2006**, 32–41.

(15) Hentschel, M.; Saliba, M.; Vogelgesang, R.; Giessen, H.; Alivisatos, a P.; Liu, N. *Nano Lett.* **2010**, *10*, 2721–2726.

(16) Chang, W.-S. W.; Willingham, B.; Slaughter, L. S.; Dominguez-Medina, S.; Swanglap, P.; Link, S. *Acc. Chem. Res.* **2012**, *45*, 1936–1945.

(17) Halas, N. J.; Lal, S.; Chang, W.-S.; Link, S.; Nordlander, P. *Chem. Rev.* **2011**, *111*, 3913–3961.

(18) Kneipp, K.; Kneipp, H.; Kneipp, J. *Acc. Chem. Res.* **2006**, 443–450.

(19) Fan, J. a; Wu, C.; Bao, K.; Bao, J.; Bardhan, R.; Halas, N. J.; Manoharan, V. N.; Nordlander, P.; Shvets, G.; Capasso, F. *Science* **2010**, *328*, 1135–1138.

(20) Gallinet, B.; Martin, O. J. F. *ACS Nano* **2011**, *5*, 8999–9008.

(21) Lassiter, J. B.; Sobhani, H.; Knight, M. W.; Mielczarek, W. S.; Nordlander, P.; Halas, N. J. *Nano Lett.* **2012**, *12*, 1058–1062.

(22) Pelton, M.; Aizpurua, J.; Bryant, G. *Laser Photonics Rev.* **2008**, *2*, 136–159.

(23) Joseph, V.; Gensler, M.; Seifert, S.; Gernert, U.; Rabe, J. P.; Kneipp, J. *J. Phys. Chem. C* **2012**, *116*, 6859–6865.

(24) Wang, Y.; Chen, H.; Wang, E. *Nanotechnology* **2008**, *19*, 105604.

(25) Isozaki, K.; Ochiai, T.; Taguchi, T.; Nittoh, K.; Miki, K. *Appl. Phys. Lett.* **2010**, *97*, 221101.

(26) Dadosh, T. *Mater. Lett.* **2009**, *63*, 2236–2238.

(27) Cathcart, N.; Kitaev, V. *Nanoscale* **2012**, *4*, 6981–6989.

(28) Shankar, C.; Dao, A.; Singh, P.; Higashimine, K.; Mott, F. M.; Maenosono, S. *Nanotechnology* **2012**, *23*, 245704.

(29) Mott, D.; Lee, J.; Thuy, N. T. B.; Aoki, Y.; Singh, P.; Maenosono, S. *Jpn. J. Appl. Phys.* **2011**, *50*, 065004.

(30) Jana, N. R. *Analyst* **2003**, *128*, 954–956.

(31) Jiang, R.; Chen, H.; Shao, L.; Li, Q.; Wang, J. *Adv. Mater.* **2012**, *24*, OP200–7.

(32) Yang, Y.; Shi, J.; Kawamura, G.; Nogami, M. *Scr. Mater.* **2008**, *58*, 862–865.

(33) Zhu, H.; Bao, L.; Mahurin, S. M.; Baker, G. a.; Hagaman, E. W.; Dai, S. *J. Mater. Chem.* **2008**, *18*, 1079.

(34) Inoue, M.; Ohtaka, K. *J. Phys. Soc. Japan* **1983**, *52*, 3853–3864.

(35) Bhawalkar, J.; He, G.; Prasad, P. *Reports Prog. Phys.* **1996**, *59*, 1041–1070.

(36) Ueno, K.; Juodkazis, S.; Mizeikis, V.; Sasaki, K.; Misawa, H. *Adv. Mater.* **2008**, *20*, 26–30.

(37) Ueno, K.; Juodkazis, S.; Shibuya, T.; Yokota, Y.; Mizeikis, V.; Sasaki, K.; Misawa, H. *J. Am. Chem. Soc.* **2008**, *130*, 6928–6929.

(38) Tsuboi, Y.; Shimizu, R.; Shoji, T.; Kitamura, N. *J. Am. Chem. Soc.* **2009**, *131*, 12623–12627.

(39) Ochiai, T.; Isozaki, K.; Pincella, F.; Taguchi, T.; Nittoh, K.; Miki, K. *Appl. Phys. Express* **2013**, *6*, 102001.

(40) O'Donnell, M. *Nature* **1968**, *218*, 460–461.

(41) Sigman, M. E.; Zingg, S. P.; Pagni, R. M.; Burns, J. H. *Tetrahedron Lett.* **1991**, *32*, 5737–5740.

(42) Debestani, R.; Ellis, K.; Sigman, M. *J. Photochem. Photobiol. A Chem.* **1995**, *86*, 231–239.

(43) Yatsuhashi, T.; Nakahagi, Y.; Okamoto, H.; Nakashima, N. *J. Phys. Chem. A* **2010**, *114*, 10475–10480.

(44) Pelton, M.; Bryant, G. *Introduction to metal-nanoparticle plasmonics*; Wiley ScienceWise, 2013.

(45) Barnes, W.; Dereux, A.; Ebbesen, T. *Nature* **2003**, *424*, 824–830.

(46) Myroshnychenko, V.; Rodríguez-Fernández, J.; Pastoriza-Santos, I.; Funston, A. M.; Novo, C.; Mulvaney, P.; Liz-Marzán, L. M.; García de Abajo, F. J. *Chem. Soc. Rev.* **2008**, *37*, 1792–1805.

(47) Knight, M. W.; Wu, Y.; Lassiter, J. B.; Nordlander, P.; Halas, N. J. *Nano Lett.* **2009**, *9*, 2188–2192.

(48) Prodan, E.; Radloff, C.; Halas, N. J.; Nordlander, P. *Science* **2003**, *302*, 419–422.

(49) Nordlander, P.; Oubre, C.; Prodan, E.; Li, K.; Stockman, M. I. *Nano Lett.* **2004**, *4*, 899–903.

(50) Prodan, E.; Nordlander, P. *Nano Lett.* **2004**, *4*, 2209–2213.

(51) Le, F.; Lwin, N. Z.; Steele, J. M.; Käll, M.; Halas, N. J.; Nordlander, P. *Nano Lett.* **2005**, *5*, 2009–2013.

(52) Hu, M.; Ghoshal, A. *J. Phys. Chem. C* **2010**, *114*, 7509–7514.

(53) Park, T.-H.; Nordlander, P. *Chem. Phys. Lett.* **2009**, *472*, 228–231.

(54) Bardhan, R.; Mukherjee, S.; Mirin, N. a.; Levit, S. D.; Nordlander, P.; Halas, N. J. *J. Phys. Chem. C* **2009**, *114*, 7378–7383.

(55) Wu, D. J.; Liu, X. J. *Appl. Phys. B* **2009**, *97*, 193–197.

(56) Kreibig, U.; Vollmer, M. *Optical Properties of Metal Clusters*; Springer: New York, 1995.

(57) Teperik, T.; Borisov, a. *Phys. Rev. B* **2009**, *79*, 245409.

(58) Draine, B. T.; Flatau, P. J. *J. Opt. Soc. Am. A* **1994**, *11*, 1491–1499.

(59) Draine, B. T.; Flatau, P. J. *J. Opt. Soc. Am. A. Opt. Image Sci. Vis.* **2008**, *25*, 2693–2703.

(60) Flatau, P. J.; Draine, B. T. *Opt. Express* **2012**, *20*, 1247–1252.

(61) Hao, E.; Schatz, G. C. *J. Chem. Phys.* **2004**, *120*, 357–366.

(62) Yang, W.-H.; Schatz, G. C.; Van Duyne, R. P. *J. Chem. Phys.* **1995**, *103*, 869.

(63) Lindquist, N.; Nagpal, P. *Reports Prog. Phys.* **2012**, *75*, 1–119.

(64) Skrabalak, S.; Chen, J.; Sun, Y.; Lu, X. *Acc. Chem. Res.* **2008**, *41*, 1587–1595.

(65) Sun, Y.; Xia, Y. *Science (80-.).* **2002**, *298*, 2176–2179.

(66) Ulman, A. *Chem. Rev.* **1996**, *96*, 1533–1554.

(67) Pincella, F.; Camorani, P.; Erokhin, V. *Appl. Phys. A* **2011**, *104*, 1039–1046.

(68) Bourgoin, J.; Kergueris, C.; Lefevre, E.; Palacin, S. *Thin Solid Films* **1998**, *327-329*, 515–519.

(69) Orsi, D.; Vezzani, A.; Burioni, R.; Pucci, A.; Ruggeri, G.; Cristofolini, L. *Colloids Surfaces A Physicochem. Eng. Asp.* **2014**, *441*, 912–918.

(70) Moskovits, M. *J. Raman Spectrosc.* **2005**, *36*, 485–496.

(71) Moskovits, M. *Rev. Mod. Phys.* **1985**, *57*, 783–826.

(72) Wu, B.; Ueno, K.; Yokota, Y.; Sun, K.; Zeng, H.; Misawa, H. *J. Phys. Chem. Lett.* **2012**, *3*, 1443–1447.

(73) Fleischmann, M.; Hendra, P.; McQuillan, A. *Chem. Phys. Lett.* **1974**, *26*, 2–5.

(74) King, F. W.; Van Duyne, R. P.; Schatz, G. C. *J. Chem. Phys.* **1978**, *69*, 4472.

(75) Albrecht, M.; Creighton, J. *J. Am. Chem. …* **1977**, *99*, 5215–5217.

(76) Kneipp, K.; Wang, Y.; Kneipp, H.; Perelman, L.; Itzkan, I.; Dasari, R.; Feld, M. *Phys. Rev. Lett.* **1997**, *78*, 1667–1670.

(77) Kneipp, K.; Kneipp, H.; Itzkan, I.; Dasari, R. R.; Feld, M. S. *J. Phys. Condens. Matter* **2002**, *14*, R597–R624.

(78) Kang, T.; Yoo, S. M.; Yoon, I.; Lee, S. Y.; Kim, B. *Nano Lett.* **2010**, *10*, 1189–1193.

(79) Leyton, P.; Sanchez-Cortes, S.; Garcia-Ramos, J. V.; Domingo, C.; Campos-Vallette, M.; Saitz, C.; Clavijo, R. E. *J. Phys. Chem. B* **2004**, *108*, 17484–17490.

(80) Liu, T.-T.; Lin, Y.-H.; Hung, C.-S.; Liu, T.-J.; Chen, Y.; Huang, Y.-C.; Tsai, T.-H.; Wang, H.-H.; Wang, D.-W.; Wang, J.-K.; Wang, Y.-L.; Lin, C.-H. *PLoS One* **2009**, *4*, e5470.

(81) Natan, M. J. *Faraday Discuss.* **2006**, *132*, 321–328.

(82) Göppert-Mayer, M. *Ann. Phys.* **2009**, *18*, 466–479.

(83) Kaiser, W.; Garrett, C. *Phys. Rev. Lett.* **1961**, *7*, 229–232.

(84) Maruo, S.; Nakamura, O.; Kawata, S. *Opt. Lett.* **1997**, *22*, 132–134.

(85) Denk, W.; Strickler, J. H.; Webb, W. W. *Science (80-.).* **1990**, *248*, 73–76.

(86) Corredor, C.; Huang, Z. *Chem. Mater.* **2007**, *19*, 5165–5173.

(87) Kim, H.; Kreiling, S.; Greiner, A.; Hampp, N. *Chem. Phys. Lett.* **2003**, *372*, 899–903.

(88) Brillet, J.; Yum, J. J.-H.; Cornuz, M.; Hisatomi, T.; Solarska, R.; Augustynski, J.; Graetzel, M.; Sivula, K. *Nat. Photonics* **2012**, *6*, 1–5.

(89) Wu, Y.; Liu, H.; Zhang, J.; Chen, F. *J. Phys. Chem. C* **2009**, *113*, 14689–14695.

(90) Zhao, W.; Chen, C.; Li, X.; Zhao, J.; Hidaka, H.; Serpone, N. *J. Phys. Chem. B* **2002**, *106*, 5022–5028.

(91) Grätzel, M. *Nature* **2001**, *414*, 338 – 344.

(92) Mukherjee, S.; Libisch, F.; Large, N. *Nano Lett.* **2013**, *13*, 240–247.

(93) Mubeen, S.; Hernandez-Sosa, G.; Moses, D.; Lee, J.; Moskovits, M. *Nano Lett.* **2011**, 0–4.

(94) Rodríguez-Oliveros, R.; Sánchez-Gil, J. *Opt. Express* **2012**, *20*, 402–407.

(95) Alessandri, I.; Depero, L. E. *Chem. Commun.* **2009**, 2359–2361.

(96) Christopher, P.; Ingram, D. B.; Linic, S. *J. Phys. Chem. C* **2010**, *114*, 9173–9177.

(97) Jana, N.; Gearheart, L.; Murphy, C. *Langmuir* **2001**, 6782–6786.

(98) Frens, G. *Nature* **1973**, *241*, 20–22.

(99) Park, Y.-K.; Park, S. *Chem. Mater.* **2008**, *20*, 2388–2393.

(100) Frisch, M. J.; Trucks, G. W.; Schlegel, H. B.; Scuseria, G. E.; M. A. Robb, J. R. Cheeseman, J. A. Montgomery, J.; Vreven, T.; Kudin, K. N.; Burant, J. C.; Millam, J. M.; Iyengar, S. S.; Tomasi, J.; Barone, V.; Mennucci, B.; Cossi, M.; Scalmani, G.; Rega, N.; Petersson, G. A.; Nakatsuji, H.; Hada, M.; Ehara, M.; Toyota, K.; Fukuda, R.; Hasegawa, J.; Ishida, M.; Nakajima, T.; Honda, Y.; Kitao, O.; Nakai, H.; Klene, M.; Li, X.; Knox, J. E.; Hratchian, H. P.; Cross, J. B.; Bakken, V.; Adamo, C.; Jaramillo, J.; Gomperts, R.; Stratmann, R. E.; Yazyev, O.; Austin, A. J.; Cammi, R.; Pomelli, C.; Ochterski, J. W.; Ayala, P. Y.; Morokuma, K.; Voth, G. A.; Salvador, P.; Dannenberg, J. J.; Zakrzewski, V. G.; Dapprich, S.; Daniels, A. D.; Strain, M. C.; Farkas, O.; Malick, D. K.; Rabuck, A. D.; Raghavachari, K.; Foresman, J. B.; Ortiz, J. V.; Cui, Q.; Baboul, A. G.; Clifford, S.; Cioslowski, J.; Stefanov, B. B.; Liu, G.; Liashenko, A.; Piskorz, P.; Komaromi, I.; Martin, R. L.; Fox, D. J.; Keith, T.; Al-Laham, M. A.; Peng, C. Y.; Nanayakkara, A.; Challacombe, M. W.; Gill, P. M.; Johnson, B.; Chen, W.; Wong, M. W.; C. Gonzalez, A.; J. A. Pople. Gaussian 03, 2004.

(101) Hutter, T.; Elliott, S. R.; Mahajan, S. *Nanotechnology* **2013**, *24*, 035201.

(102) Rhodes, C.; Franzen, S.; Maria, J.-P.; Losego, M.; Leonard, D. N.; Laughlin, B.; Duscher, G.; Weibel, S. *J. Appl. Phys.* **2006**, *100*, 054905.

(103) Johnson, P.; Christy, R. *Phys. Rev. B* **1972**, *6*, 4370–4379.

(104) Hale, G. M.; Querry, M. R. *Appl. Opt.* **1973**, *12*, 555–563.

(105) Yurkin, M. a.; Min, M.; Hoekstra, A. G. *Phys. Rev. E* **2010**, *82*, 036703.

(106) Piller, N.; Martin, O. *Antennas Propagation, IEEE …* **1998**, *46*, 1126–1137.

(107) Moerner, W. *J. Phys. Chem. B* **2002**, *106*, 910–927.

(108) Li, J.-M.; Wei, C.; Ma, W.-F.; An, Q.; Guo, J.; Hu, J.; Wang, C.-C. *J. Mater. Chem.* **2012**, *22*, 12100.

(109) Shafer-Peltier, K. *J. Am. Chem. Soc.* **2003**, *125*, 588–593.

(110) Jones, C. L.; Bantz, K. C.; Haynes, C. L. *Anal. Bioanal. Chem.* **2009**, *394*, 303–311.

(111) Michaels, A. M.; Brus, L. *J. Phys. Chem. B* **2000**, *104*, 11965–11971.

(112) Elking, M. D.; He, G.; Xu, Z. *J. Chem. Phys.* **1996**, *105*, 6565–6573.

(113) Kudelski, A. *Chem. Phys. Lett.* **2005**, *414*, 271–275.

(114) Ru, E. C. Le; Blackie, E.; Meyer, M.; Etchegoin, P. G. *J. Phys. Chem. C* **2007**, *111*, 13794–13803.

(115) McMahon, J. M.; Henry, A.-I.; Wustholz, K. L.; Natan, M. J.; Freeman, R. G.; Van Duyne, R. P.; Schatz, G. C. *Anal. Bioanal. Chem.* **2009**, *394*, 1819–1825.

(116) Jain, P. K.; Huang, W.; El-Sayed, M. A. *Nano Lett.* **2007**, *7*, 2080–2088.

(117) Wustholz, K. L.; Henry, A.-I.; McMahon, J. M.; Freeman, R. G.; Valley, N.; Piotti, M. E.; Natan, M. J.; Schatz, G. C.; Van Duyne, R. P. *J. Am. Chem. Soc.* **2010**, *132*, 10903–10910.

(118) McMahon, J. M.; Li, S.; Ausman, L. K.; Schatz, G. C. *J. Phys. Chem. C* **2012**, *116*, 1627–1637.

(119) Kleinman, S. L.; Sharma, B.; Blaber, M. G.; Henry, A.-I.; Valley, N.; Freeman, R. G.; Natan, M. J.; Schatz, G. C.; Van Duyne, R. P. *J. Am. Chem. Soc.* **2013**, *135*, 301–308.

(120) Bryant, G. W.; García de Abajo, F. J.; Aizpurua, J. *Nano Lett.* **2008**, *8*, 631–636.

(121) Bruzzone, S.; Malvaldi, M. *J. Phys. …* **2006**, *110*, 11050–11054.

(122) Zuloaga, J.; Nordlander, P. *Nano Lett.* **2011**, *11*, 1280–1283.

(123) Marty, R.; Baffou, G.; Arbouet, a; Girard, C.; Quidant, R. *Opt. Express* **2010**, *18*, 3035–3044.

(124) Deeb, C.; Zhou, X.; Plain, J. *J. Phys. Chem. C* **2013**, *117*, 10669–10676.

(125) Kawata, S.; Inouye, Y.; Verma, P. *Nat. Photonics* **2009**, *3*, 388–394.

(126) Sundaramurthy, A.; Schuck, P. J.; Conley, N. R.; Fromm, D. P.; Kino, G. S.; Moerner, W. E. *Nano Lett.* **2006**, *6*, 355–360.

(127) Tanaka, A.; Hashimoto, K.; Ohtani, B.; Kominami, H. *Chem. Commun.* **2013**, *49*, 3419–3421.

(128) Pincella, F.; Isozaki, K.; Miki, K. *Light Sci. Appl.* **2014**, *3*, e133.

(129) Wenseleers, W.; Stellacci, F.; Meyer-Friedrichsen, T.; Mangel, T.; Bauer, C. A.; Pond, S. J. K.; Marder, S. R.; Perry, J. W. *J. Phys. Chem. A* **2002**, *106*, 6853–6863.

(130) Fox, M.; Olive, S. *Science (80-.).* **1979**, *205*, 582–583.

(131) Sugiyama, N.; Iwata, M.; Yoshioka, M. *Bull. Chem. Soc. Jpn.* **1969**, *42*, 1377–1379.

(132) Kawanami, Y.; Umehara, H. *J. …* **2013**, *78*, 3073–3085.

(133) Dawn, A.; Shiraki, T.; Haraguchi, S.; Sato, H.; Sada, K.; Shinkai, S. *Chemistry (Easton).* **2010**, *16*, 3676–3689.

(134) Nakamura, A.; Inoue, Y. *J. Am. Chem. Soc.* **2003**, *125*, 966–972.

(135) Han, S.; Joo, S.; Ha, T. *J. Phys. Chem. B* **2000**, *104*, 11987–11995.

(136) Tamam, L.; Kraack, H.; Sloutskin, E. *J. …* **2007**, *111*, 2573–2579.

(137) Pocoví-martínez, S.; Parre, M.; Agouram, S.; Julia, P. *Langmuir* **2011**, *27*, 5234–5241.

(138) Xiao, Y.; Patolsky, F.; Katz, E.; Hainfeld, J.; Willner, I. *Science (80-.).* **2003**, *299*, 1877–1881.

(139) Wee, T.-L. (Erika); Schmidt, L. C.; Scaiano, J. C. *J. Phys. Chem. C* **2012**, *116*, 24373–24379.

(140) Choi, W.; Termin, A.; Hoffmann, M. R. *J. Phys. Chem.* **1994**, *98*, 13669–13679.

(141) Swamy, V.; Kuznetsov, A.; Dubrovinsky, L.; Caruso, R.; Shchukin, D.; Muddle, B. *Phys. Rev. B* **2005**, *71*, 184302.

(142) Serpone, N.; Lawless, D.; Khairutdinov, R. *J. Phys. Chem.* **1995**, *99*, 16646–16654.

(143) Wang, X. *Thin Solid Films* **2000**, *371*, 148–152.

(144) Niesen, T. P.; Bill, J.; Aldinger, F. *Chem. Mater.* **2001**, *13*, 1552–1559.

(145) Zhao, J.; Chen, C.; Ma, W. *Top. Catal.* **2005**, *35*, 269–278.

(146) Chatterjee, D.; Mahata, A. *J. Photochem. Photobiol. A Chem.* **2002**, *153*, 199–204.

(147) Tang, J.; Zou, Z.; Yin, J.; Ye, J. *Chem. Phys. Lett.* **2003**, *382*, 175–179.

(148) Tatsuma, T.; Tachibana, S.; Miwa, T. *J. Phys. Chem. B* **1999**, *103*, 18–20.

(149) Tong, L.; Wei, Q.; Wei, A.; Cheng, J. *Photochem. Photobiol.* **2009**, *85*, 21–32.

(150) Eichelbaum, M.; Rademann, K. *Adv. Funct. Mater.* **2009**, *19*, 2045–2052.